

RECLAMATION

Managing Water in the West

Technical Memorandum 86-68260-16-01

Estimating Groundwater Discharge from Phreatophyte Transpiration in Dixie Valley, Nevada

**Dixie Valley Groundwater Export Study,
Mid-Pacific Region**



**U.S. Department of the Interior
Bureau of Reclamation
Technical Service Center
Denver, Colorado**

May 2016

Mission Statements

The Department of the Interior protects and manages the Nation's natural resources and cultural heritage; provides scientific and other information about those resources; and honors its trust responsibilities or special commitments to American Indians, Alaska Natives, and affiliated island communities.

The mission of the Bureau of Reclamation is to manage, develop, and protect water and related resources in an environmentally and economically sound manner in the interest of the American public.

BUREAU OF RECLAMATION
Technical Service Center, Denver, Colorado
Geographic Applications and Analysis Group, 85-826000

Technical Memorandum 85-826000-16-01

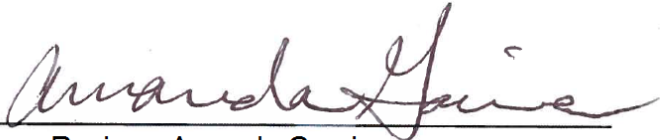
Estimating Groundwater Discharge from Phreatophyte Transpiration in Dixie Valley, Nevada

**Dixie Valley Groundwater Export Study,
Mid-Pacific Region**



Prepared: David Eckhardt
Physical Scientist
Geographic Applications and Analysis Group

5-17-2016
Date



Peer Review: Amanda Garcia
Hydrologist
U.S. Geological Survey, Nevada Water Science Center

5/18/16
Date

Disclaimer

The information contained in this report regarding commercial products or firms may not be used for advertising or promotional purposes and is not to be construed as an endorsement of any product or firm by the Bureau of Reclamation.

Acknowledgments

The author would like to thank Susan Buto and the late LaRue Smith of the USGS NWSC (Nevada Water Science Center), and David Groeneveld of HydroBio Advanced Remote Sensing for their assistance with field work and image interpretation during the course of this project, Justin Huntington of Huntington Hydrologic for assistance with image interpretation and incorporation of gridded weather datasets into the ETg calculations, and Amanda Garcia of the USGS NWSC for her assistance with image interpretation and for her thorough review of this report.

Executive Summary

As part of a groundwater export feasibility study, Public Law 110-161 directed the U.S. Bureau of Reclamation (Reclamation) to assess the perennial yield of groundwater from the Dixie Valley, NV, and assess its quality. Partners in this effort include the U.S. Geological Survey (USGS), Huntington Hydrologic (HH), and three consulting firms (HydroBio Advanced Remote Sensing, Santa Fe, NM; Interflow Hydrology, Inc., Truckee, CA; Mahannah and Associates, LLC, Reno, NV). Dixie Valley is located in arid western Nevada, approximately 140 km east of Reno, NV. A larger Dixie Valley Hydrologic Area (DVHA) was investigated during the course of this study because of theorized hydrologic connection between Dixie Valley and neighboring valleys (or basins) to the north, east, and south (Figure 1). These valleys within the DVHA constitute a closed hydrologic system with Dixie Valley at the lowest elevation. Therefore, the perennial yield of groundwater (i.e., the amount of groundwater that can be removed from the basins each year without lowering the water table) was estimated as the quantity of groundwater lost to the atmosphere through direct evaporation from the periodically inundated central playas, and transpiration from phreatophytic vegetation.

This report describes how Reclamation used the NDVI* method developed by HydroBio Advanced Remote Sensing to estimate groundwater loss through phreatophyte transpiration in the DVHA. NDVI* refers to a rescaled version of the Normalized Distance Vegetation Index (NDVI) image transformation (Rouse et al., 1974) that is typically applied to Landsat Thematic Mapper (TM) or similar optical imagery. NDVI* values are simply NDVI values that have been linearly rescaled to occupy a range between 0.0 for bare soil, and 1.0 for vigorous, full-canopy crops (Gillies et al., 1997). When calculated using carefully selected mid-summer images, Groeneveld et al. (2007) showed that NDVI* is linearly related to ET_g (groundwater evapotranspiration) by phreatophytes in arid environments where the water table is below the limit of capillary rise.

Image Acquisition and Calibration

Reclamation acquired Landsat TM images covering the DVHA on 41 different dates between 2002 and 2011 to promote understanding of the annual and seasonal variations in surface conditions. A subset of these images used in quantitative analyses was calibrated to surface reflectance to remove the unwanted effects of the atmosphere on the image data. The first step in the image calibration procedure was to convert the native spectral radiance data contained in TM images to top of the atmosphere (TOA) reflectance data. This process normalized the effects of varying sun angles and earth-to-sun distances between image acquisition dates. Reclamation then identified two calibration targets on the Landsat TM images: a bright sand dune field and a dark spring-fed lake whose spectral reflectance values were stable over time. Reclamation measured the

surface reflectance of the bright sand calibration target using a handheld spectroradiometer, while HydroBio measured the surface reflectance of the dark lake from a low-flying light aircraft. A set of six unique calibration models relating TOA reflectance to surface reflectance (one for each TM spectral band) was developed for each image acquisition date. These models were applied to selected TOA reflectance images to generate calibrated surface reflectance images. Calibrated surface reflectance data were smoothed using a 3x3-pixel moving average filter. This procedure reduced random image noise by a factor of three, and reduced the impact of slight pixel-to-pixel misregistration from one image to the next. Calibrated and smoothed surface reflectance data were used to generate NDVI and NDVI* images.

NDVI* Analysis

Groeneveld et al. (2007) showed that for phreatophytes in arid regions where the groundwater is below the limit of capillary rise, ET_g (groundwater transpiration) can be estimated as the product of NDVI* and adjusted atmospheric water demand (ASCE standardized grass reference evapotranspiration minus annual precipitation). Application of the NDVI* method to the DVHA required assembling the required weather data to characterize annual ET_o and precipitation across the DVHA, mapping the phreatophyte zones where the method would be applied, and defining the soil background and saturation NDVI values that would define the scaling of NDVI to NDVI*.

Obtaining Annual ET_o and Precipitation Data

ET_o for Dixie Valley for water years 2010 and 2011 was calculated from solar radiation, air temperature, humidity, and wind speed data collected at a weather station installed in Dixie Valley in August, 2009. For years prior to water year 2010, and for all years for the other basins in the DVHA, ET_o was estimated from a raster ET_o dataset generated from gridded Parameter-elevation Regressions on Independent Slopes Model (PRISM) and North American Land Data Assimilation System, Phase 2 (NLDAS-2) weather data. Monthly ET_o estimates from the raster ET_o dataset were bias-corrected to more accurately predict the ET_o measured at the Dixie Valley weather station. Monthly correction coefficients were defined as the ratio of average monthly ET_o at the Dixie Valley weather station (from its installation in 2009 through December, 2012) to average monthly gridded ET_o estimates for the same time period.

A similar method was used to estimate annual precipitation totals using gridded PRISM precipitation data. A correction factor for annual PRISM precipitation estimates was calculated as the ratio of the 2010-2011 average annual precipitation measured at a USGS eddy covariance station in Dixie Valley to the PRISM value for the same time period and location.

Defining the Phreatophyte Zones

The USGS, HydroBio, and Reclamation cooperated to delineate the Dixie Valley phreatophyte zone using both 30-meter Landsat TM imagery and high resolution aerial imagery. Reclamation used similar methods to define the phreatophyte zones for the other basins within the DVHA.

Generating the “Leaf-off” NDVI₀ Image

Soil background NDVI values varied greatly across Dixie Valley and the other DVHA basins, therefore a single NDVI value could not be used to characterize the soil background NDVI condition (NDVI₀). An image of spatially varying NDVI₀ values was required for the NDVI* method to function properly. This image was created using NDVI values generated from calibrated TM images acquired in late fall and winter, after the phreatophytic shrubs had lost their leaves. Because increasing soil moisture content nearly always increases bare soil NDVI values, historic weather data measured at the two closest weather stations were consulted when selecting the candidate “leaf-off” images. In an effort to match the dry soil conditions present in midsummer images, only image acquisitions dates that were preceded by extended periods of dry weather were considered to characterize NDVI₀. Six cloud-free images met that criterion, but close inspection of the NDVI images showed localized variations in NDVI between dates, indicating that any single leaf-off date would not produce an optimal NDVI₀ image. Instead, the NDVI₀ image was created by selecting the minimum NDVI value from the six candidate leaf-off images, on a pixel-by-pixel basis. The resulting image was masked to remove areas of dense spring-fed and phreatophytic shrub vegetation that produced elevated NDVI values during the winter months. These areas were filled with NDVI values from surrounding areas. A similar masking and filling procedure was applied to locations that were covered by a salt crust during the winter months, but not in the summer.

Generating the “Leaf-On” NDVI images

The NDVI* method of estimating phreatophyte ET_g requires a summertime “leaf-on” NDVI image to characterize the condition of full-canopy phreatophytic vegetation. Images acquired in late July or early August were chosen for this purpose because it was assumed that at this time of year, non-phreatophytic vegetation had either died or gone dormant, minimizing its contribution to the NDVI signal. Mid-summer TM images acquired on 8/8/07, 7/25/08, 7/28/09, 7/31/10, and 8/3/11 were used to characterize the “leaf-on” condition for those five years.

Generating NDVI* images and initial ET_g maps

NDVI* images were generated by linearly rescaling each pixel value in the “leaf-on” NDVI images between the “leaf-off” NDVI₀ image value at which NDVI* = 0, and the saturation NDVI value of 0.915 (seen in vigorous, full-cover agricultural fields) at which NDVI* = 1.0. NDVI* values from areas of natural vegetation were multiplied by annual ETo minus precipitation to generate annual ET_g maps. Agricultural fields that exhibited NDVI values in excess of 0.75, or

were active center pivot fields were assigned an ET_g value equal to 1.1 times the net irrigation requirement estimated by the Nevada Division of Water Resources for Dixie Valley (1219 mm). ET_g for other agricultural lands were estimated using the NDVI* method, but their ET_g values were not allowed to exceed 1219 mm.

The Effect of Non-Phreatophytic Vegetation

The NDVI* procedure is predicated on the assumption that the NDVI* signal can be associated with phreatophytic vegetation only. The boundaries of the phreatophyte zones within the DVHA were delineated to include only those areas containing phreatophytic vegetation; but vegetation in those zones includes non-phreatophytic grasses, forbs and shrubs as well, particularly near the upper phreatophyte zone boundaries. Vegetation of all types can respond to significant precipitation events in the spring and early summer, and such events can prolong the period of leaf retention for non-phreatophytic shrubs, producing elevated NDVI* values. And high concentrations of dead, dry herbaceous vegetation such as cheat grass that grew in response to favorable conditions earlier in the year can also increase NDVI* values. Visual inspection of the annual ET_g images indicated that while the majority of the DVHA exhibited similar ET_g estimates for at least three of the five years, large differences over the five-year period were common, indicating residual effects from non-phreatophytic vegetation during the anomalous years. No single year produced an ET_g estimate that was free from the effect of non-phreatophytic vegetation.

Estimating ET_g by Phreatophytes Using Multiscene Averages

Separate from spatial variation in annual ET_g estimates produced by non-phreatophytic vegetation, annual ET_g estimates also varied with slight errors in image calibration and variations in annual ETo and annual precipitation from year to year. A multiscene averaging approach was seen as an effective way to deal with variation in image calibration and weather factors, but all five images could not be averaged without including anomalously high ET_g estimates produced from pixels contaminated with NDVI signal from non-phreatophytic vegetation. Achieving the beneficial aspects of averaging multiple years of ET_g estimates while minimizing the influence of non-phreatophytic vegetation on those estimates was accomplished by generating new ET_g images composed of the average of the lowest two or lowest three ET_g estimates for each individual pixel. The average of the lowest three ET_g estimates was used to generate ET_g estimates for Dixie Valley and all of the adjacent DVHA basins except for Edwards Creek Valley, where the average of the lowest two ET_g estimates was used. Final ET_g estimates including pumped groundwater used by agriculture are 17,842 AF (acre feet) for Dixie Valley and 29,424 AF for the entire DVHA. Excluding agricultural lands from these calculations (with no estimate of pre-development ET_g), annual ET_g estimates decrease to 13,830 AF for Dixie Valley, and 20,826 AF for the DVHA. Complete listings of ET_g estimates are presented in Tables 8 and 9.

Table of Contents

| | <i>Page</i> |
|--|-------------|
| Executive Summary | iii |
| Image Acquisition and Calibration | iii |
| NDVI* Analysis..... | iv |
| Obtaining Annual ETo and Precipitation Data | iv |
| Defining the Phreatophyte Zones..... | v |
| Generating the “Leaf-off” NDVI ₀ Image | v |
| Generating the “Leaf-On” NDVI images | v |
| Generating NDVI* images and initial ETg maps | v |
| Estimating ETg by Phreatophytes Using Multiscene Averages | vi |
| Introduction..... | 1 |
| Background..... | 3 |
| Image Acquisition..... | 5 |
| Calibrating TM Imagery to Apparent Surface Reflectance | 7 |
| Reflectance Data Acquisition | 8 |
| Airborne Reflectance Data Processing | 10 |
| Defining and Applying Corrections to Reflectance Data | 10 |
| Generating Surface Reflectance Values for Calibration Targets in the Thematic Mapper Spectral Bands | 15 |
| Correcting Surface Reflectance Values for Variations in Local Sun Angle..... | 16 |
| Processing Surface Reflectance Data..... | 16 |
| Calibrating Thematic Mapper Images to Apparent Surface Reflectance | 17 |
| NDVI* Analysis..... | 20 |
| Obtaining Annual ETo and Precipitation Data | 20 |
| Defining the Phreatophyte Zones..... | 23 |
| Generating “Leaf-On” NDVI Images | 24 |
| Generating the “Leaf-Off” NDVI ₀ Image | 24 |
| Late Fall and Winter NDVI Images as a Solution to Spatially Variable NDVI ₀ | 27 |
| Challenges Involved with Using a Separate “Leaf-Off” Scene | 27 |
| Generating a Composite “Leaf-Off” Image | 30 |
| Generating NDVI* Images | 39 |
| The Effect of Non-Phreatophytic Vegetation | 39 |
| Correlation with Phreatophyte Canopy Cover Data | 43 |
| Generating ETg Images | 46 |
| Final Estimates of ETg..... | 48 |
| Combining Multiple Years of ETg Estimates..... | 48 |
| Multidate Averaging | 48 |
| Multidate Minimum | 48 |
| Obtaining the Optimal ETg Estimate..... | 49 |

| | |
|---|----|
| Discussion..... | 54 |
| Comparing Results with Those from Other Studies | 54 |
| USGS Eddy Covariance Data and the NDVI* to ET* Relationship | 54 |
| Comparisons with ETg Estimates from Previous Studies | 56 |
| Comparisons with ETg Estimates from Concurrent Studies | 57 |
| Reclamation’s Implementation of the NDVI* Method | 63 |
| Applying the NDVI* Method Using LEDAPS Imagery | 64 |
| Appendix—Calculating Bidirectional Reflectance Factors for the Spectralon SRS-99 Reference Panel | 68 |
| Determining Wavelength-Specific Spectralon Reflectance Factors in the Visible and Near Infrared..... | 69 |
| Determining Spectralon Reflectance Factors in the Shortwave Infrared (1301 nm – 2500 nm)..... | 73 |
| References..... | 75 |

List of Tables

| | <i>Page</i> |
|--|-------------|
| Table 1. Landsat Images Acquired for the Dixie Valley Project..... | 6 |
| Table 2. Sun Angle and Spectralon BRDF Correction Factors Used in the Calculation of the Data Presented in Figure 4..... | 13 |
| Table 3. Initial and final regression models used to calibrate 11/1/09 TOA reflectance images to apparent surface reflectance | 17 |
| Table 4. Calculated and Final PRISM/NLDAS-2 ETo Correction Coefficients by Month..... | 22 |
| Table 5. Grass Reference Evapotranspiration (ETo) and Annual Precipitation for the DVHA for Water Years 2007–2011 | 23 |
| Table 6. Surface Reflectance Values in the TM Spectral Bands and Derived NDVI and MSAVI Values for Soils in the Dixie Valley Area | 27 |
| Table 7. Comparison of Annual ETg Estimates from NDVI* and USGS Eddy Covariance Stations at Sparse Vegetation and Dense Vegetation Sites..... | 34 |
| Table 8. ETg Estimates by DVHA Basin in Acre Feet and Inches | 52 |
| Table 9. Final ETg Estimates by DVHA Basin in Acre Feet and Inches | 53 |
| Table 10. Comparison of Groundwater Discharge Volume Estimates in the Dixie Valley Phreatophyte Zone | 57 |
| Table 11. Comparison of Reclamation and USGS ETg and Phreatophytic Shrub Canopy Cover Estimates for the Three USGS ET Units | 60 |
| Table 12. Comparison of Reclamation and Huntington Hydrologic ETg Estimates | 62 |
| Table 13. Comparison of 2007–2011 ETg Estimates Generated from TM Image Data Calibrated to Surface Reflectance Using the Reclamation and LEDAPS Procedures | 65 |

Table 14. Comparison of Hybrid ET_g Estimates Generated from TM Image Data Calibrated to Surface Reflectance Using the Reclamation and LEDAPS Procedures66

Table A-1. Spectralon BRDF and DHR for a Nadir-Viewing Sensor at 632.8 nm.....69

List of Figures

| | <i>Page</i> |
|---|-------------|
| Figure 1. The Dixie Valley hydrographic area. | 2 |
| Figure 2. Locations of calibration targets whose reflectance was measured from the air on 11/2/09. | 9 |
| Figure 3. Spectralon SRS-99 directional / hemispheric reflectance by wavelength. | 11 |
| Figure 4. Pre- and post-flight Spectralon spectra, showing the effects of Spectralon BRDF and sun angle corrections. | 13 |
| Figure 5. Fully processed pre- and post-flight Spectralon reflectance values and the ASD calibration drift correction factor derived from them.... | 14 |
| Figure 6. Plots of surface reflectance values from the 11/2/09 HydroBio flight and 9/25/09 Reclamation ground data acquisition with TOA reflectance values from the 11/1/09 P42R33 TM image. | 18 |
| Figure 7. Locations of the Dixie Valley weather station and the four eddy covariance flux towers shown on the 7/31/10 TM scene..... | 21 |
| Figure 8. Phreatophyte zones of the Dixie Valley hydrographic area. | 25 |
| Figure 9. Locations near the southern portion of the Dixie Valley phreatophyte zone at which soil reflectance was measured on 6/18/09. | 26 |
| Figure 10. Stacked bar chart comparing monthly precipitation totals for the Centroid and Fallon weather stations..... | 29 |
| Figure 11. Locations at which soil background reflectance was measured in September 2012. | 32 |
| Figure 12. Comparison of surface-measured bare soil NDVI to NDVI0 image values..... | 33 |
| Figure 13. 7/31/10 NDVI and 2010 color infrared NAIP images showing two concentric circles identifying the calculated source areas for 45% and 90% of the water vapor flux measured at the DV station. | 34 |
| Figure 14. 8/8/07 brightness temperature vs. albedo for sparsely vegetated to unvegetated areas in the Dixie Valley phreatophyte zone. | 35 |
| Figure 15. Dense phreatophyte areas in a portion of Dixie Valley and Edwards Creek Valley phreatophyte zones identified using the temperature anomaly method, and spring-fed and flowing well areas identified by the USGS and Reclamation on the 8/8/07 TM image. | 37 |
| Figure 16. A salt-covered area northeast of the Dixie Valley playa. | 38 |

Figure 17. NDVI* images of the Edwards Creek Valley area showing the impact of non-phreatophytic vegetation on NDVI* values within the phreatophyte zone. 41

Figure 18. Field photos showing herbaceous vegetation existing within and above the Edwards Creek Valley phreatophyte zone, referenced to 7/28/09 NDVI* image..... 42

Figure 19. Color-coded NDVI* images from 2007–2011 and the 7/28/09 surface reflectance image as spatial reference. 44

Figure 20. Locations of 20 sites at which phreatophytic shrub canopy cover was measured in 2010..... 45

Figure 21. Scatterplots showing the relationships between phreatophytic shrub canopy cover measured in June 2010 with NDVI* values from 2007–2011..... 47

Figure 22. NDVI* images generated using the three hybrid methods: the average of the lowest two NDVI* values, the average of the lowest three, and the second lowest..... 49

Figure 23. Scatterplots showing the relationships between phreatophytic shrub canopy cover measured in June 2010 with hybrid NDVI* values. 50

Figure 24. Scatterplots showing the relationships between phreatophytic shrub canopy cover measured in June 2010 and ET_g values estimated using the three hybrid approaches. 51

Figure 25. The relationship between NDVI* and ET* developed from data presented in Groeneveld et al. (2007) and this study..... 55

Figure 26. Relationship between averaged mean summer EVI/T_b from 2009 through 2011 and phreatophytic shrub cover..... 58

Figure 27. The relationship between NDVI* and ET* developed from data presented in Beamer et al. (2013). 61

Figure A-1. Measured hemispheric BRF of Spectralon at 632.8 nm..... 68

Figure A-2. Spectralon DHR and BRF values measured normal to the panel at five different illumination angles..... 69

Figure A-3. Spectralon BRDF (bidirectional reflectance distribution function) as a function of viewing angle for four different illumination angles, from NIST measurements. 70

Figure A-4. 0°/45° and 6°/hemispherical (incidence/view) reflectance factors of Spectralon and their ratios. 72

Acronyms

| | |
|---------|---|
| AF | acre foot |
| ASCE | American Society of Civil Engineers |
| ASD | Analytical Spectral Devices |
| BRDF | bidirectional reflectance distribution function |
| BRF | bidirectional reflectance factor |
| DHR | directional/hemispherical reflectance |
| HH | Huntington Hydrologic |
| DV | USGS dense vegetation eddy covariance site |
| DVHA | Dixie Valley hydrographic area |
| ET | evapotranspiration |
| ETM+ | Enhanced Thematic Mapper Plus |
| EVI | Enhanced Vegetation Index |
| EWRI | Environmental and Water Resources Institute |
| GloVis | USGS Global Visualization Viewer |
| HH | Huntington Hydrologic |
| LEDAPS | Landsat Ecosystem Disturbance Adaptive Processing System |
| MSAVI | Modified Soil Adjusted Vegetation Index |
| NAIP | National Agricultural Imagery Program |
| NDVI | Normalized Difference Vegetation Index |
| NIR | near infrared |
| NLDAS-2 | North American Land Data Assimilation System, Phase 2 |
| NWSC | Nevada Water Science Center |
| PRISM | Parameter-elevation Regressions on Independent Slopes Model |
| PTFE | polytetrafluoroethylene |
| SV | USGS sparse vegetation eddy covariance site |
| TM | Thematic Mapper |
| TOA | top of the atmosphere |
| USGS | United States Geological Survey |
| WGS84 | World Geodetic System 1984 |
| WRS | World Reference System |

Variables

| | |
|--------------------------|---|
| $\rho_{TM\#}$ | surface reflectance in TM band # |
| $\rho_{TM\#,corr}$ | surface reflectance in TM band # corrected for variable illumination conditions |
| $\rho_{toa, TM\#}$ | at-satellite (TOA) reflectance in TM band # |
| $\rho_{\lambda, corr}$ | corrected reflectance in spectral band λ |
| ρ_{λ} | measured reflectance in spectral band λ |
| λ | wavelength |
| $Bias_{TM\#}$ | image DN to radiance bias value for TM band # |
| $\theta_{sun_corr, Ti}$ | sun angle correction at time Ti |
| Cal_corr, λ, Ti | calibration drift correction for spectral band λ at time Ti |
| d | earth-to-sun distance (astronomical units) |
| $DHR_{spec, \lambda}$ | Spectralon directional/hemispheric reflectance for wavelength λ |
| $DN_{TM\#}$ | image coded radiance (“digital number”) in TM band # |
| ETa | annual evapotranspiration |
| ETg | annual groundwater evapotranspiration |
| ETo | ASCE Standardized grass reference ET |
| $ESUN_{TM\#}$ | mean solar exoatmospheric irradiance in TM band # ($W\ m^{-2}\ \mu m^{-1}$) |
| f_{λ} | sensor response function at wavelength λ |
| $Gain_{TM\#}$ | DN to radiance gain value for TM band # |
| $L_{TM\#}$ | at-sensor spectral radiance ($W\ m^{-2}\ \mu m^{-1}\ sr^{-1}$) in TM band # |
| $NDVI^*$ | NDVI rescaled between soil background (0) and saturation (1) |
| $NDVI_0$ | soil background NDVI value |
| $NDVI_S$ | saturated NDVI value typical of a vigorous, full cover vegetation canopy |
| $NDVI_{soil}$ | NDVI calculated from field-measured soil background reflectance |
| ppt | annual precipitation |
| T | time |
| θ | solar zenith angle (angle to the sun measured from zenith) |
| θ_i | local illumination angle (relative to surface normal) |
| θ_{sun_corr} | sun angle correction |
| θ_v | view angle (relative to surface normal) |

Introduction

As authorized in Public Law 110-161, the U.S. Bureau of Reclamation (Reclamation) and its partners, the U.S. Geological Survey (USGS), and four consulting firms (HydroBio Advanced Remote Sensing, Santa Fe, NM, Mahannah and Associates, LLC, Reno, NV, Interflow Hydrology, Inc., Truckee, CA, and Huntington Hydrologic (HH), Carson City, NV) engaged in a study to assess the perennial yield of groundwater from the Dixie Valley hydrologic system, and assess its quality. This work is the necessary precursor to an economic feasibility study for exporting the perennial groundwater yield to the Carson Desert Hydrologic Area southwest of Dixie Valley.

Dixie Valley is a closed drainage basin in western Nevada, approximately 140 km east of Reno, NV (Figure 1). It is bordered on the west and northwest by the Stillwater Range, on the northeast by the Augusta Mountains, on the southeast by the Clan Alpine Mountains, on the south by Fairview Valley and on the north by the Tobin Range. Dixie Valley is connected hydraulically to six adjacent basins: Pleasant, Jersey, Fairview, Stingaree, Cowkick, and Eastgate Valleys, and is the terminus of this flow system. Edwards Creek Valley 35 km southeast of Dixie Valley may also be hydraulically connected with Dixie Valley, and is included with the other valleys to form the Dixie Valley Hydrologic Area (DVHA). The climate of the valley lowlands is characterized as desert, with average precipitation of approximately 16 cm, most of which occurs in the winter and spring. Annual precipitation increases to 40 to 50 cm in the high elevations of the mountains surrounding Dixie Valley.

Similar to most basin and range valleys in Nevada, erosion of surrounding mountains has filled Dixie Valley with unconsolidated deposits that constitute the basin-fill aquifer system. Although tertiary volcanic material may exist beneath and within older basin fill deposits, most if not all ground-water pumping is from the basin-fill aquifer system. Due to interbedded layers of fairly permeable sand and gravel with comparatively impermeable silt and clay, ground water in the Dixie Valley basin-fill aquifer system is under both unconfined and confined conditions (<http://nevada.usgs.gov/water/projects/dixie.htm>).

Because Dixie Valley is a closed basin, the perennial yield of groundwater (i.e., the amount of groundwater that can be removed from the basin each year without lowering the water table) can be estimated from the current loss of groundwater to the atmosphere through direct evaporation from the periodically inundated central playa, and transpiration from phreatophytic vegetation surrounding the playa. Greasewood (*Sarcobatus Vermiculatus*) is the dominant phreatophyte, but phreatophytic big saltbush (*Atriplex lentiformis*) and rabbit brush (*Chrysothamnus nauseosus*) are also present in some areas (Garcia et al., 2014). This report describes how Reclamation estimated groundwater loss from the phreatophyte zone. Evaporation from the Dixie Valley playa is being estimated by project partners.

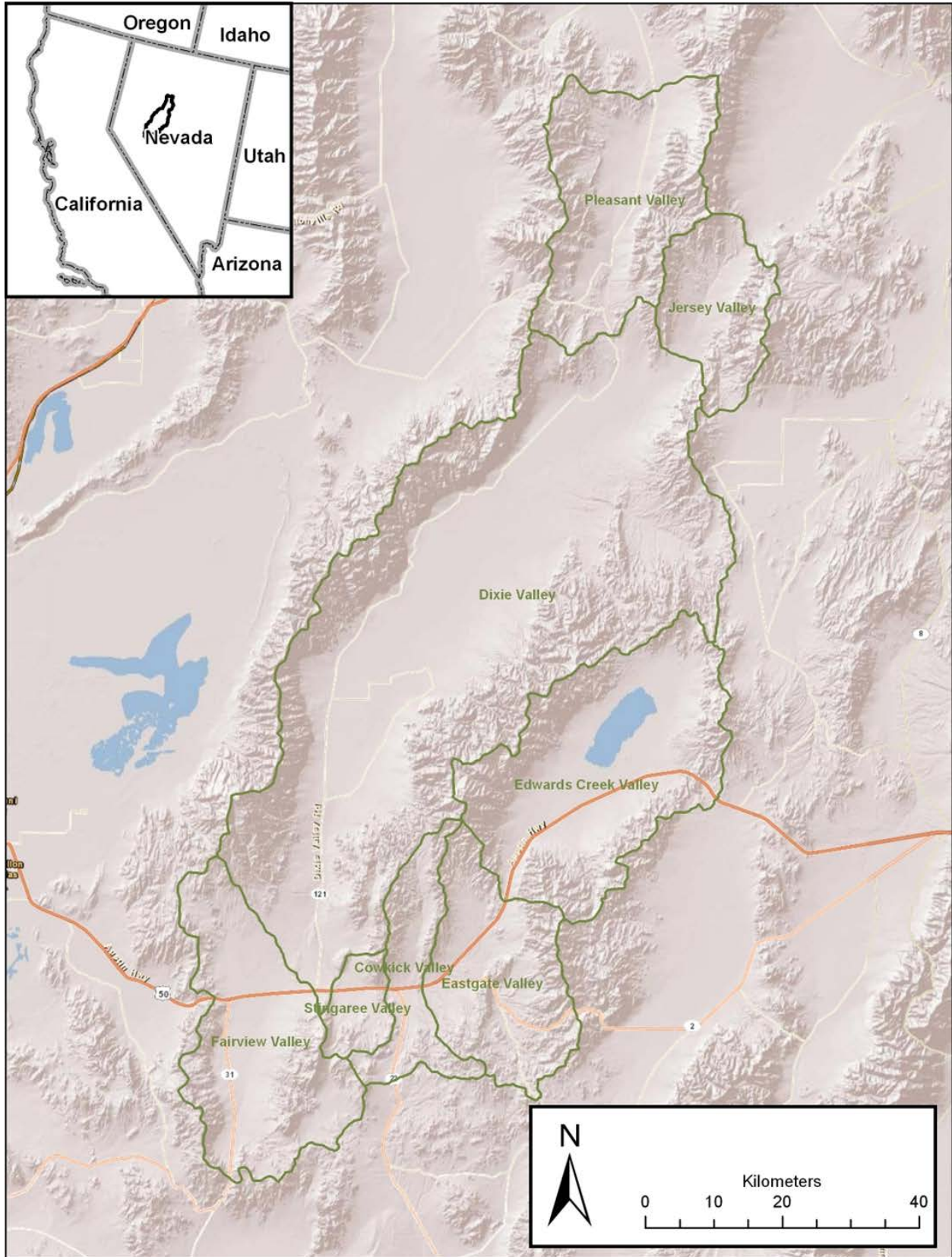


Figure 1. The Dixie Valley hydrographic area.

Background

Reclamation used the NDVI* procedure developed by HydroBio Advanced Remote Sensing to estimate groundwater loss through phreatophyte transpiration. The evolution of this procedure is described fully in Baugh and Groeneveld (2006), Groeneveld and Baugh (2007), and Groeneveld et al. (2007), and is summarized below.

The NDVI* procedure is based upon the Normalized Difference Vegetation Index (NDVI) image transformation. NDVI takes advantage of the reflectance properties of terrestrial green-leaf vegetation to form a readily interpretable vegetation index with values between -1 and 1 (Equation 1).

$$\text{NDVI} = (\text{NIR} + \text{red}) / (\text{NIR} - \text{red}) \quad (1)$$

where:

NDVI = normalized difference vegetation index
NIR = near infrared reflectance
Red = red reflectance

Red light is readily absorbed by chlorophyll within plant leaves to provide the energy required for photosynthesis. The slightly longer wavelengths of near infrared light are not absorbed by chlorophyll, but instead are strongly scattered from and transmitted through green leaves. Healthy green leaves produce high NIR and low red reflectance, and therefore high NDVI values. Similar reflectance in the red and NIR indicates little photosynthetic activity, and produces low NDVI values.

While NDVI values are sensitive to the amount of green-leaf vegetation present in each image pixel, they are also affected by the reflectance characteristics of the soil background. NDVI* is a linear transformation of NDVI that minimizes soil influences by scaling soil NDVI to zero, while rescaling the maximum, full-vegetation-canopy NDVI value to 1.0 (Equation 2).

$$\text{NDVI}^* = (\text{NDVI} - \text{NDVI}_0) / (\text{NDVI}_s - \text{NDVI}_0) \quad (2)$$

where:

NDVI* = NDVI rescaled between soil background (0) and saturation (1)
NDVI = mid-summer NDVI value
NDVI₀ = soil background NDVI value
NDVI_s = saturated NDVI value typical of a vigorous, full cover vegetation canopy

When calculated from a carefully selected summer TM scene in which non-phreatophytic vegetation is dormant or dead, the green leaf vegetation signal measured by NDVI* can be associated entirely with phreatophytic vegetation. Under these conditions, and when there is no surface evaporation of groundwater, Groeneveld et al. (2007) showed that NDVI* is directly related to ETa (total annual evapotranspiration) (Equation 3). Groundwater transpiration by phreatophytes was assumed equal to total ET (evapotranspiration) minus precipitation (assuming negligible runoff and changes in soil water storage over the course of a year), and was mapped on a pixel-by-pixel basis using Equation 4. The ETg volume for each pixel within the phreatophyte zone was calculated as depth of transpired water (mm) * area of the pixel (900 m²). The ETg volumes of all phreatophyte zone pixels were summed to generate ETg volume estimates for the entire phreatophyte zone.

$$ETa = NDVI* (ETo - ppt) + ppt \quad (3)$$

where:

- ETa = annual evapotranspiration (mm)
- NDVI* = normalized NDVI (bare soil = 0, vigorous vegetation = 1)
- ETo = annual grass reference evapotranspiration from nearby weather station (mm)
- ppt = annual precipitation measured at a nearby weather station (mm)

$$ETg = ETa - ppt = NDVI* (ETo - ppt) \quad (4)$$

where:

- ETg = annual groundwater loss through phreatophyte transpiration (mm)
- ETa = annual evapotranspiration (mm)
- ppt = annual precipitation measured at a nearby weather station (mm)
- ETo = annual grass reference evapotranspiration from nearby weather station (mm)

Equation 4 was used to estimate ETg within the DVHA, but image calibration and the definition of NDVI₀ were modified from that described in Groeneveld et al. (2007). This report describes the procedure used by Reclamation to acquire and process image and spectroradiometer data, calibrate the image data to surface reflectance, assemble spatially variable weather data, generate the NDVI* images, and finally generate ETg estimates for the DVHA.

Image Acquisition

Reclamation acquired and processed all satellite imagery used by Reclamation and the USGS. The study area was covered by two adjacent Landsat images on the same satellite path: World Reference System (WRS) path 42, rows 32 and 33. Reclamation used the USGS GloVis (Global Visualization Viewer) tool to download every Landsat 5 TM and Landsat 7 ETM+ image of the DVHA that was cloud-free over the phreatophyte zone from 2008 through 2010, plus some selected scenes from 2002-2007 and 2011. The images served by GloVis were processed to “level 1T”—terrain corrected spectral radiance images in the UTM projection and World Geodetic System 1984 (WGS84) geodetic datum. These images were imported into the native format of the ERDAS Imagine image processing software used for this project.

Landsat TM images acquired on 41 different dates between 2002 and 2011 were downloaded to allow for greater understanding of the annual and seasonal variations seen on the images (Table 1). Of particular importance were the spectral response of the various soils and vegetation communities to precipitation events, and the circumstances under which salt crusts form in parts of the phreatophyte zone. Only a subset of the images deemed most promising for quantitative analysis was calibrated to TOA (top of the atmosphere) and apparent surface reflectance.

Table 1. Landsat Images Acquired for the Dixie Valley Project

| Acquisition Date | Satellite / Sensor | Spectral Radiance | TOA Reflectance | Surface Reflectance |
|------------------|--------------------|-------------------|-----------------|---------------------|
| 3/3/02 | Landsat 5 TM | X | X | X |
| 10/21/05 | Landsat 5 TM | X | | |
| 11/22/05 | Landsat 5 TM | X | X | X |
| 5/9/06 | Landsat 7 ETM+ | X | | |
| 3/17/07 | Landsat 5 TM | X | X | X |
| 8/8/07 | Landsat 5 TM | X | X | X |
| 2/16/08 | Landsat 5 TM | X | | |
| 3/3/08 | Landsat 5 TM | X | | |
| 3/27/08 | Landsat 7 ETM+ | X | | |
| 4/12/08 | Landsat 7 ETM+ | X | | |
| 4/28/08 | Landsat 7 ETM+ | X | | |
| 5/30/08 | Landsat 7 ETM+ | X | | |
| 6/7/08 | Landsat 5 TM | X | | |
| 6/23/08 | Landsat 5 TM | X | | |
| 7/9/08 | Landsat 5 TM | X | | |
| 7/25/08 | Landsat 5 TM | X | X | X |
| 8/2/08 | Landsat 7 ETM+ | X | | |
| 8/10/08 | Landsat 5 TM | X | | |
| 9/3/08 | Landsat 7 ETM+ | X | | |
| 9/11/08 | Landsat 5 TM | X | | |
| 9/27/08 | Landsat 5 TM | X | | |
| 10/29/08 | Landsat 5 TM | X | | |
| 11/14/08 | Landsat 5 TM | X | X | X |
| 1/17/09 | Landsat 5 TM | X | X | X |
| 4/7/09 | Landsat 5 TM | X | X | X |
| 5/9/09 | Landsat 5 TM | X | X | X |
| 6/26/09 | Landsat 5 TM | X | X | X |
| 7/28/09 | Landsat 5 TM | X | X | X |
| 10/16/09 | Landsat 5 TM | X | X | X |
| 11/1/09 | Landsat 5 TM | X | X | X |
| 11/17/09 | Landsat 5 TM | X | X | X |
| 12/03/09 | Landsat 5 TM | X | X | X |
| 4/26/10 | Landsat 5 TM | X | X | X |
| 6/13/10 | Landsat 5 TM | X | X | X |
| 7/15/10 | Landsat 5 TM | X | X | X |
| 7/31/10 | Landsat 5 TM | X | X | X |
| 8/16/10 | Landsat 5 TM | X | X | X |
| 9/1/10 | Landsat 5 TM | X | X | X |
| 9/17/10 | Landsat 5 TM | X | X | X |
| 7/18/11 | Landsat 5 TM | X | X | X |
| 8/3/11 | Landsat 5 TM | X | X | X |

Calibrating TM Imagery to Apparent Surface Reflectance

Landsat TM imagery was used to generate NDVI images for Reclamation's work, and to generate Modified Soil Adjusted Vegetation Index (MSAVI; Qi et al., 1994) and Enhanced Vegetation Index (EVI; Huete et al., 2002) images requested by project partners. All of these image products produce the best correlation with surface biophysical properties when they are generated from image data calibrated to surface reflectance. Surface reflectance values are ratios of the spectral radiance received from a given pixel to that which would be received from a non-sloping, perfectly diffuse 100% reflector—without the effects of atmospheric scattering and absorption. Reclamation used astronomical data and surface reflectance measurements to perform this calibration.

The first step in the image calibration procedure was to normalize the effects of varying sun angles and earth-to-sun distances, yielding images of TOA reflectance values (Equation 5) (Markham and Barker, 1986; Irish, 2000). Sun elevation angles were calculated on a 1.5 km grid instead of using scene-center values to avoid abrupt changes in sun angle at image borders.

$$\rho_{\text{toaTM}\#} = (\pi * L_{\text{TM}\#} * d^2) / (\text{ESUN}_{\text{TM}\#} * \cos \theta) \quad (5)$$

where:

- $\rho_{\text{toaTM}\#}$ = at-satellite (TOA) reflectance in TM band #
- $L_{\text{TM}\#}$ = at-satellite radiance in TM band # $((\text{Gain}_{\text{TM}\#} * \text{DN}_{\text{TM}\#}) + \text{Bias}_{\text{TM}\#})$
- $\text{Gain}_{\text{TM}\#}$ = DN to radiance gain value for TM band #
- $\text{Bias}_{\text{TM}\#}$ = DN to radiance bias value for TM band #
- $\text{DN}_{\text{TM}\#}$ = image coded radiance value (“digital number”) in TM band #
- d = earth-to-sun distance in astronomic units
- θ = solar zenith angle (angle to the sun measured from zenith)
- $\text{ESUN}_{\text{TM}\#}$ = mean solar exoatmospheric irradiance in TM band #

Terrain slope and aspect affect TOA reflectance values to the extent that they modify incoming solar radiation intensity relative to that impinging on a level surface (i.e., the topographic effect). Reflectance data which retain topographic effects are referred to as “apparent reflectance” data because reflectance values are a function of both the reflectance characteristics of the surface and its orientation relative to the sun. Terrain effects can be largely removed by modeling local sun angles using digital terrain data, but such modeling can produce artifacts if the digital terrain data do not adequately represent the surface. Terrain correction was not performed on the Dixie Valley imagery because the National Elevation Dataset (NED) digital elevation model (DEM) showed

anomalous elevation readings in portions of the Dixie Valley playa, and showed obvious “terracing” in the alluvial fans adjoining the Dixie Valley phreatophyte zone. Although MSAVI and EVI exhibit some sensitivity to the topographic effect due to the soil adjustment factor used in their computation (Matsushita et al., 2007), the low slopes which characterize the phreatophyte zone minimized the influence of terrain effects. The purely ratio-based NDVI (and therefore NDVI*) values were not affected by slight variations in incoming solar radiation intensity caused by topography.

While calibration to TOA reflectance eliminates all image variation caused by radiometric calibration and astronomical differences between image acquisition dates, it ignores any scattering or absorption that takes place in the atmosphere. The effects of atmospheric scattering and absorption present in the TOA reflectance data were removed by applying a set of six date-specific empirical models to each TM image (one model per spectral band) that predicted measured surface reflectance from image TOA reflectance values. These models were defined using surface reflectance measurements of temporally stable calibration targets acquired from the ground and from a low-flying aircraft.

Reflectance Data Acquisition

All targets selected for image calibration purposes had to be spatially homogeneous over the spatial scale of at least a 3x3 block of TM pixels (a minimum of 90 meters by 90 meters in size), and in aggregate, had to cover a wide range of reflectance values in each TM spectral band. Furthermore, budgetary constraints restricted the collection of surface reflectance data to a single date, so it was critical to find calibration targets whose spectral reflectance properties changed little over the course of the year. Analyses of a time series of TOA reflectance images spanning all four seasons identified no targets with temporally stable reflectance values within Dixie Valley itself; but five promising targets with minimal date-to-date reflectance variation were identified in the Carson Desert area approximately 65 km southwest of Dixie Valley (Figure 2). These targets were deemed suitable for atmospheric correction purposes because they were all located on the same Landsat path as Dixie Valley and were of similar elevation above sea level (mean of 1232 m) to the areas of groundwater discharge within the DVHA (mean of 1185 m).

Both HydroBio and Reclamation collected surface reflectance data that were used in the image calibration process. On 11/2/09, HydroBio acquired reflectance data for the five candidate reflectance calibration targets shown in Figure 2 from a Cessna 185 fixed wing aircraft flying at approximately 300 meters above the ground. Weather conditions were good with clear skies and light winds. HydroBio used an Analytical Spectral Devices (ASD) FieldSpec FR spectroradiometer with a 3-degree field-of-view foreoptic which generated a 16-meter spot size at the nominal flight altitude. Prior to takeoff, the system was calibrated to insolation (incoming solar radiation) conditions using a Spectralon[®] SRS-99 reference panel. Reflectance measurements were made at a rate of 30 per

minute over the calibration targets, producing a nominal separation of 125 meters between initiations of each spectrum measurement. The system is described in Groeneveld et al. (2006). The mount used to hold the ASD foreoptic on the aircraft was modified to hold a small video camera that recorded continuous video during the reflectance data acquisition flight. Time-synchronization between the video camera and the spectroradiometer simplified the identification of target spectra.

On 9/25/09, Reclamation used an ASD FieldSpec FR spectroradiometer with a nominal 15-degree field of view to measure surface spectral reflectance at two locations of homogeneous sand 1700 meters apart in the eastern and southern portions of the Sand Mountain dune area (Figure 2). Sand from each sampling site was placed on a tray which was leveled and smoothed prior to reflectance measurements. 20 spectra were acquired for each sample immediately after instrument calibration. Reflectance spectra from the two sites were indistinguishable from one another.

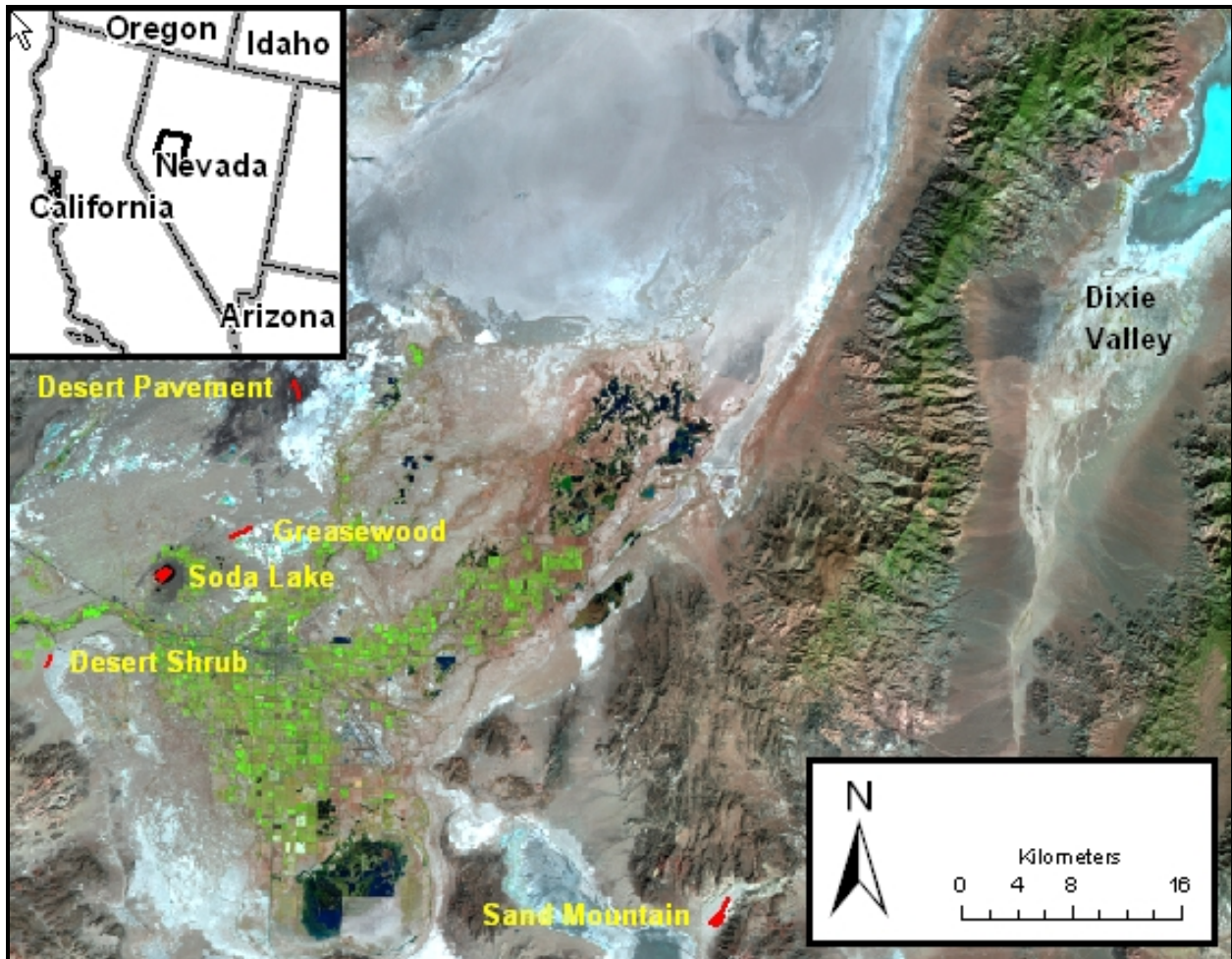


Figure 2. Locations of calibration targets (in red) whose reflectance was measured from the air on 11/2/09. The background TM image was acquired on 11/1/2009, and is displayed as band 5,4,3 (R,G,B).

Airborne Reflectance Data Processing

Defining and Applying Corrections to Reflectance Data

The reflectance data acquired from HydroBio's aircraft were processed to reduce the effects of three significant factors: 1) Spectralon bi-directional reflectance characteristics, 2) changing sun angle during data acquisition, and 3) sensor calibration drift. Multiplicative correction factors developed for each of these effects were applied to the airborne reflectance data to produce the best estimates of actual surface reflectance (Equation 6). The derivation of each correction factor is discussed below.

$$\rho_{\lambda,corr,Ti} = \rho_{\lambda,Ti} * BRF_{\theta_i,\theta_v,\lambda,T0} * \theta_{sun_corr,Ti} * Cal_{corr,Ti,\lambda} \quad (6)$$

where:

| | |
|--------------------------------------|---|
| $\rho_{\lambda,corr,Ti}$ | = corrected reflectance in spectral band λ at time Ti |
| $\rho_{\lambda,Ti}$ | = measured reflectance in spectral band λ at time Ti |
| $BRF_{\theta_i,\theta_v,\lambda,T0}$ | = bidirectional reflectance factor of the Spectralon reference panel for , spectral band λ under illumination angle θ_i at instrument calibration time $T0$ and nadir viewing angle θ_v |
| $\theta_{sun_corr,Ti}$ | = sun angle correction at time Ti |
| $Cal_{corr,Ti,\lambda}$ | = calibration drift correction for spectral band λ at time Ti |

Correcting for Spectralon Bidirectional Reflectance Characteristics

The ASD spectroradiometer measures spectral reflectance in the 350 to 2500 nm spectral range and reports them in 1 nm increments. Reflectance is calculated as the ratio of target spectral radiance to that received from a calibration panel of known reflectance. For this project, a 12-inch Spectralon SRS-99 reflectance panel was used for calibration. Spectralon is a sintered polytetrafluoroethylene (PTFE) material manufactured by Labsphere, Inc. Spectralon is a commonly used reference panel for field reflectance data collection because it is durable, easily cleaned in the field, and is a good approximation to the perfectly diffuse, 100% reflector against which reflected sunlight from surface materials are compared to calculate reflectance. Spectralon panels come in a variety of "brightnesses" characterized by their directional/hemispherical reflectance (DHR). In the case of Spectralon, DHR is a measurement of the total light reflected by the panel in all directions from a light source inclined 8° from surface normal. The DHR for the Spectralon SRS-99 panel used in this study is approximately 99% for the visible and near infrared. This value declines steeply at around 1950 nm and approaches 94% reflectance near 2150 and 2500 nm (Figure 3).

The DHR value describes the overall spectral reflectivity of the panel, but the bi-directional reflectance factor (BRF) is used to quantify the angular distribution of the reflected light. The BRF of a surface is the ratio of its reflectance at a given combination of illumination (θ_i) and view (θ_v) angles relative to that from a

perfectly diffuse, 100% reflector. BRF is a more useful descriptor of a reference panel's reflectance characteristics than DHR because the measured radiance from both the reference panel (during instrument calibration) and from ground targets (during data acquisition) are made under specific illumination / observation geometries defined by the elevation of the sun and the look angle of the sensor. Multiplying spectral reflectance values produced by the ASD spectroradiometer by the appropriate Spectralon BRF corrects for deviations of Spectralon reflectance from that of a theoretical perfectly diffuse reflector.

Directional reflectance from diffuse skylight was not modeled, but was assumed to be a minor component. Diffuse irradiance typically composes approximately 15% to 20% of total irradiance in TM band 1, and progressively less in the longer wavelength TM spectral bands, reaching essentially zero in TM bands 5 and 7. The procedure by which Spectralon BRF values were estimated over the entire 350–2500 nm range from illumination angle data is presented in the Appendix.

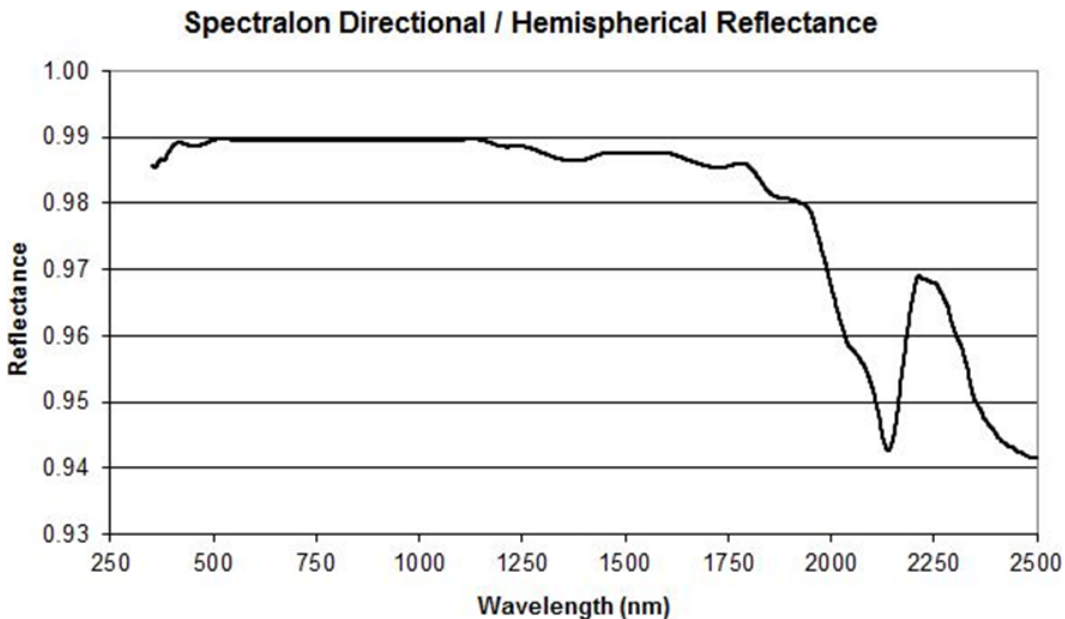


Figure 3. Spectralon SRS-99 directional / hemispheric reflectance by wavelength.

Correcting for Changes in Sun Angle During Flight

The ASD FieldSpec FR spectroradiometer used aboard HydroBio's aircraft was calibrated to solar illumination conditions immediately prior to takeoff using a level Spectralon panel. A Teflon light diffuser mounted in the ceiling of the aircraft's cabin was intended to allow for frequent recalibration of the ASD in-flight. Unfortunately, a test flight determined that intensity of light transmitted through the diffuser varied significantly (~ 10%) with the direction of flight, making its use for in-flight calibration impractical. Therefore, all spectra collected during the flight were relative to the initial pre-takeoff instrument calibration.

During the course of the flight, the sun angle changed, which affected the insolation intensity. For all but the lowest sun angles, the intensity of clear-sky insolation closely follows the cosine of the solar zenith angle. This relationship was exploited to correct recorded ASD reflectance spectra for the effects of changing sun angle during the flight. Equation 7 determined the factor by which a reflectance spectrum was multiplied to correct for changes in sun angle during flight.

$$\theta_{sun_corr,Ti} = \cos \theta_{t0} / \cos \theta_{ti} \quad (7)$$

where:

- $\theta_{sun_corr,Ti}$ = multiplicative sun angle correction at time i
- θ_{t0} = solar zenith angle at the time of instrument calibration
- θ_{ti} = solar zenith angle at the time of spectrum measurement

Correcting for Sensor Calibration Drift in the Airborne Reflectance Data

The 11/2/09 reflectance data acquisition flight was well-timed, with sun angles varying only 1.2 degrees during the measurement of reflectance spectra of the calibration targets. The difference in solar zenith angle between the pre-flight and post-flight Spectralon measurements was only 2.0° (54.76° pre-flight, 56.78° post-flight). Because solar radiation intensity varies with the cosine of the solar zenith angle, the two-degree difference in sun angle pre- and post-flight resulted in about a 5% decrease in post-flight Spectralon reflectance values after the Spectralon BRDF differences were taken into account.

Pre- and post-flight Spectralon reflectance spectra, and the effects of the corrections for Spectralon Bidirectional Reflectance Distribution Function (BRDF) and sun angle changes are shown in Figure 4. Calculations of the BRDF and sun angle corrections are shown in Table 2. The Spectralon reflectance data plotted in Figure 4 show that after correction for sun angle and Spectralon BRDF differences between pre- and post-flight measurements, there was a drift in the calibration of HydroBio’s ASD spectroradiometer of approximately 5% in the 350 nm – 1000 nm range, and about a 9% drift in the 1001 nm – 2500 nm range over the 1 hour, 33 minute time span between measurements.

Having duplicate measurements of a low-reflectance target early and late in the reflectance data acquisition mission would have provided data that could have been used to determine if the sensor calibration drift was entirely bias (additive), entirely gain (multiplicative), or some combination of the two. However, only Spectralon measurements were made on the ground, and the reflectance data acquisition mission was flown in a general counter-clockwise loop which produced no repeat coverage of any ground target. So with only the pre- and post-flight Spectralon data to define the calibration drift, all calibration drift was assumed to be caused by sensor gain degradation alone.

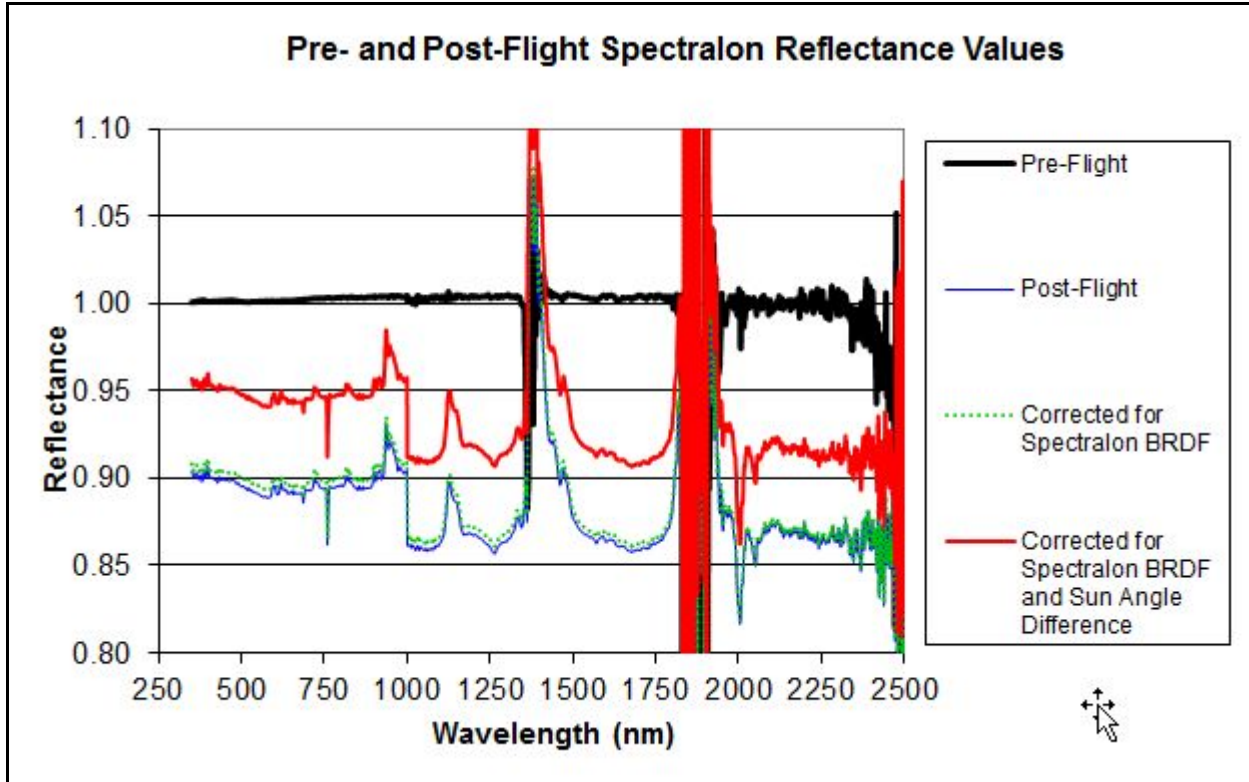


Figure 4. Pre- and post-flight Spectralon spectra, showing the effects of Spectralon BRDF and sun angle corrections. Spikes in the spectral are in portions of the spectrum where atmospheric water vapor absorption is strong, reducing the signal to noise ratio.

Table 2. Sun Angle and Spectralon BRDF Correction Factors Used in the Calculation of the Data Presented in Figure 4

| Spectralon Measurement | Solar Zenith Angle (degrees) | Cosine Solar Zenith Angle | Post-Flight Sun Angle Correction Factor | Average VNIR Spectralon BRDF | Post-Flight Spectralon BRDF Correction Factor |
|------------------------|------------------------------|---------------------------|---|------------------------------|---|
| Pre-flight | 54.76 | 0.5770 | | 0.9723 | |
| Post-flight | 56.78 | 0.5479 | 1.0532 | 0.9675 | 1.0050 |

Post-flight wavelength-specific multiplicative correction factors were calculated as the ratio of pre-flight to post-flight Spectralon reflectance values (after correction for sun angle and Spectralon BRDF differences shown in Figure 4). But prior to generating these correction factors, the pre- and post-flight Spectralon reflectance spectra were filtered to eliminate spectral regions where atmospheric water vapor absorption produced noisy reflectance data (686-688 nm, 711-734 nm, 756-764 nm, 811-838 nm, 896-985 nm, 1081-1250 nm, 1291-1540 nm, and 1745-2130 nm). Then, the pre- and post-flight spectra were smoothed using a 51nm moving average filter. The filter kernels did not operate across the transition at 1000 nm that separates the regions measured by the ASD's silicon

detector array (350–1000 nm) and the region measured by its two indium gallium arsenide (InGaAs) detectors (1001-2500 nm). Finally, gaps in the edited spectrum were linearly interpolated from adjacent regions of the spectrum with valid data.

Figure 5 shows the results of the editing, averaging, and gap filling of the pre- and post-flight Spectralon reflectance data, and the resulting ASD post-flight calibration correction factors. The drift in the VNIR was about half that exhibited in the SWIR. The drop off in the pre-flight Spectralon reflectance values around 2400 nm is unexplained, but this region is not contained within any TM spectral band so it had no impact on the image calibration results.

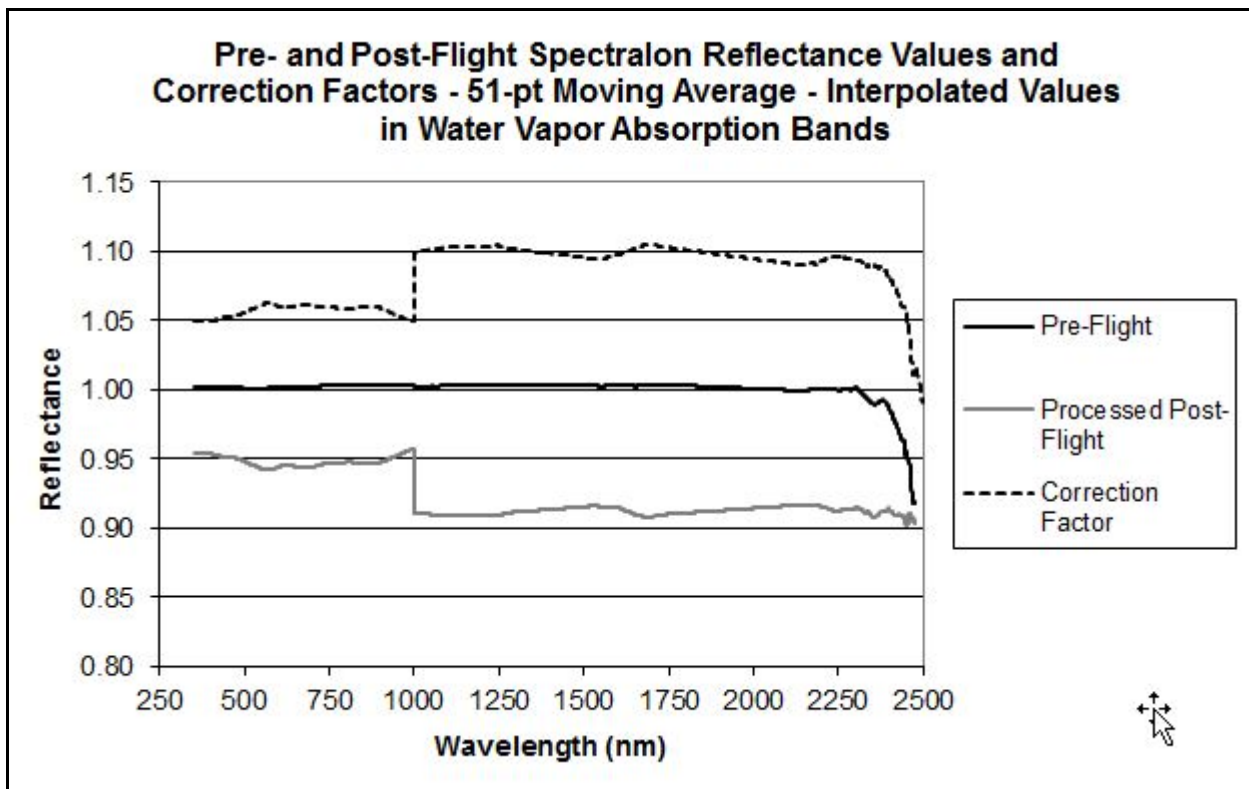


Figure 5. Fully processed pre- and post-flight Spectralon reflectance values and the ASD calibration drift correction factor derived from them.

Calibration drift correction factors were linearly interpolated with time from a value of 1.0 at the time of pre-flight Spectralon measurement to the final correction values at the time of the post-flight Spectralon measurement (Equation 8).

$$\text{Cal}_{corr,T_i,\lambda} = 1 + ((T_i - T_{start}) / (T_{end} - T_{start})) * (\text{Cal}_{corr,T_{end},\lambda} - 1) \quad (8)$$

where:

$$\text{Cal}_{corr,T_i,\lambda} = \text{calibration correction for wavelength } \lambda \text{ at time } T_i$$

T_{start} = time of pre-flight Spectralon panel measurement
 T_{end} = time of post-flight Spectralon panel measurement
 T_i = time of target measurement
 $Cal_{corr,Tend,\lambda}$ = calibration correction for wavelength λ at the time of the post-flight Spectralon panel measurement

Sporadic Occurrence of Step Function at 1001 nm

Inspection of spectra of the five calibration targets revealed that the abrupt change in reflectance values at 1001 nm (at the transition from the VNIR detector array to the SWIR1 detector) was only present in the desert pavement spectrum. The desert pavement site was the fourth calibration target, measured 41 minutes after instrument calibration (44% through the 93 minute time period between the pre- and post-flight Spectralon readings). The temporally interpolated VNIR and SWIR correction factors effectively removed the drop in recorded reflectance values at 1001 nm. For the remaining four calibration sites, no discontinuities in the spectra at 1001 nm were present. For these spectra, the average VNIR correction factor for the 986-1000 nm range was used for the entire SWIR data range (1001–2500 nm).

Generating Surface Reflectance Values for Calibration Targets in the Thematic Mapper Spectral Bands

Candidate ASD spectra for each calibration target were identified using the GPS track log and flight video. Each candidate spectrum was inspected to ensure that no outliers existed in the spectrum set (none were found). Then, all spectra for each target were averaged into a single spectrum. The averaged spectrum was corrected for the pre-flight Spectralon BRF and for sun angle and sensor calibration changes with time.

Convolution of ASD reflectance values to much coarser TM spectral bands was accomplished using the spectral response functions of the six reflective TM bands. Spectral response functions are composed of a series of coefficients between 0 and 1 which define the relative sensitivity of the TM spectral band to specific wavelengths of light, relative to the wavelength of maximum sensitivity. Spectral response values are recorded at 1 nm spectral increments. Equation 9 shows how these values were converted to TM spectral band reflectance values.

$$\rho_{TM\#} = (\sum_{\lambda_{min\#}, \lambda_{max\#}} \rho_{\lambda} * f_{\lambda}) / (\sum_{\lambda_{min\#}, \lambda_{max\#}} f_{\lambda}) \quad (9)$$

where:

$\rho_{TM\#}$ = reflectance in TM band #
 $\lambda_{min\#}$ = minimum wavelength of the sensor response function for TM band #
 $\lambda_{max\#}$ = maximum wavelength of the sensor response function for TM band #
 ρ_{λ} = measured spectral reflectance at wavelength λ
 f_{λ} = sensor response function at wavelength λ

Correcting Surface Reflectance Values for Variations in Local Sun Angle

As with the TOA reflectance imagery, the reflectance values recorded from the aircraft were apparent surface reflectance values; that is, they were corrected for variable sun angles, but not for variations in illumination due to terrain slope and aspect. If the airborne reflectance data had been acquired concurrently with the image data being corrected, terrain effects would be irrelevant because they would be identical on both data sets. However, the effect of terrain slope and aspect on surface illumination varies with the position of the sun. Therefore, coefficients were calculated to compensate for any differences in local illumination conditions present at the times of reflectance data acquisition and image acquisition.

The Soda Lake, greasewood, and desert pavement sites all had slopes of near zero degrees, so illumination was accurately modeled by sun angle corrections. The Desert Shrub target had an average slope of 1.6°, while the flight line tracks over the sand plain to the southwest of Sand Mountain averaged 1.3°. For these two sites, the effect of variable illumination was corrected using Equation 10. Illumination angles were calculated using terrain slope and aspect values calculated from a 1/3 arc second NED DEM that was reprojected into the project's zone 11 UTM grid system with a 10-meter grid cell size.

$$\rho_{TM\#_corr} = \rho_{TM\#} * (\cos \theta_{iI} / \cos \theta_{sunI}) / (\cos \theta_{iR} / \cos \theta_{sunR}) \quad (10)$$

where:

- $\rho_{TM\#_corr}$ = surface reflectance in TM band # corrected for variable illumination conditions
- $\rho_{TM\#}$ = surface reflectance in TM band # measured from aircraft
- θ_{iI} = local illumination angle (relative to surface normal) during image acquisition
- θ_{sunI} = solar zenith angle during image acquisition
- θ_{iR} = local illumination angle (relative to surface normal) during airborne reflectance data acquisition
- θ_{sunR} = solar zenith angle during airborne reflectance data acquisition

Processing Surface Reflectance Data

The reflectance data collected at the surface by Reclamation on 9/25/09 were much easier to process than the airborne data. Calibration drift was not an issue because spectra were measured immediately after instrument calibration. All of the other processing steps (correction for Spectralon BRF, variations in local sun angles relative to a flat surface, and convolution to TM spectral band reflectances) were performed in the manner described for the airborne reflectance data.

Calibrating Thematic Mapper Images to Apparent Surface Reflectance

TOA reflectance images were calibrated to surface reflectance using linear regression equations calculated from paired TOA and surface reflectance data (Equation 11). The initial set of reflectance calibration models were derived using the surface reflectance data acquired solely from the air. TOA reflectance values paired with the surface reflectance data came from the average of image pixels intersecting the aircraft ground track. The only exception to this rule was Soda Lake, where image TOA reflectance values were calculated as the average of all water pixels that were at least three pixels from the shore, and not visibly affected by sun glint off the water surface (as determined by viewing a severely contrast-stretched TM band 5 image). Plots of TOA reflectance from the 11/1/09 TM image versus processed surface reflectance data acquired from HydroBio's aircraft on 11/2/09 are shown as blue points in Figure 6, and regression coefficients and model r^2 values are reported in Table 3.

$$\rho_{TM\#} = \alpha_{TM\#} + (\beta_{TM\#} * \rho_{toa,TM\#}) \quad (11)$$

where:

- $\rho_{TM\#}$ = surface reflectance in TM band #
- $\alpha_{TM\#}$ = regression model intercept for TM band #
- $\beta_{TM\#}$ = regression model slope for TM band #
- $\rho_{toa,TM\#}$ = top-of-the-atmosphere reflectance for TM band #

Table 3. Initial (from Airborne Reflectance Measurements) and Final (from Airborne Measurement of Soda Lake and Ground-Level Measurement of Sand Mountain) Regression Models Used to Calibrate 11/1/09 TOA Reflectance Images to Apparent Surface Reflectance

| Spectral Band | 5-pt Regression Intercept (aircraft refl. data only) | 5-pt Regression Slope (aircraft refl. data only) | 5-pt Regression r^2 | Final 2-pt Regression Intercept (aircraft and ground refl. data) | Final 2-pt Regression Slope (aircraft and ground refl. data) |
|---------------|--|--|-----------------------|--|--|
| TM1 | -0.1122 | 1.4813 | 0.9963 | -0.1086 | 1.4918 |
| TM2 | -0.0612 | 1.2811 | 0.9985 | -0.0594 | 1.3171 |
| TM3 | -0.0350 | 1.1770 | 0.9990 | -0.0343 | 1.2339 |
| TM4 | -0.0216 | 1.0610 | 0.9990 | -0.0212 | 1.1516 |
| TM5 | -0.0053 | 1.0584 | 0.9991 | -0.0045 | 1.1707 |
| TM7 | -0.0020 | 1.0953 | 0.9992 | 0.0003 | 1.1669 |

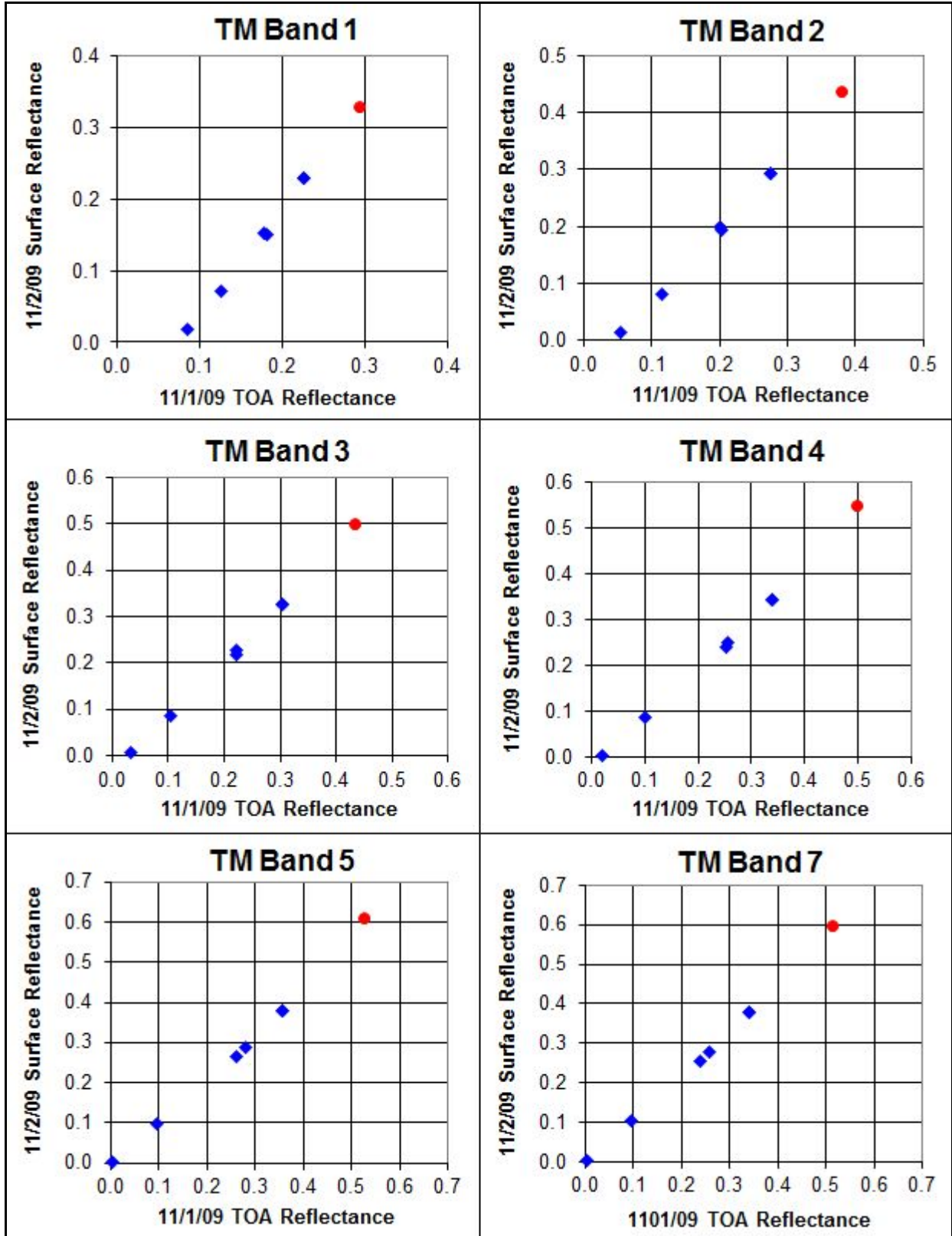


Figure 6. Plots of surface reflectance values from the 11/2/09 HydroBio flight (blue diamonds) and 9/25/09 Reclamation ground data acquisition (red circles) with TOA reflectance values from the 11/1/09 P42R33 TM image.

The linear regression models generated from the TOA and airborne reflectance data shown in blue in Figure 6 were very robust, with the coefficients of determination for all bands exceeding 0.996. But because these targets were to be used to calibrate all of the TM scenes used in this study, their reflectance values had to be extremely stable over the course of the year. Although all five calibration targets exhibited annual variation in TOA reflectance that was among the lowest in the TM image swath containing the study area, the three vegetated targets showed slight predictable reflectance variation caused by variable shading of the ground by the vegetation canopy, and changes in canopy reflectance due to phenological changes over the course of a year. The other two calibration targets (Soda Lake and the Sand Mountain) were unvegetated and therefore not affected by these factors. Furthermore, they were the most spatially homogeneous of the calibration targets, showed little sensitivity to antecedent precipitation events, and exhibited the lowest and highest recorded reflectance values in all TM spectral bands. Therefore, the final models used to calibrate all of the TOA reflectance images to apparent surface reflectance were derived from surface reflectance data acquired at only the Soda Lake and Sand Mountain targets.

But the Sand Mountain reflectance data acquired from HydroBio's aircraft were called into question for three reasons. First, more than 70 minutes had elapsed between the spectroradiometer calibration and data acquisition at Sand Mountain. Although steps were taken to model and remove the effects of sensor calibration drift, if the assumption of linear sensor gain decay with time was incorrect, the predicted reflectance values would be in error. Second, TM4 surface reflectance values of the Sand Mountain target were almost identical to the TOA reflectance values, indicating an underestimation of TM4 surface reflectance because the atmosphere normally attenuates some of the signal from such a bright target. Finally, surface measurements of soil background reflectance taken in September, 2012 showed a consistent offset between the $NDVI_0$ image (discussed later) and NDVI values calculated from soil background surface reflectance measurements.

For these three reasons, the final reflectance calibration models were developed using HydroBio's aircraft-measured surface reflectance measurements of Soda Lake (acquired 22 minutes after sensor calibration), and Reclamation's ground-based measurements of sand reflectance (after correction for differences in illumination angle using Equation 10). The TOA reflectance values paired with the ground-based measurements came from south southeast-facing slopes (mean slope and azimuth of 23° and 162° , respectively) of tall dunes in the Sand Mountain complex. These slopes were chosen because their slopes were assumed to be stable, they were completely unvegetated, they experience relatively high local solar incidence angles at the time of Landsat image acquisition during all months of the year, and the relatively high sun angles and well-drained sand surface guarantee quick drying of the surface after precipitation events. Table 3 contains the additive and multiplicative surface reflectance calibration coefficients developed using the airborne reflectance data alone, and those developed using

airborne reflectance measurements for Soda Lake and ground-based measurements for the Sand Mountain area.

NDVI* Analysis

The NDVI* procedure was used to estimate ET_g for the DVHA for each of five years from 2007 through 2011. This procedure consisted of 1) acquiring meteorological data to establish ETo and precipitation, 2) mapping the phreatophyte zone for which groundwater ET will be estimated, 3) generating mid-summer NDVI images using Equation 1 that capture phreatophytes in a full-canopy condition 4) characterizing the soil background NDVI values (NDVI₀) that would be scaled to zero during the calculation of NDVI*, 5) rescaling summertime NDVI images to NDVI* using Equation 2, and 6) estimating groundwater ET from each NDVI* image. These steps are discussed below.

Obtaining Annual ETo and Precipitation Data

The USGS collected the standard complement of agricultural weather station data at a weather station located 18 km northeast of the Dixie Valley playa from August, 2009 through December, 2012. The USGS also operated four eddy covariance stations at locations near the south end of the playa from March, 2009 through October, 2011. Two of these eddy stations were located on the playa, while the remaining two were located in sparsely vegetated (SV) and densely vegetated (DV) phreatophyte areas (Figure 7). Data from the weather station were used to compute the water year 2010–2012 ETo using the American Society of Civil Engineers (ASCE) Standardized Penman-Monteith equation (ASCE-EWRI, 2005). Data gaps in the weather station data stream were filled with data from the SV eddy covariance station—the eddy covariance site whose environmental conditions most closely represented those at the weather station.

For Dixie Valley, ETo estimates were needed for the water years prior to the installation of the weather station (water years 2007-2009). The other basins in the DVHA contained no weather stations, so they required ETo estimates for the entire water year 2007-2011 time period. ETo estimates for unmeasured time periods and locales were generated from gridded weather datasets. Daily ETo was calculated from daily PRISM maximum and minimum air temperature and dew point data, and hourly NLDAS-2 solar radiation and wind speed data aggregated to daily values. The NLDAS-2 data were downscaled to the 2.5 arc minute grid spacing of the PRISM data (approximately 4-km) using bilinear interpolation resampling. For each basin within the DVHA, ETo was characterized from a carefully selected 4-km grid cell whose location and elevation closely matched those of each basin's phreatophyte zone.

Estimating Groundwater Discharge from Phreatophyte Transpiration in Dixie Valley, Nevada

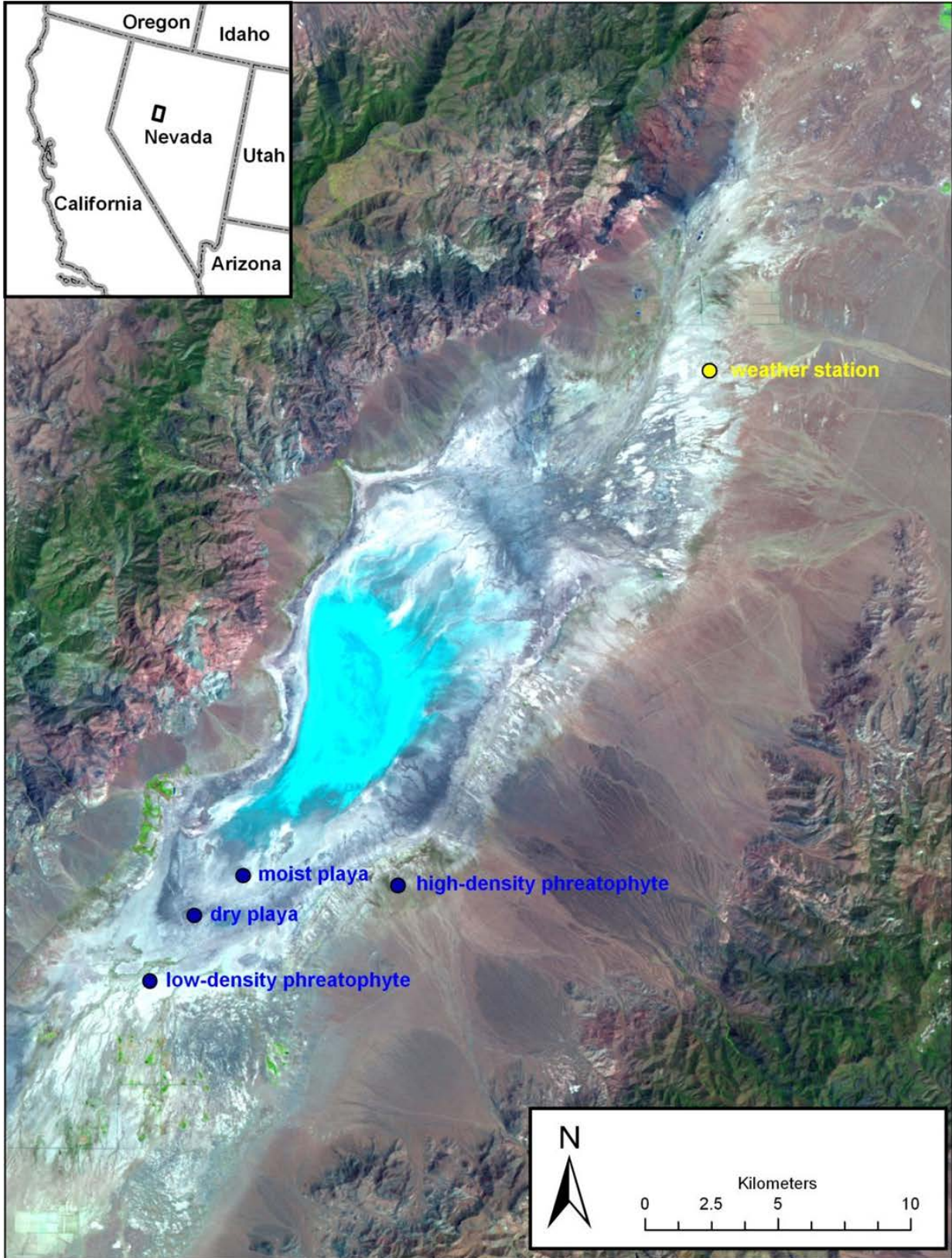


Figure 7. Locations of the Dixie Valley weather station (yellow), and the four eddy covariance flux towers (blue) shown on the 7/31/10 TM scene (TM 5, 4, 3 = R, G, B).

Gridded PRISM/NLDAS-2 ETo was generally greater than weather station ETo for the colder months and less than weather station ETo in the warmer months. Monthly correction factors were developed to produce better matches between the two ETo estimates. Correction factors were defined as ratios of ETo from the Dixie Valley weather station to ETo from the PRISM/NLDAS-2 grid cell containing the station. Summed daily ETo data for the subject month over the entire August 5, 2009 – December 31, 2012 weather station data record were used in the calculations. Final monthly correction factors for December, January, and February were modified slightly by Justin Huntington of Huntington Hydrologic to smooth out month-to-month variation in the data most likely resulting from the ratioing of small values present during the late fall and early winter months (Table 4). The final monthly correction factors were multiplied by monthly PRISM/NLDAS-2 ETo estimates for each basin in the DVHA, and monthly results were summed to provide the required ETo estimates by water year.

Table 4. Calculated and Final PRISM/NLDAS-2 ETo Correction Coefficients by Month

| Month | Calculated Ratio | Final Ratio |
|-----------|------------------|-------------|
| January | 0.833353 | 0.870000 |
| February | 1.077229 | 0.950000 |
| March | 0.962537 | 0.962537 |
| April | 0.984785 | 0.984785 |
| May | 1.028962 | 1.028962 |
| June | 1.096837 | 1.096837 |
| July | 1.144673 | 1.144673 |
| August | 1.116011 | 1.116011 |
| September | 1.110126 | 1.110126 |
| October | 1.045066 | 1.045066 |
| November | 0.946380 | 0.946380 |
| December | 1.011121 | 0.950000 |

Annual precipitation estimates for Dixie Valley in water years 2007–2009, and for 2007–2011 for the other DVHA basins were derived by summing daily gridded PRISM precipitation data. An annual correction factor for the 4-km gridded PRISM precipitation data was calculated by dividing the undercatch-corrected bulk precipitation total for the 2010 and 2011 water years measured at the SV station by the PRISM precipitation total for the same time period and location. Precipitation estimates for other basins and for the 2007-2009 time period were generated by multiplying the PRISM estimates by the correction factor (1.13). The annual ETo and precipitation data used to calculate ETg for water years 2007-2011 are shown in Table 5.

Table 5. Grass Reference Evapotranspiration (ET_o) and Annual Precipitation for the DVHA for Water Years 2007–2011

| Year | Parameter | Stingaree | Cowkick | Eastgate | Dixie | Pleasant | Jersey | Edwards Creek |
|------|----------------------|-----------|---------|----------|-------|----------|--------|---------------|
| 2007 | ET _o (mm) | 1541 | 1534 | 1516 | 1647 | 1614 | 1629 | 1518 |
| | Precipitation (mm) | 91 | 108 | 133 | 90 | 229 | 170 | 156 |
| 2008 | ET _o (mm) | 1507 | 1500 | 1484 | 1631 | 1588 | 1604 | 1487 |
| | Precipitation (mm) | 146 | 160 | 182 | 131 | 226 | 182 | 175 |
| 2009 | ET _o (mm) | 1458 | 1452 | 1430 | 1568 | 1522 | 1544 | 1444 |
| | Precipitation (mm) | 194 | 219 | 255 | 157 | 305 | 285 | 270 |
| 2010 | ET _o (mm) | 1377 | 1367 | 1360 | 1511 | 1473 | 1494 | 1392 |
| | Precipitation (mm) | 156 | 171 | 192 | 140 | 243 | 194 | 157 |
| 2011 | ET _o (mm) | 1351 | 1341 | 1334 | 1508 | 1485 | 1509 | 1378 |
| | Precipitation (mm) | 175 | 200 | 236 | 187 | 340 | 273 | 207 |

Defining the Phreatophyte Zones

As described in Baugh and Groeneveld, 2006, areas to which the NDVI* method can be applied must exist in an arid to semi-arid environment where potential evaporation is far greater than precipitation (clearly met in the DVHA) and must meet three other conditions. The area: 1) must be underlain by shallow groundwater, 2) must be vegetated with phreatophytic plants transpiring groundwater, and 3) must have water tables that generally remain deeper than the limit of capillary rise. The USGS, HydroBio, and Reclamation cooperated to define a phreatophyte zone for Dixie Valley that met these requirements.

Analysts used multidecadate Landsat imagery, high-resolution National Agricultural Imagery Program (NAIP) imagery, oblique aerial imagery acquired by HydroBio, and field observations to define the upper and lower limits of phreatophytic vegetation. Reclamation defined the phreatophyte zones for the remaining basins within the DVHA. Oblique aerial photography was only available for Dixie Valley itself, so Reclamation used NAIP, Landsat TM, and ground reference data for the task. The final phreatophyte zones for the DVHA are shown in Figure 8.

Detailed analysis by the USGS of ET and piezometer data at the four eddy covariance stations shown in Figure 7 determined that groundwater evaporation from the soil surface was near zero at all four locations, in spite of mean depths to groundwater as small as 0.3 meters (Garcia et al., 2014). Although the hydrology of Dixie Valley is very complex, with confined aquifers, faults, and springs occurring in many locations, depth to groundwater generally increased with distance from the playa. Three piezometers located along the southern boundary of the phreatophyte zone each recorded mean depth to groundwater of approximately 10 meters. The Dixie Team agreed that the assumption that the water table was below the limits of capillary rise was met in nearly all locations

within the Dixie Valley phreatophyte zone, and it was therefore suited to the application of the NDVI* method. Similar conditions were assumed present in the other DVHA phreatophyte zones.

Generating “Leaf-On” NDVI Images

The NDVI* method of estimating phreatophyte ET_g requires a summertime “leaf-on” NDVI image to characterize the vegetation canopy development of phreatophytic vegetation. Five TM images acquired on 8/8/07, 7/25/08, 7/28/09, 7/31/10, and 8/3/11 were investigated to assess their potential to characterize the mid-summer “leaf-on” condition. NDVI images were generated from surface reflectance images masked to eliminate the Dixie and Edwards Creek Valley playas, then smoothed using a 3x3-pixel averaging filter.

Generating the “Leaf-Off” NDVI₀ Image

The formulation of NDVI makes it sensitive to the quantity of green leaf vegetation, but in areas of sparse vegetation cover, NDVI is also sensitive to the composite reflectance of the soil surface. Dead herbaceous plant material, plant litter and woody stems may also become a significant component of the soil background reflectance as plant densities increase. Groeneveld et al. (2007) showed that correlation of NDVI values with desert phreatophyte ET is enhanced if these soil background effects are removed. Groeneveld et al. (2007) used image statistics from a mid-summer NDVI scene to define a single NDVI₀ value for each TM image being processed.

Early in the project, the ability of a single NDVI₀ value to characterize the variation in soil background reflectance was called into question. Inspection of NDVI, MSAVI, and EVI images generated from TOA reflectance imagery revealed significant variation across the phreatophyte zone; and much of this variation appeared to be more related to variations in soil background color than to variations in shrub density as observed on 1-meter resolution NAIP imagery. Bare soil reflectance spectra measured during a subsequent field trip at five locations within the southern portion of Dixie Valley (Figure 9) documented some of this variation. The spectra, measured with Reclamation’s ASD FieldSpec-FR spectroradiometer, were converted to Landsat TM reflectance values using the TM sensor response functions (Equation 9), and then converted to NDVI, MSAVI, and EVI values (Table 6). While these data did not capture the full range of spectral variability of soils within the phreatophyte zone, they showed that much of the observed variation in the NDVI, MSAVI, and EVI images was caused by variations in background soil reflectance, and was unrelated to the quantity or vigor of phreatophytic vegetation. Given that the range of bare soil NDVI values in Table 6 was similar to the observed differences between dense phreatophyte stands and their sparsely vegetated surroundings, it was clear that an image of spatially varying NDVI₀ values was needed to adequately characterize soil background NDVI.

Estimating Groundwater Discharge from
Phreatophyte Transpiration in Dixie Valley, Nevada

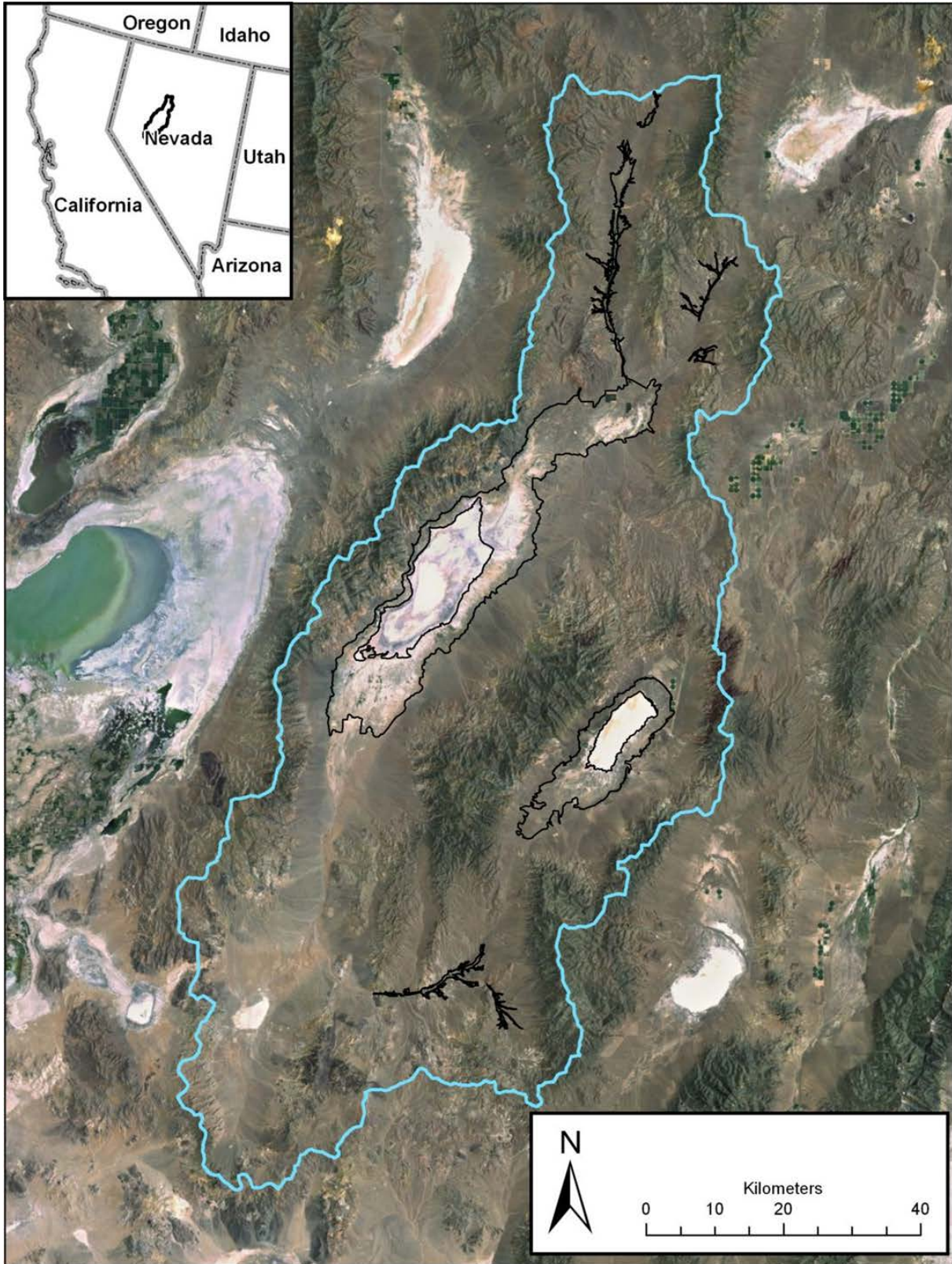


Figure 8. Phreatophyte zones (outlined in black) of the Dixie Valley hydrographic area (outlined in blue). Playas defined by inner polygons within Dixie and Edwards Creek Valleys were not included in NDVI* analyses.

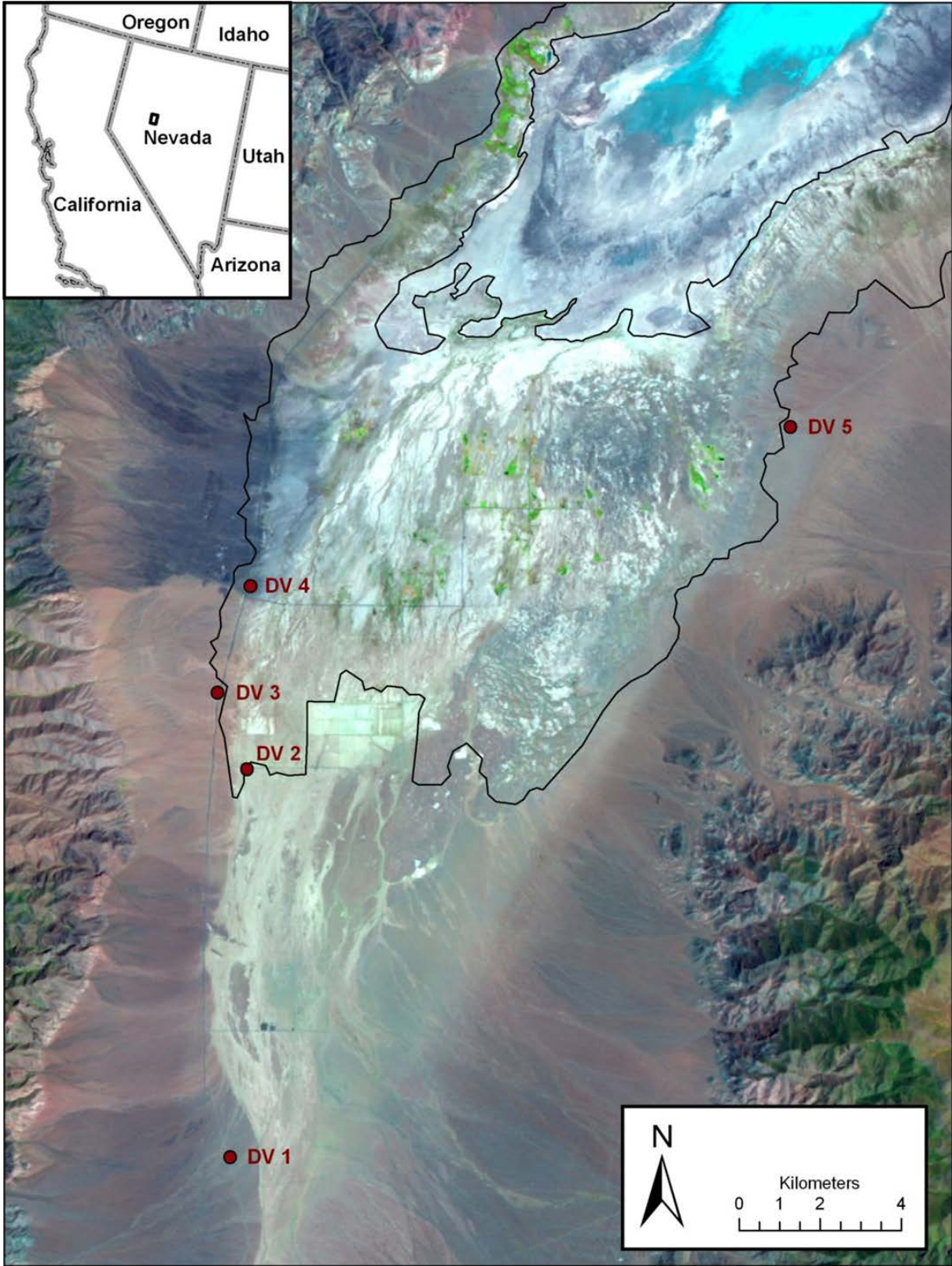


Figure 9. Locations near the southern portion of the Dixie Valley phreatophyte zone (in black) at which soil reflectance was measured on 6/18/09. Background image is the 7/31/10 TM scene (TM 5, 4, 3 = R, G, B).

Table 6. Surface Reflectance Values in the TM Spectral Bands and Derived NDVI and MSAVI Values for Soils in the Dixie Valley Area

| Target | TM1 refl | TM2 refl | TM3 refl | TM4 refl | TM5 refl | TM7 refl | NDVI | MSAVI | EVI |
|--------|----------|----------|----------|----------|----------|----------|--------|--------|--------|
| DV1 | 0.152 | 0.199 | 0.231 | 0.256 | 0.234 | 0.228 | 0.0505 | 0.0333 | 0.0433 |
| DV2 | 0.252 | 0.338 | 0.390 | 0.433 | 0.487 | 0.465 | 0.0519 | 0.0469 | 0.0594 |
| DV3 | 0.133 | 0.179 | 0.207 | 0.251 | 0.349 | 0.324 | 0.0968 | 0.0615 | 0.0765 |
| DV4 | 0.136 | 0.168 | 0.180 | 0.185 | 0.193 | 0.176 | 0.0141 | 0.0075 | 0.0104 |
| DV5 | 0.160 | 0.220 | 0.261 | 0.295 | 0.304 | 0.293 | 0.0598 | 0.0430 | 0.0532 |

Late Fall and Winter NDVI Images as a Solution to Spatially Variable NDVI₀

Because of typical summer and early fall drought and the cold winters experienced in the study area, phreatophytes such as greasewood, rabbit brush, and big saltbush typically lose their leaves by late fall or early winter, while understory grasses and forbs die off. Therefore, an NDVI image generated from a late-fall or winter “leaf-off” scene was seen as the only efficient and effective way to map spatially varying estimates of NDVI₀ across the study area.

Challenges Involved with Using a Separate “Leaf-Off” Scene

Using a “leaf-off” image to quantify NDVI₀ introduces complications that are avoided when a simple scalar NDVI₀ value is estimated from the summer scene itself. When a scalar NDVI₀ value is used, the effect of any error in image reflectance calibration is minimized during the normalization procedure. The zero vegetation NDVI value is set to zero and the fully vegetated NDVI value is set to 1.0 regardless of any calibration errors in the parent image. However, using different images to represent leaf-on and leaf-off conditions of the same area means that NDVI* values will be sensitive to anything that alters the soil background NDVI of the leaf-off scene relative to that of the leaf-on scene. Those factors include random image noise, and variations in illumination angle, atmospheric conditions, soil moisture, and concentrations of dead herbaceous vegetation, which are discussed below.

Influence of Random Image Noise

Like any sensor, measurements of spectral radiance made by the Landsat TM sensor contain some error. Random noise in the data that will produce fluctuations in recorded image radiance values from a completely homogenous target. These radiance variations are carried through the processing flow to produce fluctuations in surface reflectance values in the calibrated images. These fluctuations are typically very small (standard deviations of pixels from the homogeneous surface of Soda Lake for all images used in this analysis averaged 0.2 and 0.25% reflectance for TM3 and TM4, respectively), but their magnitudes are independent of overall reflectance value, and effects can be amplified when the image data are used to generate spectral band ratios, such as NDVI. This

random noise was reduced by a factor of three by running a 3x3-pixel low-pass (averaging) filter over the surface reflectance image data prior to generating NDVI images. The spatial resolution of the image data was effectively increased to 90-meters by this operation, but it had a secondary beneficial effect of reducing the impact of any slight spatial misregistration between multirate TM images.

Influence of Illumination Angle

The difference in sun angle between the summer leaf-on and late fall to winter leaf-off scenes is significant. Sun angles during image acquisition on 6/26/09 (64.3°) and 12/3/09 (25.3°) differed by 39°. For surface measurements, NDVI from dense vegetation shows sensitivity to illumination angle because increased multiple scattering of NIR light in the vegetation canopy at lower sun angles increases NIR reflectance, while reflectance of highly absorbed red light changes little, resulting in increased NDVI (Jackson and Huete, 1991). But illumination angle has only a minimal effect on NDVI measurements non-vegetated areas (Los et al., 2002). Any NDVI variations most likely arise from slight differences in the BRDF of surface materials, and the effects of increased surface shading at low sun angles. In shaded areas, slightly increased diffuse irradiance in the red spectral band relative to the NIR band could reduce NDVI values. However, due to the typically sparse vegetation in the DVHA and the close spectral proximity of the red and NIR bands, this effect was assumed to be minimal.

Influence of Atmospheric Scattering and Absorption

The effects of atmospheric scattering and absorption on TOA reflectance values make the influence of sun angle on NDVI less predictable. For densely vegetated targets, low TM3 reflectance values are increased, and high TM4 reflectance values are decreased by the increased atmospheric scattering and absorption arising from the longer atmospheric path lengths at low sun angles. These two factors have the combined effect of decreasing NDVI of vigorous vegetation targets. The effect of increased atmospheric path length on the NDVI of sparsely vegetated areas is less predictable and depends on the land surface reflectance properties and composition of the atmosphere.

Calibration of the TM imagery to apparent surface reflectance was performed to minimize atmospheric effects. Great care was taken during the calibration of each TM image to surface reflectance to ensure that the NDVI, EVI, and MSAVI values derived from these reflectance data were well-correlated with surface conditions.

Influence of Soil Moisture

A visual inspection of a time series of TM images of the Dixie Valley playa and phreatophyte zone at the beginning of this project showed that spectral reflectance and NDVI values varied widely from location to location, and with time at a single location. Precipitation data from the two closest pre-existing weather stations (Centroid and Fallon) were inspected to determine if patterns on the images correlated with antecedent precipitation events. The Centroid weather station maintained by the U.S. Navy started operation in October of 2005, and is

located 60 km south of the Dixie Valley playa near the southern boundary of Dixie Valley. The Fallon AgriMet station maintained by Reclamation started operation in October, 1991, and is located on the west side of the Stillwater Range, about 80 km southwest of the Dixie Valley playa.

Identifying definitive relationships between precipitation events and patterns seen on the image was difficult. Precipitation events are infrequent in the study area, and rarely occur immediately before a successful (i.e., cloud-free) satellite image acquisition where their effects can be unambiguously observed. Furthermore, precipitation in the study area is often localized, so a significant precipitation event recorded at either the Fallon or Centroid weather station may not have produced any precipitation in Dixie Valley, and vice versa. An example of the spatial heterogeneity of precipitation in the study area can be seen in the Centroid and Fallon precipitation data. For the January 2006 through December 2011 time period, the precipitation totals from the Centroid and Fallon weather stations agreed to within 10 percent (601 mm for the Centroid, 660 mm for Fallon). However, monthly precipitation totals could vary widely, as seen in Figure 10.

Influence of Dead Herbaceous Vegetation

Variable soil moisture, in combination with variable grazing intensity during previous months also can have an effect on leaf-off NDVI values. Carpets of dead grass or other herbaceous material can produce higher NDVI values than the underlying bare soil. Concentrations of this material vary both in space and time.

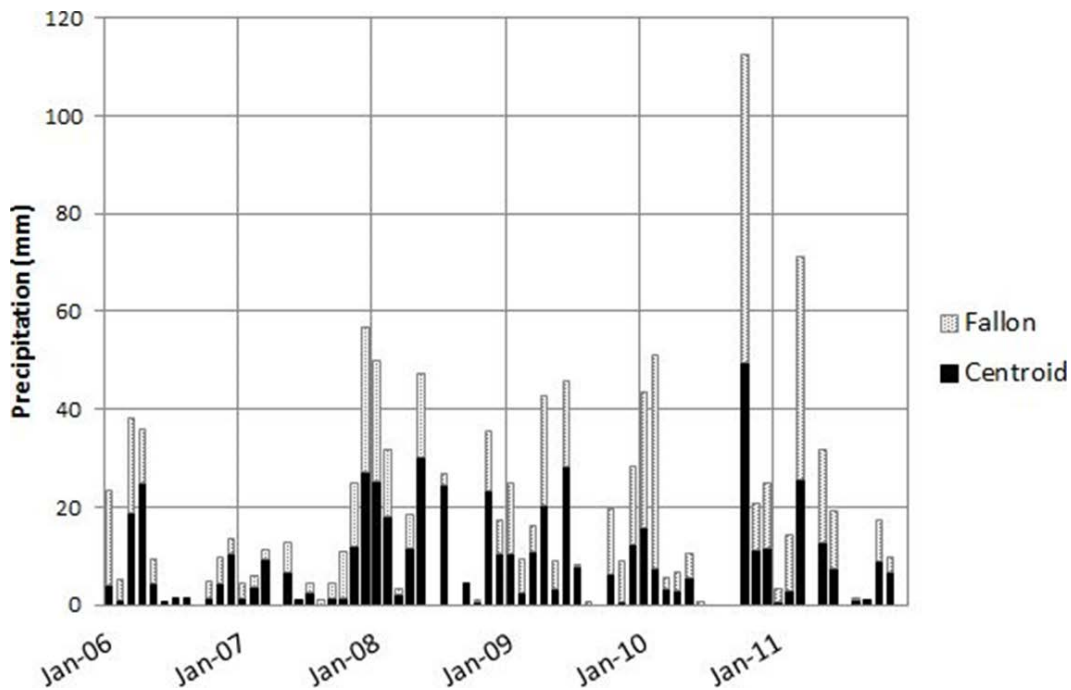


Figure 10. Stacked bar chart comparing monthly precipitation totals for the Centroid and Fallon weather stations.

Generating a Composite “Leaf-Off” Image

Finding a leaf-off scene with low soil moisture conditions similar to those seen in mid-summer was desired. But because of the spotty nature of rainfall in the Dixie Valley area, any point precipitation measurement could not be counted upon to be an accurate representation of the precipitation history of any location more than a few kilometers from the precipitation gauge. Furthermore, weather systems that produced no precipitation in the lower elevations at which precipitation is recorded can produce precipitation in the surrounding mountains; and such precipitation occasionally produces flow into the washes draining into Dixie Valley, producing elevated NDVI values in those areas. Even dead herbaceous vegetation resulting from rainfall events earlier in the year can produce elevated NDVI values that are present one year and gone the next.

To deal with the spatial and temporal variability of precipitation and the associated vegetation response, a decision was made to designate the $NDVI_0$ value for each pixel to be the minimum NDVI value from a number of candidate leaf-off TM scenes. The Landsat image archive was searched along with the Fallon, Centroid, and Dixie Valley weather station data to find clear images that were acquired in a period of low precipitation and low temperatures in the late fall or winter seasons. Six images were identified that met these criteria (3/3/02, 11/22/05, 3/17/07, 11/1/09, 11/17/09, and 12/3/09), and they were used to define the $NDVI_0$ image. Using the minimum leaf-off NDVI from these six candidate images helped to ensure that $NDVI_0$ values would not be anomalously high due to elevated soil moisture content or ephemeral high concentrations of dead herbaceous material.

Replacing Elevated Leaf-Off NDVI Values

Carefully calibrating the TM images and defining $NDVI_0$ values as the minimum NDVI from six candidate “leaf-off” TM scenes addressed the most significant issues related to quantifying a spatially variable $NDVI_0$. However, two additional problems remained: elevated late fall and winter NDVI values in spring-fed and dense phreatophyte areas, and reduced late fall and winter NDVI from salt-covered areas.

Spring-fed Areas

Areas within the DVHA that were moist throughout the year because of artesian spring flow always maintained wintertime NDVI values that were significantly greater than their surroundings. The causes of this phenomenon are uncertain, but are probably linked to the higher concentration of herbaceous vegetation around these springs, which in either its live or dead/dormant condition produces NDVI values that are greater than surrounding bare soil areas. USGS personnel delineated polygons defining spring-fed areas exhibiting elevated NDVI values year-round. These areas and similar areas in phreatophyte zones of the adjacent valleys in the DVHA were masked from the surface reflectance imagery prior to low-pass filtering and generation of the six leaf-off NDVI images from which the $NDVI_0$ image was generated. $NDVI_0$ values for the masked areas were obtained

from the surrounding areas using a series of spatial filtering operations. The masked $NDVI_0$ image was first smoothed using a 9x9-pixel low-pass (moving average) filter, then the smoothed data were progressively moved into the “holes” occupied by spring-fed vegetation using a sequence of 9x9, 17x17, and 33x33 low-pass filters which used only valid data in their calculations, but produced output only in the masked (spring-fed) areas. $NDVI_0$ data for the masked areas were then inserted back into the original masked $NDVI_0$ image.

Dense Phreatophyte Areas

Although most shrubs in the DVHA phreatophyte zones are classified as drought or winter deciduous, USGS field teams reported that some big saltbush and rabbitbrush plants in dense phreatophyte stands retained some of their leaves during the winter months, thereby raising concerns that the $NDVI_0$ estimates generated from the six leaf-off NDVI scenes might overestimate the true soil background NDVI.

In an effort to assess the accuracy of the $NDVI_0$ image, Reclamation collected soil reflectance spectra at 11 locations representing a wide range of $NDVI_0$ values in the Dixie and Edwards Creek Valleys in September, 2012 (Figure 11). At each of these locations, soil reflectance data were collected continuously along four transects oriented in the cardinal directions separated by 10 meters, each measuring 30 m to 60 m in length. Because phreatophytic shrubs still had green leaves at the time of reflectance measurement, reflectance data were not collected along portions of transects that crossed shrub canopies. About 250 measurements of soil background reflectance were taken at most sites, and these data were averaged to generate a single estimated soil background reflectance spectrum for each site. Averaged spectra were converted to reflectance values in the TM spectral bands using Equation 9, and then to NDVI values using Equation 1.

Comparison of the field-measured soil NDVI with corresponding $NDVI_0$ image values shows a strong relationship between the two data sets ($r^2 = 0.98$, Figure 12). The linear least squares regression model predicting surface-measured soil background NDVI from image $NDVI_0$ (Equation 12) has a near-zero intercept, indicating that there is little additive bias to $NDVI_0$ values at the low end of the distribution. But the 1.1021 multiplicative coefficient indicates a tendency for the $NDVI_0$ image to underestimate soil background NDVI values as $NDVI_0$ values increase, which would lead to slight overestimates of $NDVI^*$.

$$NDVI_{soil} = 0.0016 + 1.1021 (NDVI_{0 \text{ image}}) \quad (12)$$

where:

$$\begin{aligned} NDVI_{soil} &= \text{NDVI calculated from field-measured soil background} \\ &\quad \text{reflectance} \\ NDVI_{0 \text{ image}} &= \text{soil background NDVI value from the } NDVI_0 \text{ image} \end{aligned}$$

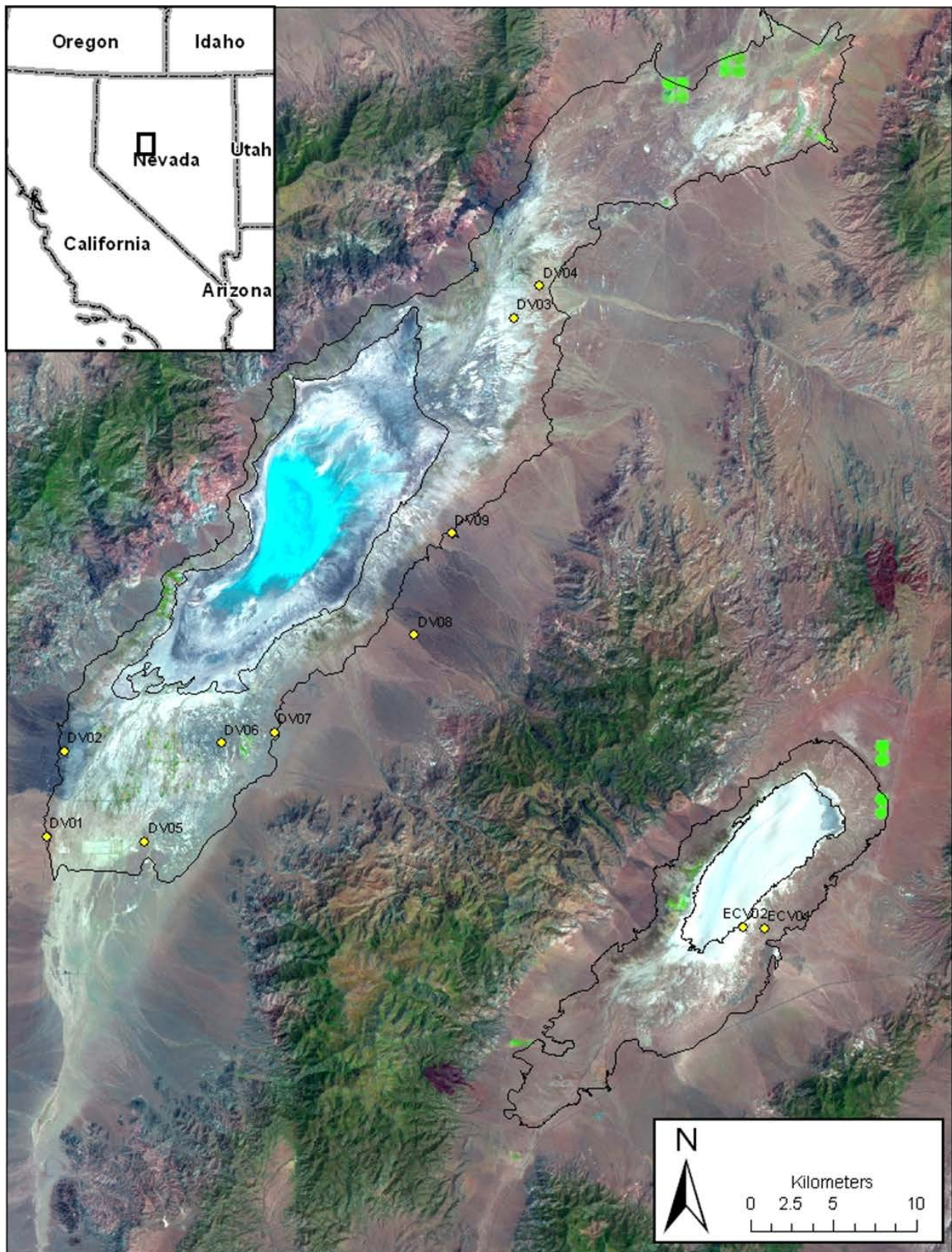


Figure 11. Locations at which soil background reflectance was measured in September 2012. Background image is the 7/31/10 TM scene (TM 5, 4, 3 = R, G, B).

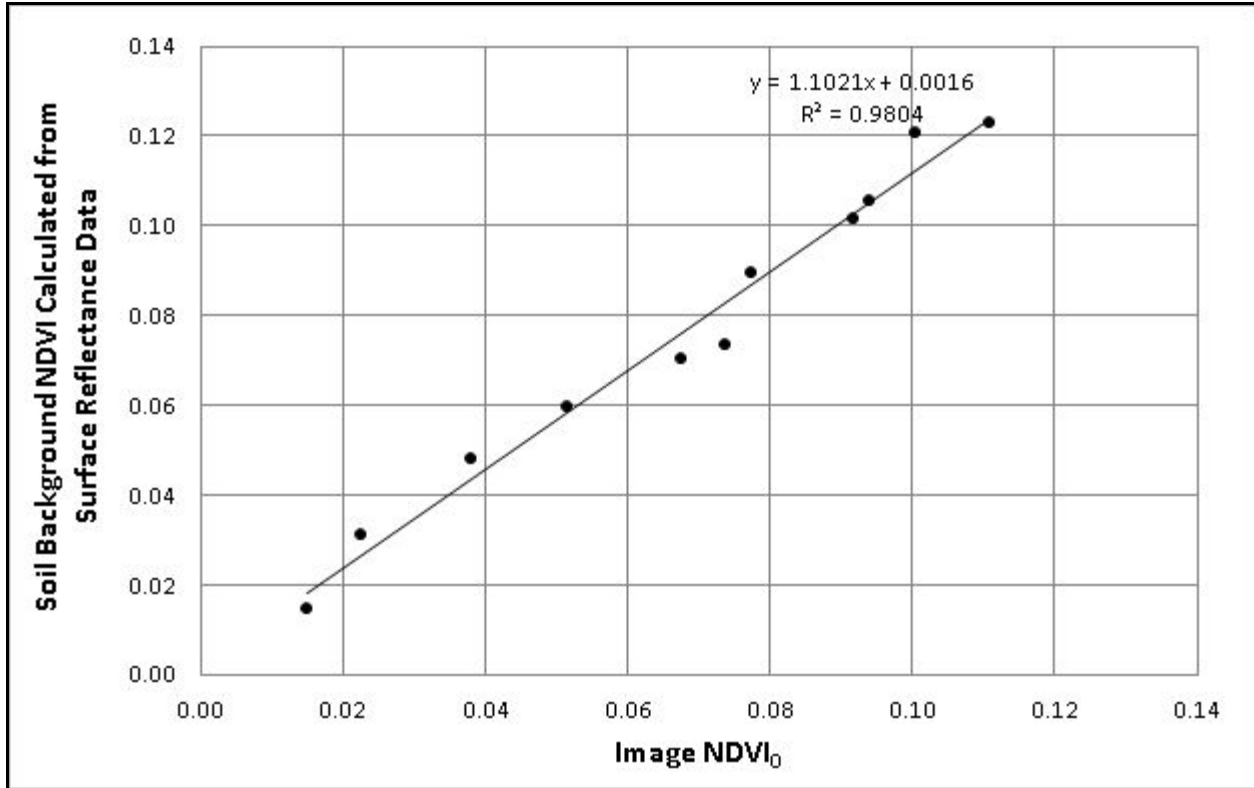


Figure 12. Comparison of surface-measured bare soil NDVI to NDVI₀ image values.

Figure 12 indicates a strong relationship between measured soil background NDVI and NDVI₀ image values, but the bias in the data is the opposite of what remnant leaves in a shrub canopy would produce. However, all vegetation canopies were purposely omitted from the surface reflectance data collected in September, 2012, so none of the spectra plotted in Figure 12 were acquired in conditions under which the potential problem could occur.

A comparison of ET_g estimates from NDVI* images to those estimated from eddy covariance data indicated that underestimation of ET_g in dense phreatophyte areas could be a significant issue. The USGS defined generalized circular areas surrounding each eddy covariance tower which estimated the source area for 45% and 90% of the water vapor flux measured at each station. The radii of the 45% and 90% contribution areas were 28.5 m and 214 m for the SV site, and 20.5 m and 150 m for the DV site (Garcia et al., 2014). NDVI*-derived ET_g estimates paired with the eddy covariance estimates were calculated as the average of two mean ET_g values: the mean of the image pixels falling within the 45% perimeter, and the pixels falling between the 45% to 90% perimeters. ET_g estimates for the SV site generated from NDVI* data differed from the 2010-2011 mean eddy covariance ET_g estimate (53 mm) by less than the reported probable error (21 mm) for all five years, but ET_g estimates for the DV site differed from the eddy covariance value (225 mm) by more than the reported probable error (50 mm) for all five years (Table 7). Although some of the difference in ET_g estimates at the

DV site might be explained by vegetation density variation in the vicinity of the DV site and the chosen shape and size of the fetch area over which NDVI* image data were averaged for comparison purposes (Figure 13), the differences were large enough to indicate that underestimation of NDVI* occurred in at least some dense phreatophyte stands.

Table 7. Comparison of Annual ET_g Estimates (mm) from NDVI* and USGS Eddy Covariance Stations at Sparse Vegetation (SV) and Dense Vegetation (DV) Sites

| Year | SV Eddy Covariance | | SV NDVI* | | DV Eddy Covariance | | DV NDVI* | |
|---------------|------------------------|------------------------------|--|--|------------------------|------------------------------|--|--|
| | Annual ET _g | Probable Error (1 σ) | ET _g w/o NDVI ₀ adjustment | ET _g after NDVI ₀ adjustment | Annual ET _g | Probable Error (1 σ) | ET _g w/o NDVI ₀ adjustment | ET _g after NDVI ₀ adjustment |
| 2007 | None | N.A. | 47.1 | 47.4 | None | N.A. | 101.0 | 123.4 |
| 2008 | None | N.A. | 43.3 | 43.6 | None | N.A. | 69.3 | 91.2 |
| 2009 | None | N.A. | 48.8 | 49.0 | None | N.A. | 91.7 | 111.9 |
| 2010 | 48 | 28 | 38.4 | 38.5 | 247 | 53 | 120.7 | 139.5 |
| 2011 | 58 | 31 | 34.3 | 35.5 | 203 | 59 | 84.2 | 105.6 |
| 2010–2011 Avg | 53 | 21 | 36.4 | 37.0 | 225 | 40 | 102.5 | 122.6 |

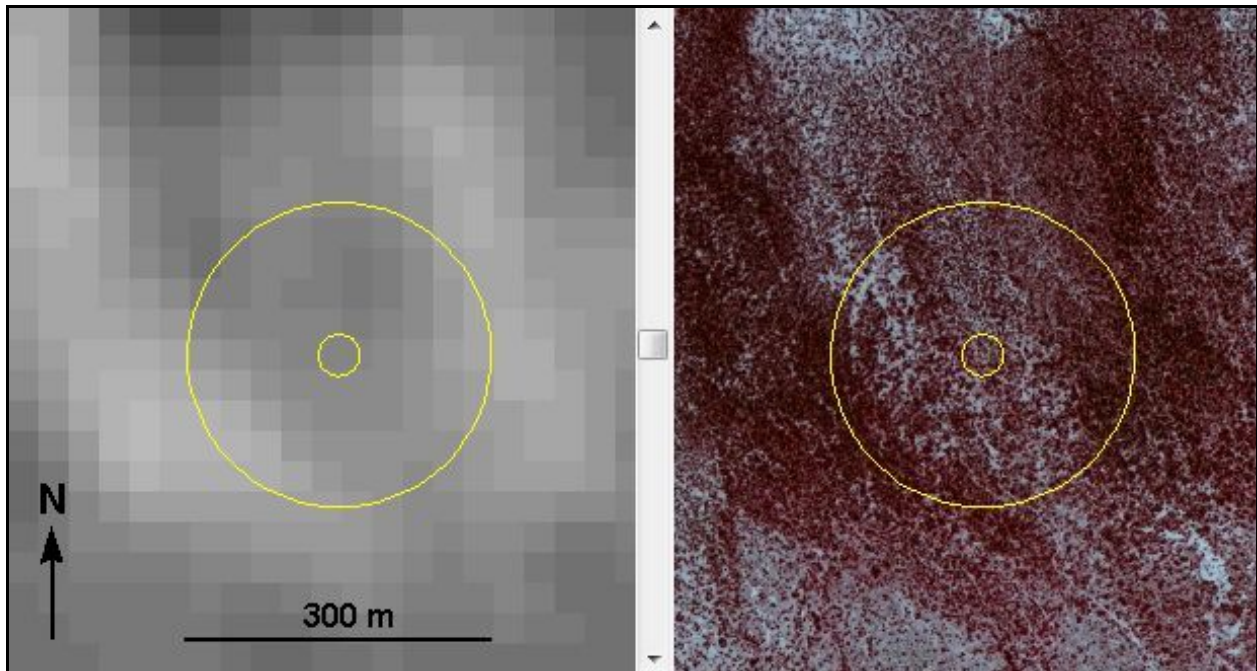


Figure 13. 7/31/10 NDVI (left) and 2010 color infrared NAIP images (right) showing two concentric circles identifying the calculated source areas for 45% (inner circle) and 90% (outer circle) of the water vapor flux measured at the DV station.

Reclamation chose to address this apparent problem by replacing $NDVI_0$ values in the densest phreatophyte stands with the average $NDVI_0$ values from nearby pixels in a manner similar to that used for spring-fed areas. A quantitative method was devised to map areas of dense phreatophytic vegetation that takes advantage of the general relationship between surface albedo and surface temperature. Assuming that solar radiation is the sole energy input to the system, minimal evaporation from the soil surface, and similar ground heat fluxes at all locations, areas with lower albedos that absorb more incoming solar radiation should exhibit higher surface temperatures than high albedo areas. Dense shrub canopies produce cooler surface temperatures because more heat is lost to the atmosphere over rough vegetation canopies, either through transpiration from phreatophyte leaves or through increased sensible heat flux from the aerodynamically rough vegetation canopy.

Temperature anomalies were identified with the aid of a linear relationship predicting brightness temperature from surface albedo. This relationship was defined using manually selected image data collected from areas throughout the Dixie Valley phreatophyte zone that supported little to no vegetation (Figure 14). The 8/8/07 TM image was used to define this relationship because 2007 had the lowest water year precipitation total of any year under study, and therefore the lowest probability of thermal anomalies resulting from either localized rainfall events before image acquisition or from dense stands of dead annual grasses that sprouted earlier in the year. Vegetation density was assessed using 2010 1-meter NAIP imagery, and the higher resolution imagery available using the “World Imagery” service available through ArcGIS online.

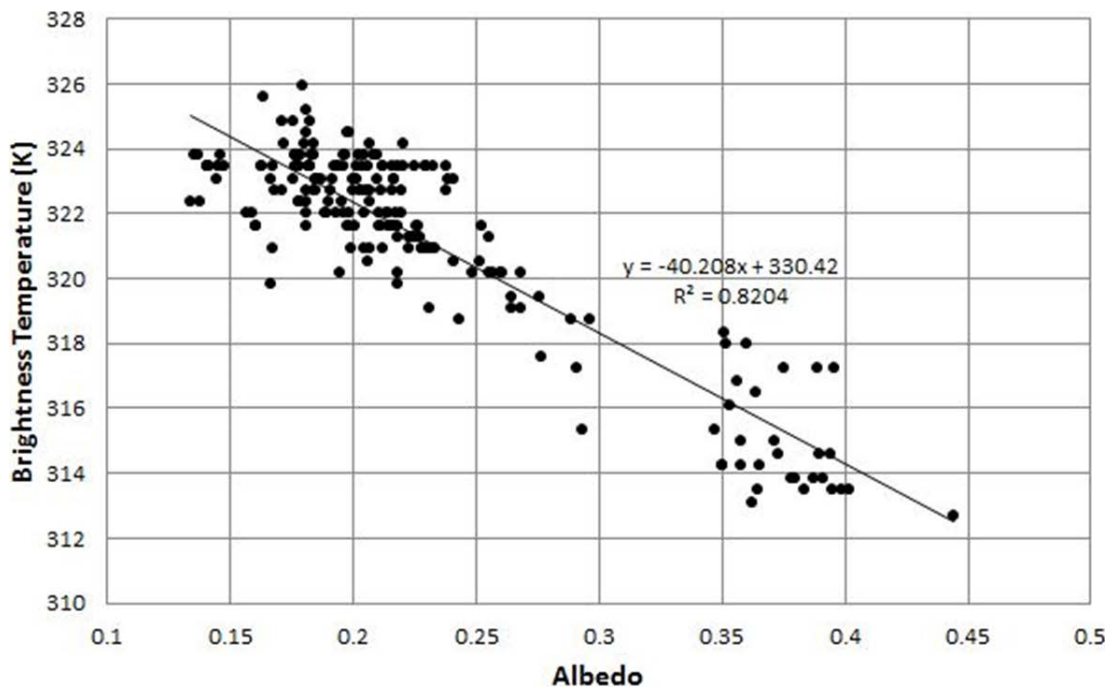


Figure 14. 8/8/07 brightness temperature vs. albedo for sparsely vegetated to unvegetated areas in the Dixie Valley phreatophyte zone.

A pixel was identified as a candidate to have its $NDVI_0$ value replaced by the average of its neighbors if its 8/8/07 brightness temperature was at least $7.5^{\circ}C$ cooler than the value predicted by its 8/8/07 albedo, using the regression equation shown in Figure 14. The identified pixels were manually edited to remove those within agricultural fields whose temperature anomaly resulted from moist soil, and a few whose identification resulted from the spatial resolution mismatch between the visible bands from which albedo is generated (30 m) and the thermal band providing temperature measurements (120 m). Figure 15 shows the dense shrub areas identified using the temperature anomaly method in red, with spring-fed and flowing well areas identified through manual image interpretation by the USGS and Reclamation in blue.

0.73 % and 1.95% of the pixels in the Dixie Valley and DVHA phreatophyte zones were identified for replacement as a result of this operation. Replacement of dense shrub $NDVI_0$ resulted in locally significant decreases in $NDVI_0$ values for some of the dense phreatophyte stands; but it produced only a minor 20 mm increase in ET_g at the DV site, from 103 mm to 123 mm (45.6% of measured DV ET_g to 54.5%) and a negligible increase at the SV site (Table 7). The overall effect on ET_g estimates was small due to the small affected area (852 acres in Dixie Valley, 3,272 acres total in the DVHA). Taken through the $NDVI^*$ calculations, this procedure increased ET_g by 162 acre feet in Dixie Valley and 475 AF in the DVHA (1.2% and 2.3% of the phreatophyte zone ET_g not attributed to agriculture, respectively).

Replacing Reduced Leaf-Off NDVI values from Salt-Covered Areas

For the vast majority of the Dixie Valley phreatophyte zone, the TM spectral reflectance values from the leaf-off image containing the lowest NDVI value were visually similar to those from summer images. The only exceptions were areas covering less than 3% of the study area which exhibited very high reflectance (in excess of 0.40 in the visible wavelengths) in some or all of the candidate leaf-off scenes, but significantly lower reflectance in the summer scenes. A USGS field crew visited several of these sites in April, 2011 and found these areas to be coated with a thin layer of salt (Figure 16).

The origins of this salt are not fully understood, but bright deposits typically appeared following cool season precipitation. The USGS hypothesized that it results from the evaporation of soil water during times of year when the evaporative demand of the atmosphere is low enough to allow precipitation to percolate into the salt-rich soils and absorb some of the salts before being gradually drawn back to the surface by capillary action to be evaporated, leaving the salts behind. The periodic appearance of these salt deposits is not thought to be an indicator of coincident groundwater evaporation because they do not occur in the summer, when capillary rise and evaporation of shallow groundwater would be the greatest. Whatever the cause, the salt crust produced nearly identical, high reflectance values in TM3 and TM4 which produced near-zero NDVI values that were significantly lower than those for the soil beneath the salt crust. And because the minimum NDVI value from the six candidate leaf-off scenes became

the $NDVI_0$ value, the salt-covered pixels needed to be replaced with values that were more representative of the summertime bare soil conditions.

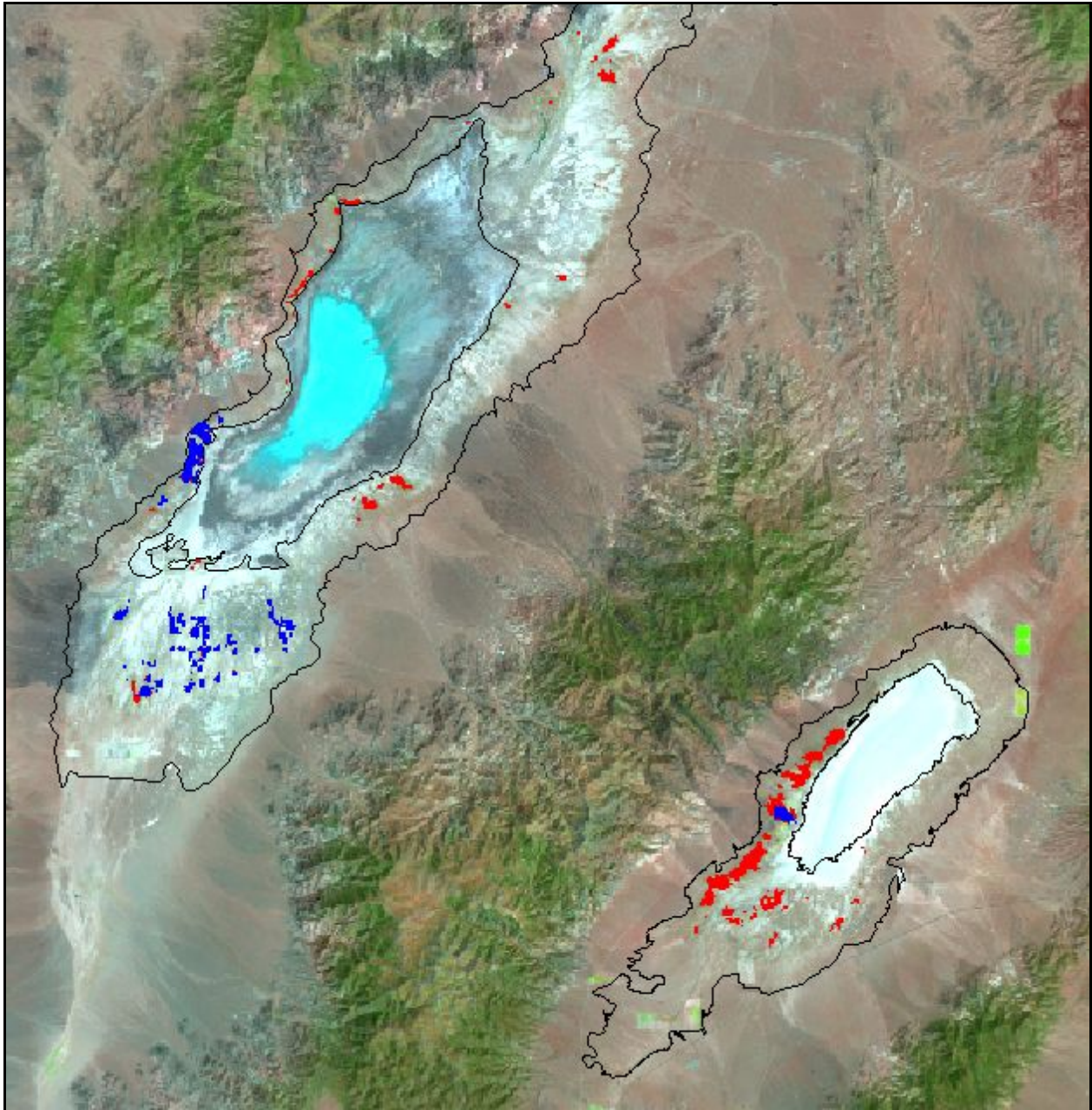


Figure 15. Dense phreatophyte areas in a portion of Dixie Valley and Edwards Creek Valley phreatophyte zones (outlined in black) identified using the temperature anomaly method (red), and spring-fed and flowing well areas identified by the USGS and Reclamation (blue) on the 8/8/07 TM image (TM 5, 4, 3 = R, G, B).



Figure 16. A salt-covered area northeast of the Dixie Valley playa (USGS photo taken on 4/19/11).

The procedure used to address this issue took advantage of the variability in salt coverage between candidate leaf-off scenes. A pixel that was salt covered on one scene was not necessarily salt-covered on all of the other five. An image mask of salt-covered areas was created from pixels whose TM1 reflectance value exceeded 0.42 on any of the six candidate leaf-off scenes. This threshold reflectance value appeared to be brighter than any surface not impacted by surface salt accumulation, and was five percent greater than the brightest reflectance value from a salt-free surface measured by Reclamation in the field (site ECV02 shown in Figure 11). Next, the lowest TM1 reflectance value from the six candidate leaf-off scenes for each pixel in the initial salt mask was identified, as well as the candidate leaf-off image from which it came. If a pixel's minimum leaf-off TM1 reflectance value was within 0.10 reflectance of its leaf-on TM1 reflectance value (defined as the minimum TM1 reflectance value from the 8/8/07, 7/28/09, and 7/31/10 images), the potential replacement pixel was assumed to be only minimally affected by salt crust, and its NDVI value became the new $NDVI_0$ estimate. This procedure produced new $NDVI_0$ estimates for 53% of the pixels identified in the initial mask of salt-covered areas. The values of these new $NDVI_0$ pixels were then averaged using a 7x7 low-pass filter, and

then expanded outward by 10 pixels using successive passes of 7x7, then 15x15-pixel low-pass filters to form an NDVI₀ replacement image. The resulting replacement image provided NDVI₀ estimates to all pixels identified in the initial salt-covered mask, while bordering pixels received a final NDVI₀ value that was the average of their original value and that from the NDVI₀ replacement image. This procedure resulted in a 0.0227 increase in NDVI₀ values for the 4539 acres identified as being salt-covered. Taken through the NDVI* calculations, this procedure reduced the ET_g estimate for the salt-covered areas by approximately 500 acre feet.

Generating NDVI* Images

NDVI* images were generated using Equation 2 by rescaling each pixel in the “leaf-on” NDVI images between the “leaf-off” NDVI₀ image value where NDVI* = 0, and the “saturated” NDVI (NDVI_S) value of 0.915 where NDVI* = 1.0. The 0.915 NDVI_S value was a common NDVI value occurring in center pivot agricultural fields within the TM images containing Dixie Valley.

A small fraction of the pixels in each NDVI* image had negative values where leaf-off NDVI values were slightly greater than leaf-on NDVI values. Possible causes for this condition include errors in reflectance calibration and differences in soil background condition between leaf-off and leaf-on scenes. But including these negative NDVI* values in computations of ET_g instead of clipping them to zero prior to computations resulted in only minor decreases in the estimated DVHA phreatophyte zone ET_g. The 7/25/08 NDVI* image contained the largest percentage of negative NDVI* values (5.1%), but including these negative values in the phreatophyte zone ET_g computations instead of clipping them at zero resulted in an ET_g decrease of only 0.84%. During the calculation of the final ET_g estimates from this study, all negative NDVI* values were set to zero.

The Effect of Non-Phreatophytic Vegetation

Although Equations 3 and 4 compensate to some degree for variation in phreatophyte NDVI response resulting from variable evaporative demand and precipitation from year to year, one of the preconditions inherent to the NDVI* procedure is that all of green-leaf vegetation generating the NDVI* signal (i.e., the NDVI response exceeding the NDVI₀ value) is associated with phreatophytic vegetation. This condition was impossible to meet for all of the DVHA basins using imagery from a single year. Boundaries of the phreatophyte zones within the DVHA were delineated to include the entire range occupied by phreatophytes in each valley, and phreatophyte densities within the defined phreatophyte zones ranged from dense to very sparse. Field crews observed non-phreatophytic grasses, forbs, and shrubs interspersed with phreatophytes at many locations within the mapped phreatophyte zones, particularly near their upslope margins. During June of 2010, the USGS measured vegetation canopy cover using transect

analysis at 21 locations in the Dixie Valley phreatophyte zone, and 14 of these locations contained non-phreatophytic shrub vegetation (Garcia et al., 2014). The summertime NDVI response of soil and vegetation can change as a result of precipitation.

Biological soil crust responds quickly to summer rains, producing brief periods of elevated NDVI* values immediately after wetting. Vegetation of all types can respond to significant precipitation events in the spring and early summer, and such events can prolong the period of leaf retention for non-phreatophytic shrubs, producing elevated NDVI values. And dead, dry herbaceous vegetation such as cheat grass that grew in response to favorable conditions earlier in the year can produce NDVI values greater than the underlying soil. The spectral library maintained by the U.S. Geological Survey's Spectroscopy Laboratory in Denver, Colorado (<http://speclab.cr.usgs.gov/spectral.lib06/ds231/datatable.html>) contains a reflectance spectrum for 'mature brown cheatgrass' which produces an NDVI value of 0.18—about 50% greater than the highest soil NDVI value measured in the field (Figure 12). Including the NDVI signal from any such non-phreatophytic vegetation in the calculation of ET_g violates the preconditions of the NDVI* method and produces inflated estimates of ET_g.

An obvious example of the effect of non-phreatophytic vegetation on phreatophyte zone NDVI* values can be seen in the Edwards Creek Valley area, east of Dixie Valley. Figure 17 shows the northern and eastern boundaries of the Edwards Creek Valley phreatophyte zone on NDVI* images from 2007 through 2011, as well as the 7/28/09 TM image (TM bands 5, 4, 3 = red, green, blue) provided for geographic reference. NDVI* values to the east and north of the phreatophyte zone in 2007 are at expected low levels. But the 2008–2011 images show several instances where elevated NDVI* values exist both upslope of and within the phreatophyte zone. NAIP imagery and high-resolution ArcGIS World Imagery of areas in Figure 17 exhibiting the highest NDVI* values in 2008, 2009, and 2011 showed only widely scattered shrub vegetation, indicating that herbaceous vegetation was the most likely cause for the elevated NDVI* values seen during those years. In September, 2012, a field crew verified the presence of dry herbaceous cover in areas exhibiting elevated 7/28/09 NDVI* both within and upslope of the Edwards Creek Valley phreatophyte zone (Figure 18).

Any elevated NDVI* values found in the valley floors but above the phreatophyte zones must result from meteoric water or runoff from adjacent mountains, as there is no other source of moisture. Given that non-phreatophytic vegetation exists both above and below the phreatophyte zone boundary, it is reasonable to assume that when NDVI* values above the phreatophyte zone are high, a significant portion of the composite NDVI* signal within the phreatophyte zone comes from non-phreatophytic vegetation. Strengthening this argument is the fact that the vegetative response of phreatophytes should not vary significantly from one year to the next. The fact that 2009 NDVI* values inside the eastern boundary of the Edwards Creek Valley phreatophyte zone (Figure 18) were up to 5 times the 2010

values (exceeding 0.20 in some places) is clear evidence of the influence of non-phreatophytic vegetation on the phreatophyte zone NDVI* response. Therefore, ET_g estimated from images with elevated NDVI* values above the phreatophyte zone most likely will be too high, as a portion of NDVI* signal used to calculate ET_g originates from non-phreatophytic vegetation.

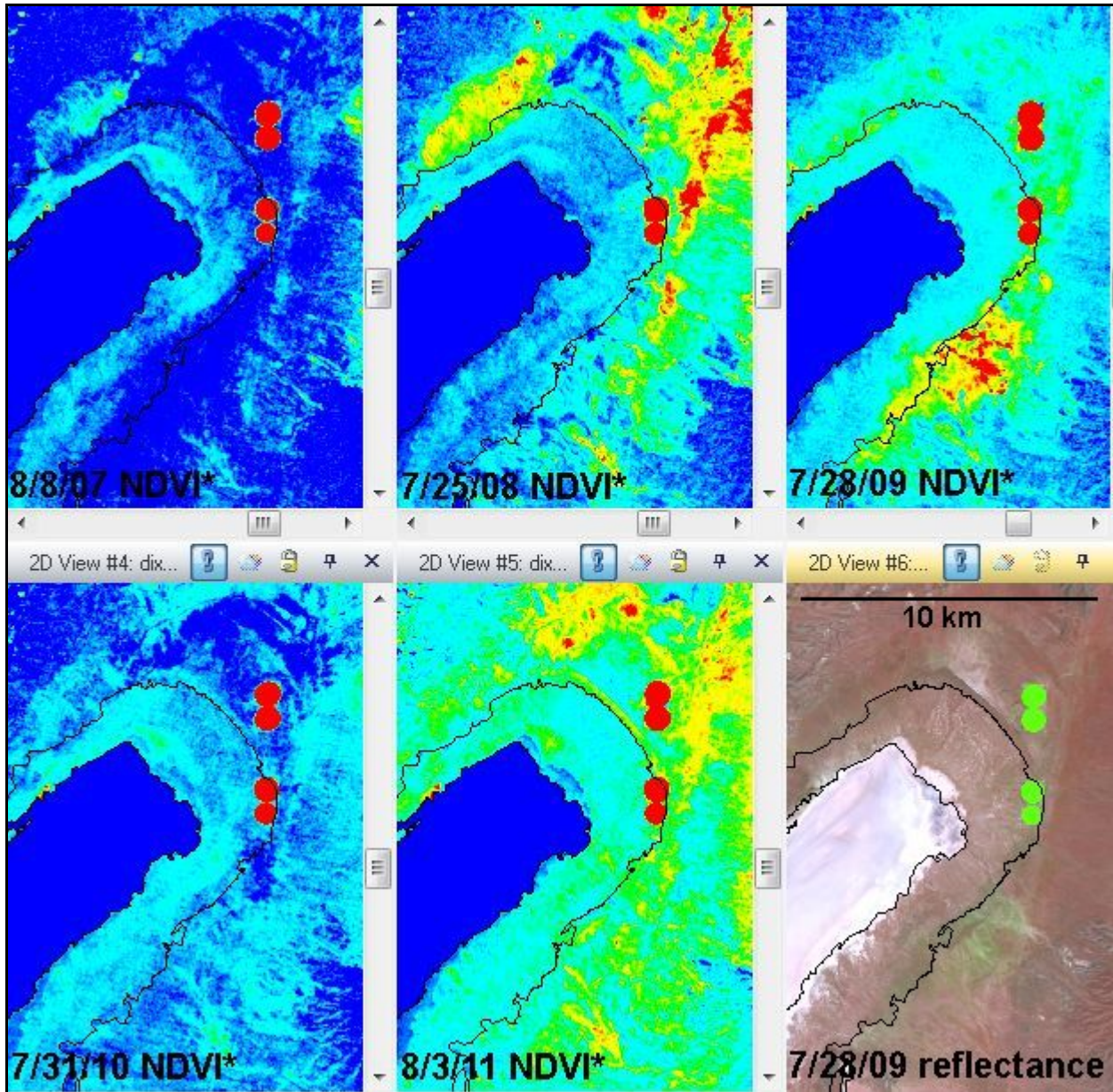


Figure 17. NDVI* images of the Edwards Creek Valley area showing the impact of non-phreatophytic vegetation on NDVI* values within the phreatophyte zone. Color coding for NDVI* images stretches between blue (NDVI* = 0) to red (NDVI* = 0.20). 7/28/09 surface reflectance image shows TM bands 5, 4, 3 as R,G,B.

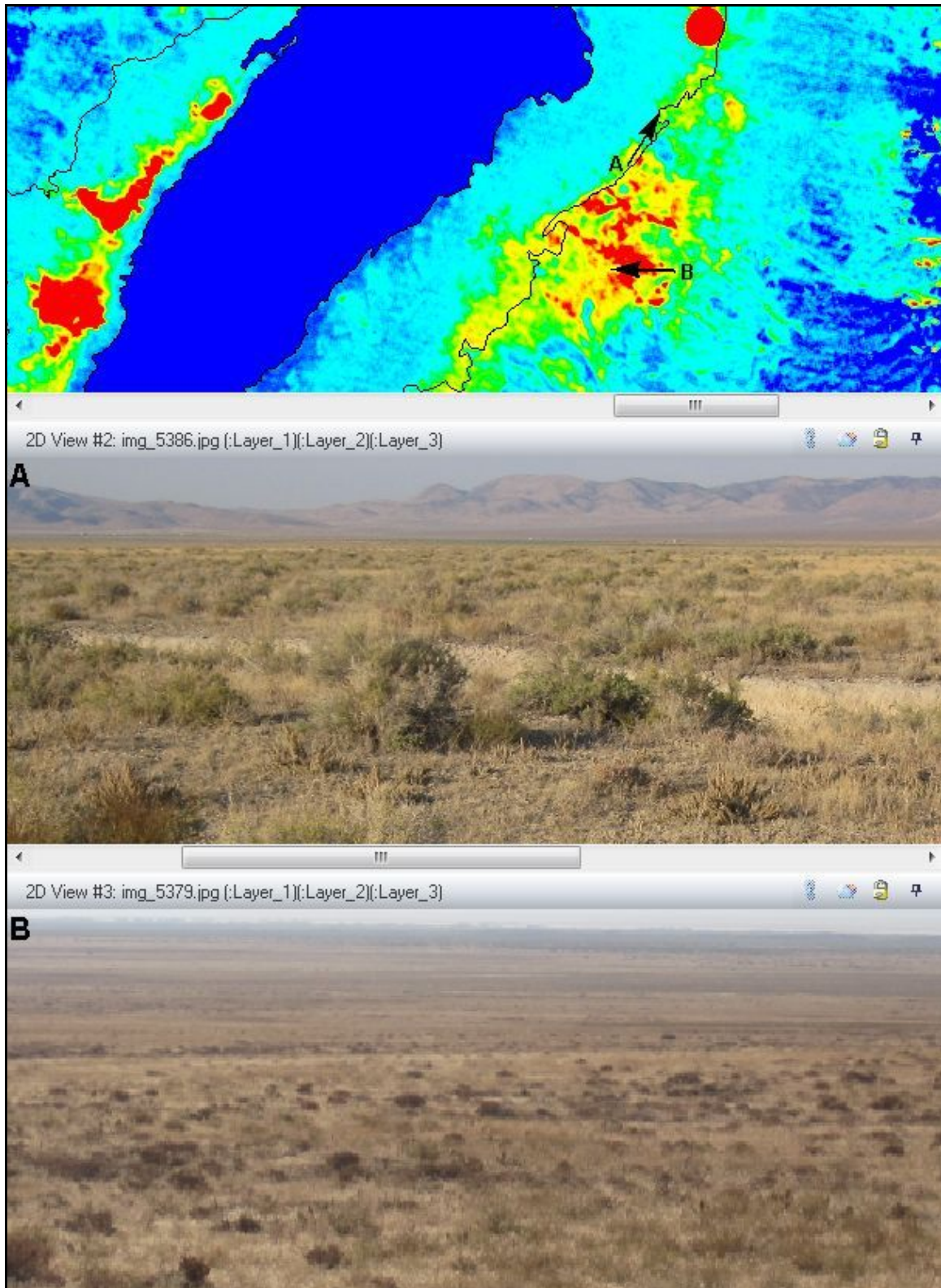


Figure 18. Field photos showing herbaceous vegetation existing within (A) and above (B) the Edwards Creek Valley phreatophyte zone, referenced to 7/28/09 NDVI* image (color coding stretches between blue (NDVI* = 0) to red (NDVI* = 0.20). Photos were taken at the base of the arrows shown on the NDVI* image, in the direction indicated by the arrows.

NDVI* images of the DVHA are presented in Figure 19. Although the scale of the images displayed in Figure 19 is small, close inspection shows that no one year produced the “ideal” result of clear demarcation of all phreatophyte zones. However, Figure 19 does show that the NDVI* images from 2007-2009 produced a cleaner demarcation of the Dixie Valley phreatophyte zone than those from 2010 and 2011.

Correlation with Phreatophyte Canopy Cover Data

Other than the visual trends shown in Figure 19, only limited ground reference data were available that could be considered useful in determining the optimum NDVI* image or images to use. The two USGS eddy covariance towers within the Dixie Valley phreatophyte zone provided valuable data, but the DV site was located in an area of significant spatial heterogeneity, making the selection of the appropriate NDVI* value to pair with the DV ET_g estimate problematic. To obtain a less ambiguous indication of the correlation of specific NDVI* images with phreatophyte ET, NDVI* values were compared to the phreatophyte canopy cover estimates generated by the USGS—a variable assumed to be correlated with phreatophyte ET_g. Of the 21 sites at which phreatophytic shrub canopy cover (PSCC) was measured within Dixie Valley, one was unsuitable for comparison with Landsat NDVI* values and because it was located in a transition zone between sparsely and densely vegetated areas where there was some uncertainty as to whether the 3x3-averaged image data would accurately represent the field-measured condition. Two of the remaining 20 sites (Figure 20) were located adjacent to the SV and DV eddy covariance stations, where phreatophyte canopy cover was measured along two 200-meter transects arranged in a “+” configuration in the cardinal directions. For the other 18 transects, phreatophyte canopy cover was measured along two 100-meter transects similarly arranged. Canopy cover was calculated as the proportion of transect length intersecting a phreatophyte canopy to total transect length. NDVI* image data were extracted at the pixel containing the transect center point for the 18 sites whose PSCC was measured using 100-meter transects. For the other two sites, NDVI* image data were extracted along 7- pixel by 7-pixel “+” patterns centered on the pixel containing the transect center point, then averaged.

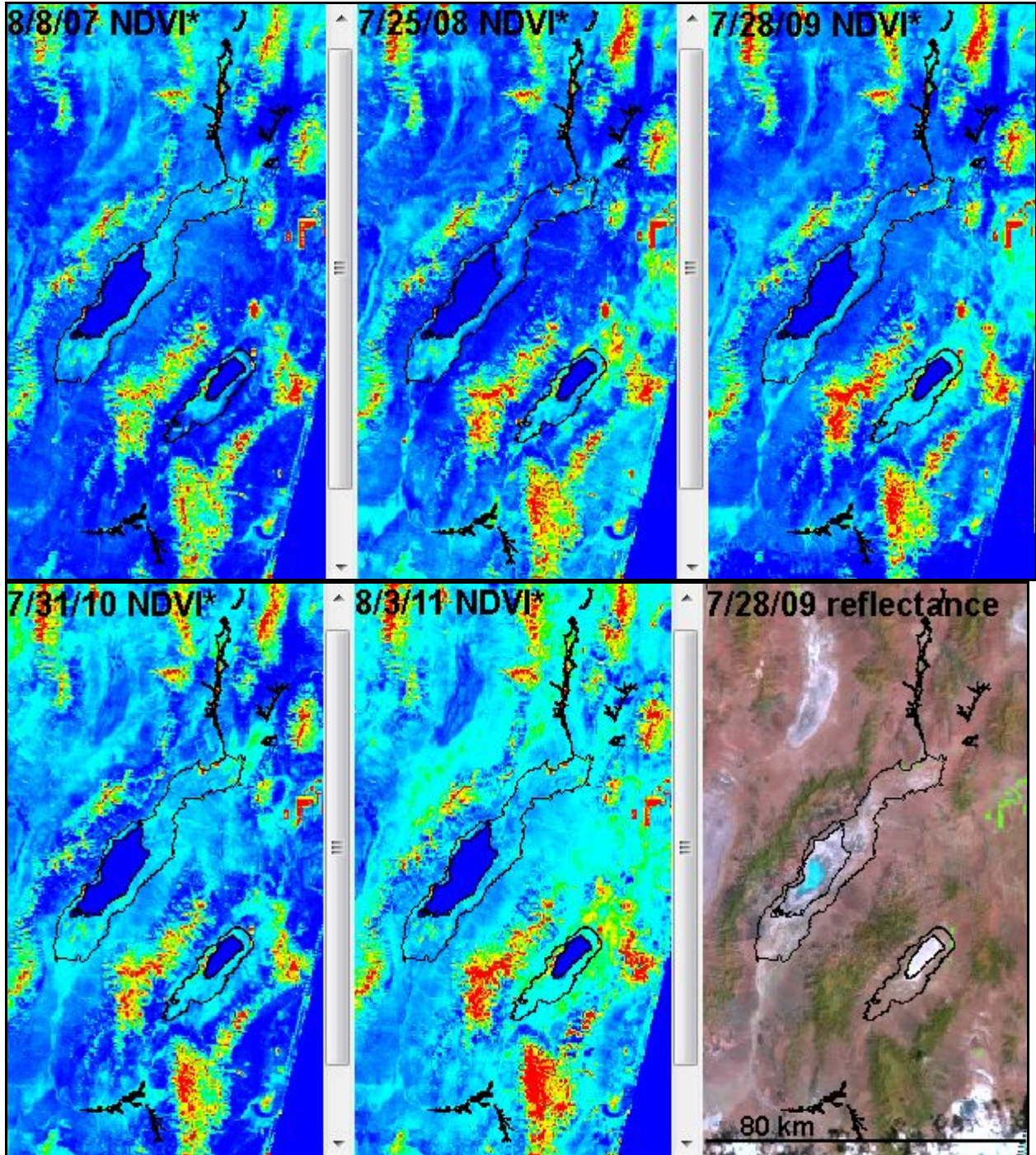


Figure 19. Color-coded NDVI* images from 2007–2011 and the 7/28/09 surface reflectance image (TM bands 5, 4, 3 = R,G,B) as spatial reference. Color coding is on a continuous scale, with dark blue indicating near zero NDVI*, and red indicating NDVI* ≥ 0.20 .

Estimating Groundwater Discharge from
Phreatophyte Transpiration in Dixie Valley, Nevada

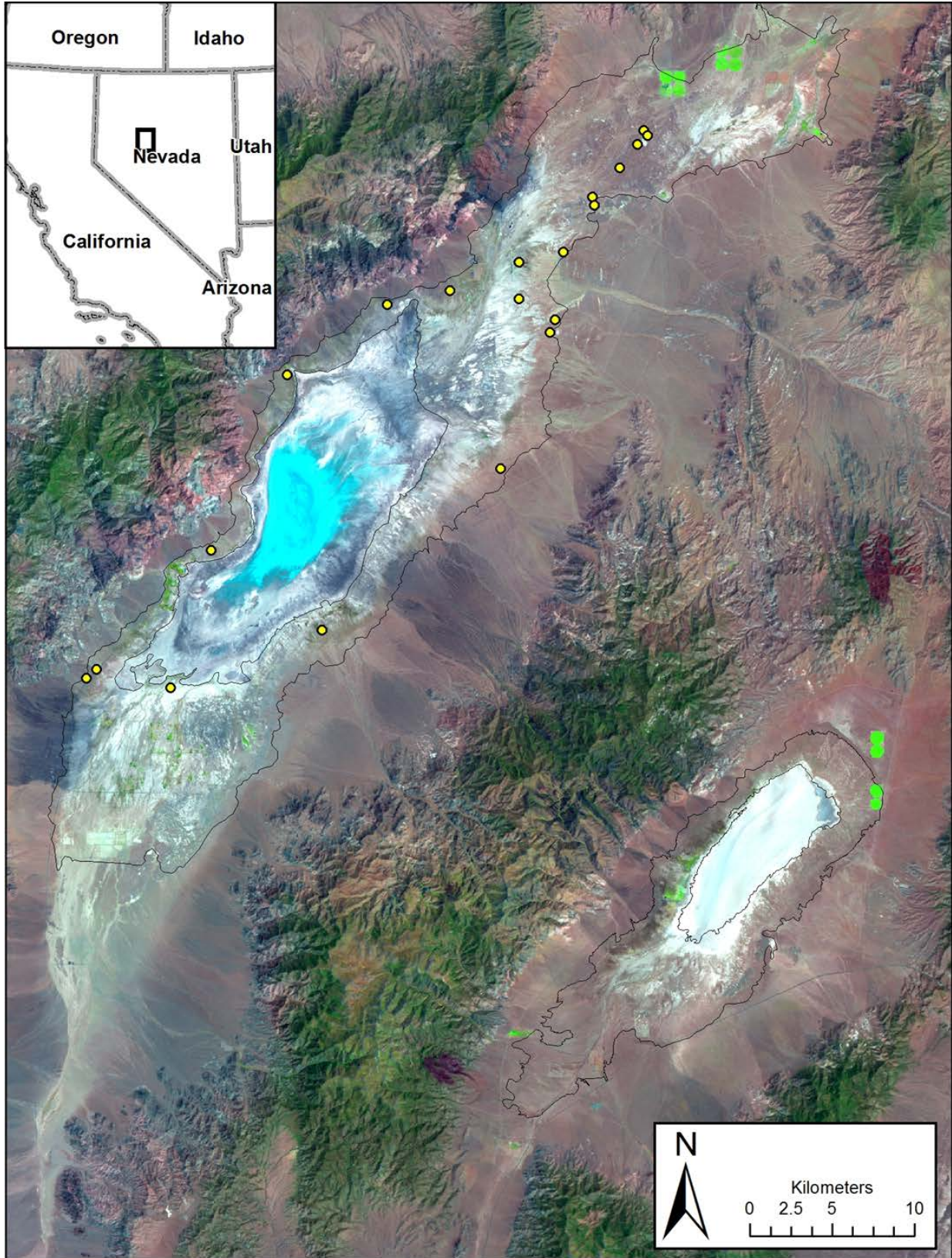


Figure 20. Locations of 20 sites at which phreatophytic shrub canopy cover was measured in 2010. Background image is the 7/31/10 TM scene (TM 5, 4, 3 = R, G, B).

Figure 21 shows the relationship between PSCC and NDVI* for the 2007–2011 mid-summer images. The regression models were derived from a small sample size of 20 and the calculated slope and intercept values are only estimates of the populations' true values, but analyzing them in combination with the NDVI* images in Figure 19 is instructive. The 7/28/09 regression model produces the best r^2 value (0.937), and a near-zero intercept value. The near-zero intercept value indicates that NDVI* values at the low end of the distribution are not likely to systematically underestimate or overestimate ETg from phreatophytes, as zero NDVI* predicts near zero PSCC (and presumably near zero transpiration of groundwater by phreatophytic shrubs). The 7/28/09 NDVI* image in Figure 19 affirms this interpretation as it shows a fairly clean boundary around all but the southern boundary of the Dixie Valley phreatophyte zone (where no measurement plots were located). The unambiguous phreatophyte zone boundary indicates that the majority of the NDVI* signal is coming from phreatophytes, not xerophytes or herbaceous vegetation in the phreatophyte zone. The correlation between 7/25/08 NDVI* and PSCC also is quite high (0.914); but the positive intercept indicates a slight negative bias to the NDVI* estimates of ETg, as an NDVI* value of zero (which produces an ETg estimate of 0 mm) produces a PSCC estimate of 2.53%. This effect manifests in Figure 19 where the phreatophyte zone boundary east and west of the Dixie Valley playa area is the most distinct of any of the NDVI* images. However, some areas within the phreatophyte zone have little to no estimated ETg, indicating a possible underestimation of ETg values. The correlation between NDVI* and PSCC is not nearly as strong with the 8/8/07 image ($r^2 = 0.858$), but a near-zero intercept produces another reasonable phreatophyte zone boundary visible on the NDVI* in Figure 19. The 7/31/10 and 8/3/11 datasets have the lowest r^2 values (0.828 and 0.808, respectively), and their negative intercept values indicate the influence of non-phreatophytic vegetation, as a nonzero NDVI* value is associated with zero PSCC. Figure 19 corroborates this interpretation, as significant NDVI* values appear upslope of the phreatophyte zones.

Generating ETg Images

ETg images were generated from each of the five midsummer NDVI* images using Equation 4. Any negative ETg estimates were rescaled to zero. Agricultural crops were treated differently than natural vegetation. Agricultural fields that exhibited NDVI values in excess of 0.75, or were active center pivot fields were assigned an ETg value equal to 1.1 times the net irrigation requirement estimated by the Nevada Division of Water Resources for Dixie Valley (1219 mm; http://water.nv.gov/mapping/et/et_general.cfm; Huntington and Allen, 2010). ETg for other agricultural lands were estimated using the NDVI* method, but their ETg values were not allowed to exceed 1219 mm.

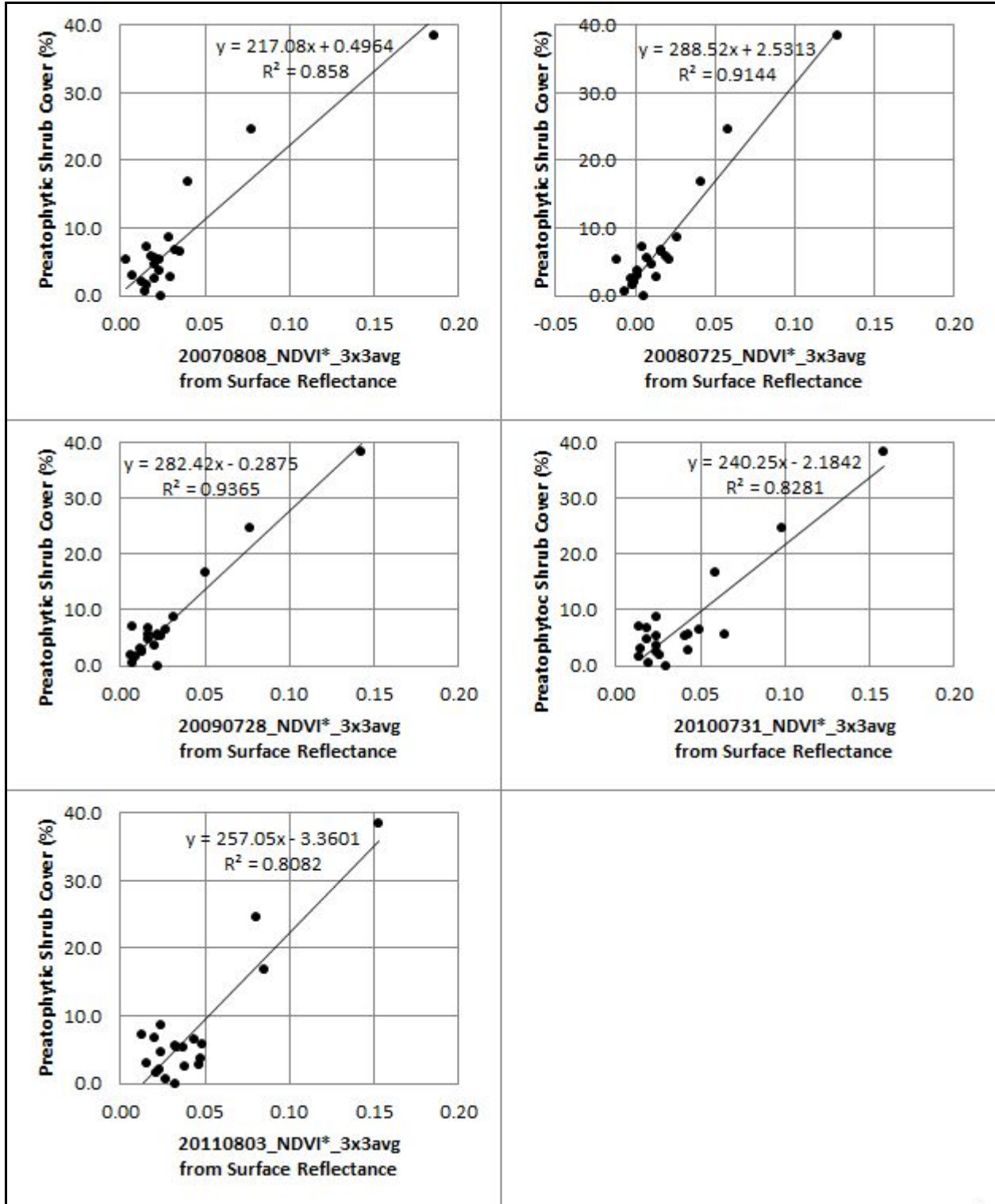


Figure 21. Scatterplots showing the relationships between phreatophytic shrub canopy cover measured in June 2010 with NDVI* values from 2007–2011. The linear least-squares model predicting phreatophytic shrub canopy cover from NDVI* is shown on each plot.

Final Estimates of ET_g

Of all five years for which NDVI* images were generated, the 7/28/09 image produced the best fit between NDVI* and percent phreatophytic shrub canopy cover ($r^2 = 0.937$), and the intercept value closest to zero (-0.288). It also produced an unambiguous phreatophyte zone boundary in most locations within Dixie Valley. However, as with the NDVI images used to characterize the leaf-off NDVI condition, environmental variability in the study area produced a situation where no single year produced optimal results across the DVHA. The 7/28/09 NDVI* image clearly was not the best choice for the southern portion of the Dixie Valley phreatophyte zone, or for the Edwards Creek Valley phreatophyte zone. In these locations, elevated NDVI* values existed on upland areas immediately adjacent to the phreatophyte zones, indicating a contribution to the phreatophyte zone NDVI* signal from non-phreatophytic vegetation and/or photosynthetically active biological soil crust.

Combining Multiple Years of ET_g Estimates

Two different processing approaches were investigated as a solution to the problem of environmental variability across the DVHA: pixel-by-pixel averaging of ET_g estimates from multiple dates, and pixel-by-pixel selection of ET_g estimates from the 2007-2011 date range according to their rank order. These approaches are described below.

Multidate Averaging

Using NDVI* images for a single year to characterize ET_g was deemed suspect, out of concerns that the specific environmental conditions for the selected year and/or any systematic errors associated with image calibration could yield results not indicative of the long-term mean. A multidate averaging approach was seen as a way to better characterize typical conditions. However, analysis of spatial patterns in the NDVI* imagery in Figure 19 and the scatter plots in Figure 21 showed that non-phreatophytic vegetation produced elevated NDVI* values at nearly all locations within the DVHA on two of the five midsummer NDVI* images. Achieving the beneficial aspects of averaging multiple years of ET_g estimates while minimizing the influence of non-phreatophytic vegetation on those estimates was accomplished by generating new ET_g images that contained the average of the lowest two and lowest three ET_g estimates for each individual pixel. These images are referred to as the “low2avg” and “low3avg” images.

Multidate Minimum

Another processing method intended to characterize typical ET_g conditions followed a procedure similar to that used in the generation of the NDVI₀ image. Each pixel's final ET_g value was to be the minimum of those generated for that pixel for each of the five years. However, the 7/25/08 NDVI* image appeared to have a slight negative bias in Dixie Valley, and including it in this calculation might bias results downward. This issue was addressed by assigning each pixel

the second lowest rather than the lowest ET_g estimate from the 5-year period. This image is referred to as the “2ndlowest” image.

Obtaining the Optimal ET_g Estimate

The NDVI* images generated from the hybrid approaches are displayed in Figure 22, and the scatterplots showing correlation with PSCC are shown in Figure 23. There is little degradation in the r^2 values shown in Figure 23 compared to those in Figure 21, with values of at least 0.907 for all hybrid approaches. Intercept values are also quite low with both the low3avg and 2ndlowest values being approximately 0.3 % PSCC. The spatial definition of all phreatophyte zones is also better on the hybrid NDVI* images than it is on any of the NDVI* images for individual years. Figure 24 shows the relationship between phreatophyte canopy cover and ET_g, estimated using the three hybrid approaches. Patterns are symmetrical about the regression line to those in figure 23, with the only differences between NDVI* and ET_g arising from the varying ETo and precipitation values from year to year.

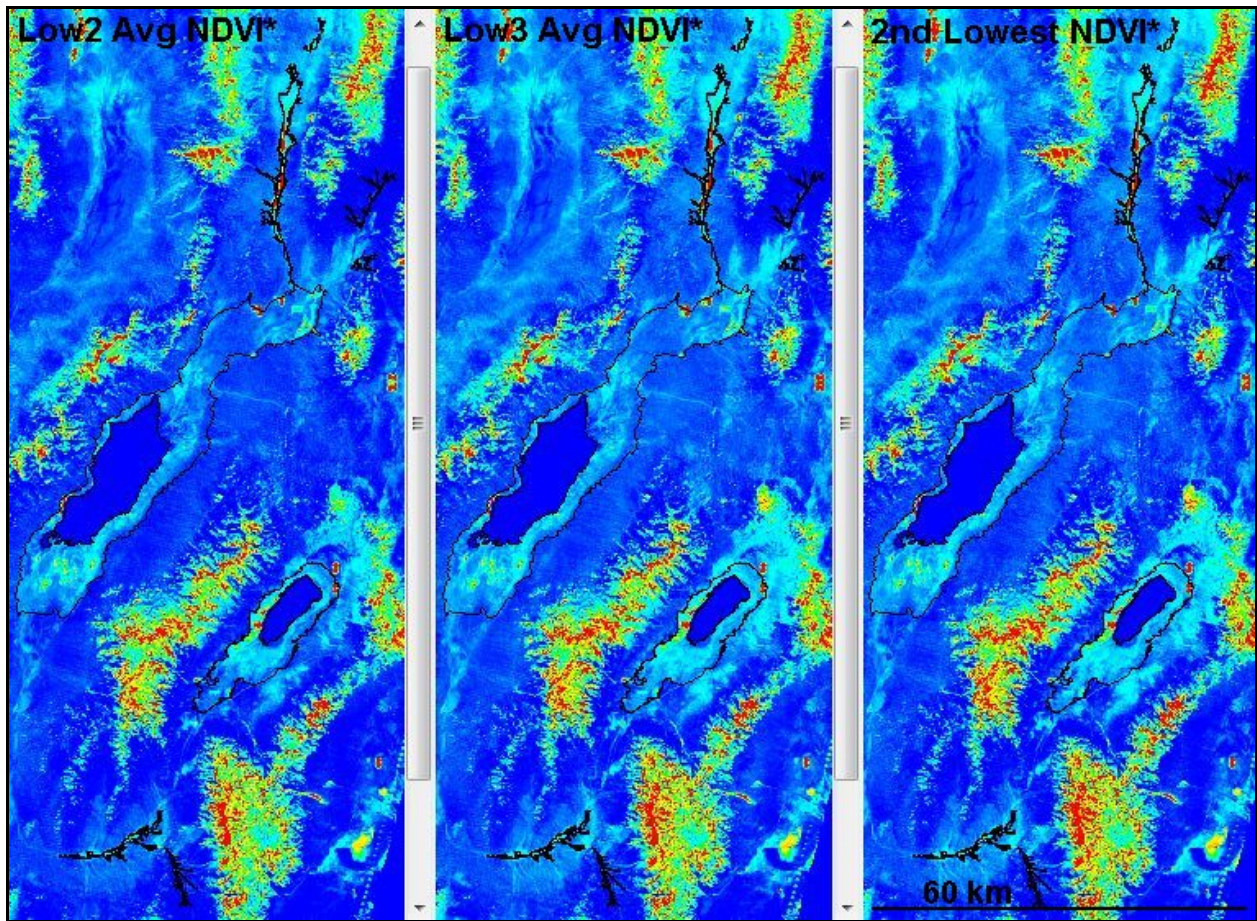


Figure 22. NDVI* images generated using the three hybrid methods: the average of the lowest two NDVI* values (left), the average of the lowest three (center), and the second lowest (right). Color coding is on a continuous scale, with dark blue indicating near zero NDVI*, and red indicating NDVI* \geq 0.20.

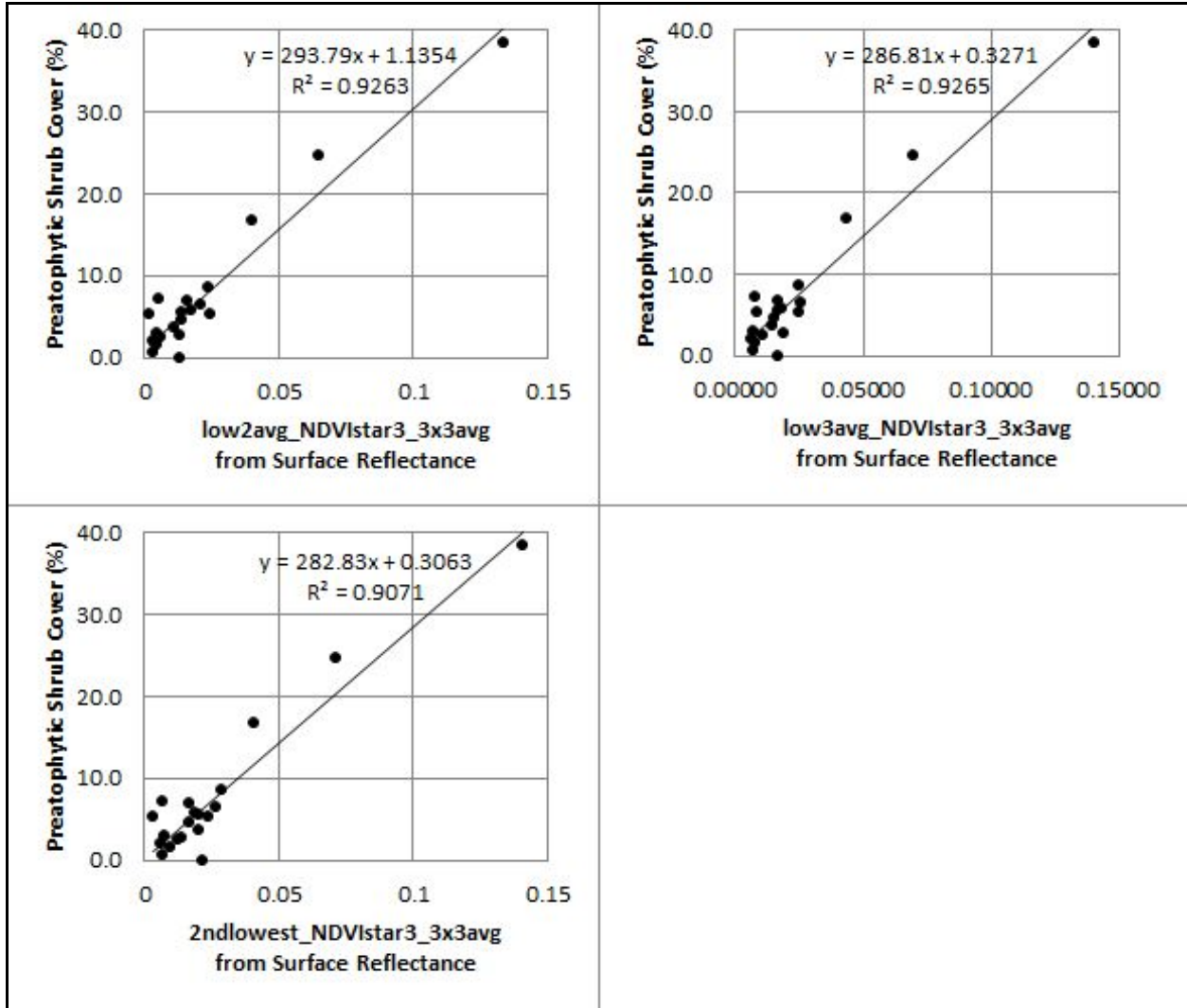


Figure 23. Scatterplots showing the relationships between phreatophytic shrub canopy cover measured in June 2010 with hybrid NDVI* values. The linear least-squares regression model predicting phreatophytic shrub canopy cover from NDVI* is shown on each plot.

ETg estimates derived from each of the five individual years and the three combination methods just described are presented in Table 8. For each DVHA basin, two sets of ETg estimates are provided: one combining the ETg from agriculture supported by groundwater pumping with that from desert phreatophytes and spring-fed vegetation, and one from desert phreatophytes and spring-fed vegetation only. Because the total area and location of irrigated agriculture varied from year to year, the hybrid approaches derived from multiple years of ETg data produced erroneous estimates of agricultural ETg that were not representative of any particular year. To avoid this situation, 2011 agricultural ETg estimates were substituted for all three hybrid approaches. Any land in agricultural production between 2007 and 2011 was excluded from the phreatophyte-only ETg estimates for all years. Phreatophyte-only ETg depths are

provided in addition to ET_g volumes to facilitate comparisons. Commonly used English units are reported in Table 8.

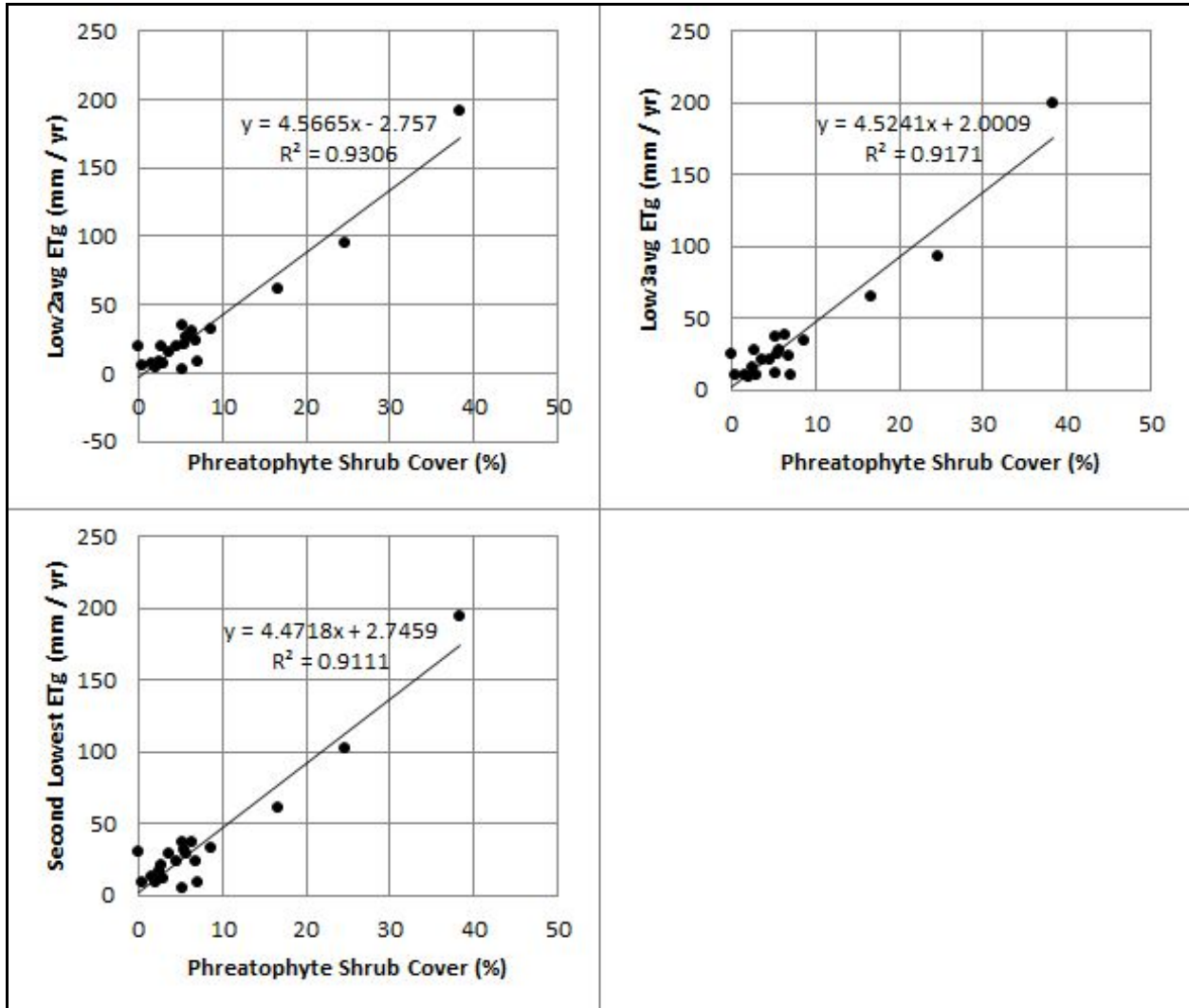


Figure 24. Scatterplots showing the relationships between phreatophytic shrub canopy cover measured in June 2010 and ET_g values estimated using the three hybrid approaches. The linear least squares regression model predicting ET_g from phreatophytic shrub canopy cover is shown on each plot.

Inspection of Table 8 shows that the ET_g estimates from the low3avg and 2ndlowest hybrid approaches are very similar to one another. They fall between the lowest and second lowest annual ET_g estimates for the DVHA as a whole and for all of its individual basins, except for the small Jersey Valley where the hybrid approaches produce the lowest estimate. The low2avg ET_g image produces the smallest ET_g estimate of any of the composite images, producing the smallest ET_g estimate for the entire DVHA, as well as for Dixie and Jersey Valleys.

Table 8. ETg Estimates by DVHA Basin in Acre Feet and Inches

'no ag' AF totals exclude ETg from all agricultural lands, without replacement with estimates of pre-development ETg.

| Estimate | Parameter | Stingaree | Cowkick | Eastgate | Dixie | Pleasant | Jersey | Edwards Creek | DVHA Total |
|----------------------|---------------------------------------|-----------|---------|----------|---------|----------|--------|---------------|------------|
| All | Phreatophyte zone area, no ag (acres) | 52.7 | 272.9 | 3,217 | 115,665 | 6,758 | 1,382 | 36,862 | 164,210 |
| 8/8/07 | PZ veg & ag (AF) | 5.5 | 31.6 | 363 | 21,111 | 4,862 | 136 | 6,582 | 33,091 |
| | PZ veg, no ag (AF) | 5.5 | 31.6 | 363 | 18,870 | 2,093 | 136 | 4,380 | 25,879 |
| | PZ veg, no ag (in) | 1.25 | 1.39 | 1.35 | 1.96 | 3.72 | 1.18 | 1.43 | 1.89 |
| 7/25/08 | PZ veg & ag (AF) | 10.4 | 76.8 | 892 | 17,285 | 4,741 | 93.0 | 8,327 | 31,424 |
| | PZ veg, no ag (AF) | 10.4 | 76.8 | 892 | 13,666 | 1,826 | 93.0 | 6,207 | 22,772 |
| | PZ veg, no ag (in) | 2.36 | 3.38 | 3.33 | 1.42 | 3.24 | 0.81 | 2.02 | 1.66 |
| 7/28/09 | PZ veg & ag (AF) | 7.3 | 83.3 | 605 | 18,888 | 4,230 | 97.2 | 9,264 | 33,174 |
| | PZ veg, no ag (AF) | 7.3 | 83.3 | 605 | 14,840 | 1,558 | 97.2 | 7,262 | 24,453 |
| | PZ veg, no ag (in) | 1.65 | 3.66 | 2.26 | 1.54 | 2.77 | 0.84 | 2.36 | 1.79 |
| 7/31/10 | PZ veg & ag (AF) | 8.2 | 72.0 | 758 | 24,278 | 4,597 | 197 | 8,385 | 38,294 |
| | PZ veg, no ag (AF) | 8.2 | 72.0 | 758 | 20,236 | 1,919 | 197 | 6,404 | 29,593 |
| | PZ veg, no ag (in) | 1.87 | 3.17 | 2.83 | 2.10 | 3.41 | 1.71 | 2.08 | 2.16 |
| 8/3/11 | PZ veg & ag (AF) | 9.7 | 58.4 | 822 | 22,213 | 5,184 | 290 | 11,619 | 40,197 |
| | PZ veg, no ag (AF) | 9.7 | 58.4 | 822 | 18,200 | 2,587 | 290 | 9,631 | 31,598 |
| | PZ veg, no ag (in) | 2.21 | 2.57 | 3.07 | 1.89 | 4.59 | 2.51 | 3.14 | 2.31 |
| Mean of Low 2 | PZ veg & ag (AF) | 6.1 | 41.9 | 452 | 16,294 | 4,177 | 71.1 | 6,609 | 27,650 |
| | PZ veg, no ag (AF) | 6.1 | 41.9 | 452 | 12,281 | 1,579 | 71.1 | 4,621 | 19,051 |
| | PZ veg, no ag (in) | 1.38 | 1.84 | 1.69 | 1.27 | 2.80 | 0.62 | 1.50 | 1.39 |
| Mean of Low 3 | PZ veg & ag (AF) | 6.8 | 50.0 | 532 | 17,842 | 4,296 | 88.0 | 7,256 | 30,071 |
| | PZ veg, no ag (AF) | 6.8 | 50.0 | 532 | 13,830 | 1,698 | 88.0 | 5,268 | 21,472 |
| | PZ veg, no ag (in) | 1.54 | 2.20 | 1.98 | 1.43 | 3.01 | 0.76 | 1.72 | 1.57 |
| Second Lowest | PZ veg & ag (AF) | 6.9 | 54.7 | 558 | 17,952 | 4,314 | 88.5 | 7,376 | 30,350 |
| | PZ veg, no ag (AF) | 6.9 | 54.7 | 558 | 13,939 | 1,716 | 88.5 | 5,388 | 21,751 |
| | PZ veg, no ag (in) | 1.57 | 2.40 | 2.08 | 1.45 | 3.05 | 0.77 | 1.75 | 1.59 |

The fact that averages of multiple ET_g estimates can produce lower ET_g estimates than that from any particular year results from spatial variability in NDVI* values across the phreatophyte zones. Although the 7/25/08 image produced the lowest annual ET_g estimate between 2007 and 2011, it also contains areas where ET_g values exceed those from one or more other years. The net result was that the Dixie Valley ET_g estimate from the low2avg hybrid approach that was 10% lower than the 2008 estimate.

When looking at the least squares regression models between NDVI* and PSCC, the low3avg NDVI* image produced the best combination of a small intercept value and a high r² value. Reclamation chose to use the low3avg ET_g estimate for each DVHA basin unless the spatial patterns on the low3avg NDVI* image indicated that another formulation provided a much better phreatophyte zone delineation. Edwards Creek Valley was the only basin where such a condition existed. The 8/8/07 and low2avg NDVI* images generated much more distinct phreatophyte zone boundaries than any of the other images. The low2avg image was selected over the 8/8/07 image because interpretation of high-resolution aerial imagery indicated that the 8/8/07 NDVI* values might slightly underestimate PSCC in parts of the Edwards Creek Valley phreatophyte zone.

Reclamation’s final ET_g estimates for each of the seven sub basins in the DVHA are presented in Table 9. The low3avg NDVI* formulation provides the estimates for all but Edwards Creek Valley, which is provided by the low2avg NDVI* formulation.

Table 9. Final ET_g Estimates by DVHA Basin in Acre Feet and Inches

‘no ag’ AF totals exclude ET_g from all agricultural lands, without replacement with estimates of pre-development ET_g.

| Parameter | Sting- aree | Cow- kick | East- gate | Dixie | Pleasant | Jersey | Edwards Creek | DVHA Total |
|--|----------------|--------------|---------------|---------|----------|---------|------------------|---------------|
| Phreatophyte zone area, no ag (acres) | 52.7 | 272.9 | 3,217 | 115,665 | 6,758 | 1,382.4 | 36,862 | 164,210 |
| Final Selection | | | | | | | | |
| PZ veg & ag (AF) | 6.8 | 50.0 | 532 | 17,842 | 4,296 | 88.0 | 6,609 | 29,424 |
| PZ veg, no ag (AF) | 6.8 | 50.0 | 532 | 13,830 | 1,698 | 88.0 | 4,621 | 20,826 |
| PZ veg, no ag (in) | 1.54 | 2.20 | 1.98 | 1.43 | 3.01 | 0.76 | 1.50 | 1.52 |

Discussion

Comparing Results with Those from Other Studies

USGS Eddy Covariance Data and the NDVI* to ET* Relationship

Using 24 site-years of data, Groeneveld et al. (2007) found that ET*, a ratio of actual ET to grass reference ET minus water year precipitation (Equation 13), was well correlated with NDVI*. Figure 25 depicts these data as black dots, as well as the linear model derived from them, and the 90 percent prediction intervals. The relationship between these NDVI* and ET* data is so close to 1:1 that the authors suggested that NDVI* could be substituted for ET*, which was done for this project. Replacing ET* in Equation 13 with NDVI* and rearranging the terms produces Equation 4, which was used to map ETg across the DVHA.

$$ET^* = (ETa - ppt) / (ETo - ppt) \quad (13)$$

where:

- ET* = rescaled evapotranspiration measurement
- ETa = annual evapotranspiration (mm)
- ETo = annual grass reference evapotranspiration (mm)
- ppt = annual precipitation (mm)

Data from Dixie Valley's SV and DV sites are shown as red triangles in Figure 25. Average ET* values for water years 2010 and 2011 measured at the SV and DV sites (the best estimate of the long-term average ET* at these sites) were plotted against low3avg NDVI* values. The SV site is located near the 1:1 line in Figure 25, indicating that NDVI* produced ETg estimates similar to those measured at the USGS SV eddy covariance station (38 mm vs. 53 mm, respectively). Although still within the 90 percent prediction interval of the Groeneveld et al. (2007) regression model, the DV site lies significantly above the 1:1 line, indicating that NDVI* significantly underestimates ETg at the USGS DV eddy covariance station (102 mm vs. 225 mm, respectively). There are several factors that could be influencing this result.

Uncertainty in the DV eddy covariance estimate of ETg itself could explain some of the observed difference in ET*, but the difference between eddy covariance and NDVI* estimates would still be significant even if all of the probable error of 40 mm reported by the USGS (approximately 0.03 ET*) was in the negative direction.

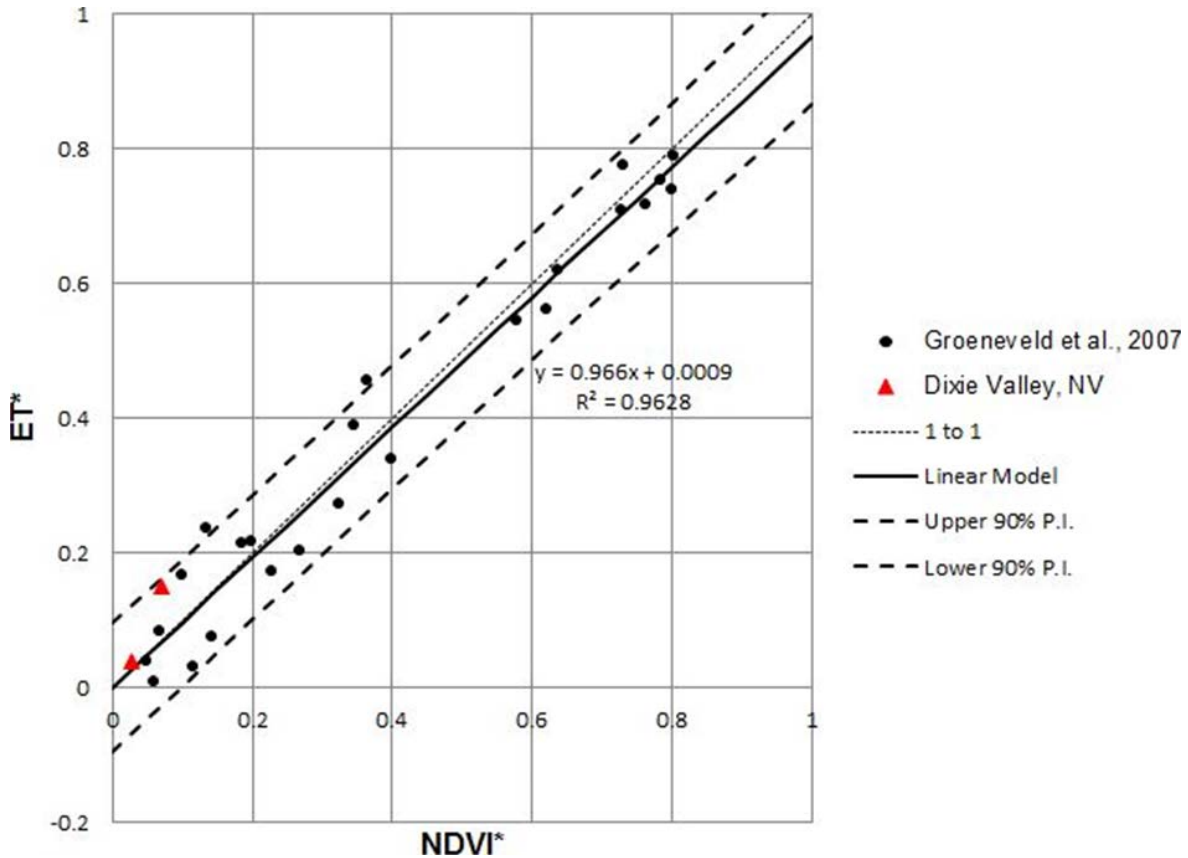


Figure 25. The relationship between NDVI* and ET* developed from data presented in Groeneveld et al. (2007) (black dots) and this study (red triangles). The solid line shows the linear least squares regression, with 90% prediction intervals shown as dashed lines.

Uncertainty is also associated with the method used to calculate the NDVI* value that was paired with the annual ET_g estimate from the DV site. Because of the spatial variability in vegetation density around the DV site and the non-uniform wind direction and wind speed characteristics of the DV site during the summer months, the generalized circular shapes of the fetch areas around the DV eddy station could explain some of the reported difference. For example, using the same 200 m fetch radius as Huntington (2015) increases the NDVI* ET_g estimate at the DV site from 101 mm to 118 mm.

Another possible explanation for the seemingly low NDVI* value at the DV site could be that all of the dense phreatophyte stands retained some of their leaves during the winter, and the method employed to identify dense phreatophyte stands and replace their $NDVI_0$ values with the mean of their immediate surroundings did not produce accurate $NDVI_0$ estimates. But in order for the NDVI*-derived ET_g estimate to equal the measured value at the DV station, the $NDVI_0$ value for the DV station (approximately 0.09) would need to be reduced to 0.01—an extremely low value seen in only 0.1% of the Dixie Valley phreatophyte zone. From the accuracy of the $NDVI_0$ image demonstrated in Figure 12 and the photos

and description of the DV site in Garcia et al. (2014), that magnitude of error in the NDVI₀ estimate is highly unlikely.

The factors accounting for the large difference between the NDVI*-based ET_g prediction and that measured at the DV site are not fully understood. Although the DV site is among the largest outliers in the NDVI* to ET* graph in Figure 25, it is within the 90% prediction intervals established by the original NDVI* to ET* dataset. From the population sampled in Groeneveld's work (black dots in Figure 25), individual deviations from predicted values on the order of that seen at the DV site would be rare, but are not unexpected. However, only 1.0% of the non-agricultural vegetation in the DVPZ produced ET_g estimates equal to or greater than that measured at the DV site, which could indicate a systematic underestimation of ET_g at high-density phreatophyte sites.

Comparisons with ET_g Estimates from Previous Studies

Two other studies were undertaken to estimate annual ET_g within Dixie Valley in the 1960s and the 1990s. Cohen and Everett (1963) and Harrill and Hines (1995) estimated annual ET_g using an "ET Unit" approach in which strata within a given phreatophyte zone are assigned annual ET_g depths. Harrill and Hines (1995) refined the general ET units used in Cohen and Everett (1963), mapping nine different ET units on the basis of vegetation species composition and foliage density. Agricultural water use was not included in the ET_g estimate from either study. No ET_g measurements were made within Dixie Valley for either study, so lysimeter-based ET_g values measured near Winnemucca, Nevada (about 130 km north of the Dixie Valley playa) were correlated with foliage density measurements by phreatophyte species, and these relationships were used to assign ET_g values to the various ET units in Dixie Valley. Total annual ET_g was estimated by multiplying the strata areas by their associated ET_g depths, and summing the results.

Reclamation's ET_g estimates are similar to these previous studies which reported ET_g values of 15–120 mm for areas with phreatophytic shrub cover of about 5–26 percent (Cohen and Everett, 1963; Harrill and Hines, 1995). The PSCC to ET_g relationship for the low3avg NDVI* relationship used to develop ET_g estimates for Dixie Valley (Figure 24) estimates ET_g of 25–120 mm for the same 5–26 percent PSCC range. However, the USGS applied the volume foliage approach used by Harrill and Hines (1995) to the DV and SV sites and found to substantially underestimate measured values (143 mm versus 225 mm for the DV site, 33 mm versus 53 mm for the SV site). Table 10 compares estimated ET_g volumes for the Dixie Valley phreatophyte zone from this this work, Cohen and Everett (1963), Harrill and Hines (1995), and two concurrent studies conducted by the USGS and HH (discussed in the next section). Pre- and post-development Reclamation ET_g estimates are presented. Both pre-development estimates exclude agricultural land (as was done with all studies listed in Table 10), with the smaller of the two estimates further excluding lands with vegetation supported by anthropogenic artesian springs (following the USGS protocol). In all cases,

excluded lands received ET_g estimates from surrounding phreatophyte areas (as is done for both the USGS and HH work). The post-development estimate represents total ET_g from all sources, both natural and anthropogenic. Reclamation’s estimates are similar to the previous studies, but significantly below the USGS and HH estimates. These differences are discussed below.

Table 10. Comparison of Groundwater Discharge Volume Estimates in the Dixie Valley Phreatophyte Zone

| Estimate | Discharge (acre-feet) |
|---|--------------------------|
| Reclamation: pre-development | 13,249–13,962 |
| Reclamation: post-development (including agriculture and all spring-fed vegetation) | 17,842 |
| Cohen and Everett, 1963: pre-development | 13,600 |
| Harrill and Hines, 1995: pre-development | 12,900–14,400 |
| USGS (Garcia et al., 2014): pre-development | 20,400 |
| HH (Huntington, 2015): pre-development | 18,900 |

Comparisons with ET_g Estimates from Concurrent Studies

U.S. Geological Survey

The USGS conducted a parallel effort to estimate groundwater evapotranspiration from Dixie Valley. This study also made use of ET units, and Landsat TM imagery was critical to defining them. The phreatophyte zone was divided into three ET units based upon a ratio of the Enhanced Vegetation Index (EVI; Huete et al., 1999) to brightness temperature in degrees Celsius (T_b; Chander et al., 2009). Summertime EVI/T_b images from 2007, 2009, 2010, and 2011 were processed in an effort to quantify year-to-year variability in vegetation condition. A single summer scene was used to characterize vegetation conditions for 2007, and means of multiple summer images were used to characterize conditions for 2009 (2 images), and 2010–2011 (3 images).

A “sparse shrubland” ET unit defined as having a nominal PSCC of 10% or less was initially mapped separately for each year. Dixie Valley’s central playa defined the lower boundary, and the upper boundaries were defined using EVI/T_b thresholds equal to the mean of EVI/T_b image data collected at the locations of the 17 vegetation transects with PSCC < 10% (with a mean PSCC of 4.1%). The four annual maps were combined into a single final sparse shrubland ET unit. A higher EVI/T_b threshold generated from the 2011 summer EVI/T_b image defined the boundary between the moderate-to-dense shrubland ET unit (nominally 10% to 40% PSCC) and the grassland ET unit. The final sparse shrubland, moderate-to-dense shrubland and grassland ET units contained 70%, 29%, and 1% of the Dixie Valley phreatophyte zone, respectively.

The USGS relied on a linear correlation between PSCC and ET_g to estimate ET_g for the two shrubland ET units which together comprise 99% of the Dixie Valley phreatophyte zone. Although the average coefficient of determination for the regression models predicting PSCC from the four mean summer EVI/Tb images was 0.77, predicted PSCC values from the models were not reliable at low canopy cover values (Figure 26), with the resulting regression model producing negative PSCC estimates for 20% of the Dixie Valley phreatophyte zone. These negative estimates precluded the option of mapping low PSCC areas directly from EVI/Tb. Instead, a sampling approach was adopted in which the mean canopy cover value for the sparse shrubland ET unit (82,009 acres) was estimated using the mean PSCC value from 16 of the 17 USGS transects whose mean EVI/Tb value defined the boundary between the sparse and moderate-to-dense shrubland ET units. The 16 transects used to define mean PSCC for the sparse shrubland ET unit had PSCC values of less than 10%, and were either contained within, or were within one 30-meter pixel of the sparse shrubland ET unit. ET_g was assumed to vary linearly with PSCC, with 0 mm ET_g at zero canopy cover, and 53 mm ET_g at the 7.9% PSCC measured at the SV site. ET_g for the entire sparse shrubland ET unit was computed as the product of the estimated mean sparse shrubland PSCC (4.2%) and the ratio of ET_g to PSCC measured at the SV site (53 mm / 7.9% PSCC), resulting in an estimate of 28 mm.

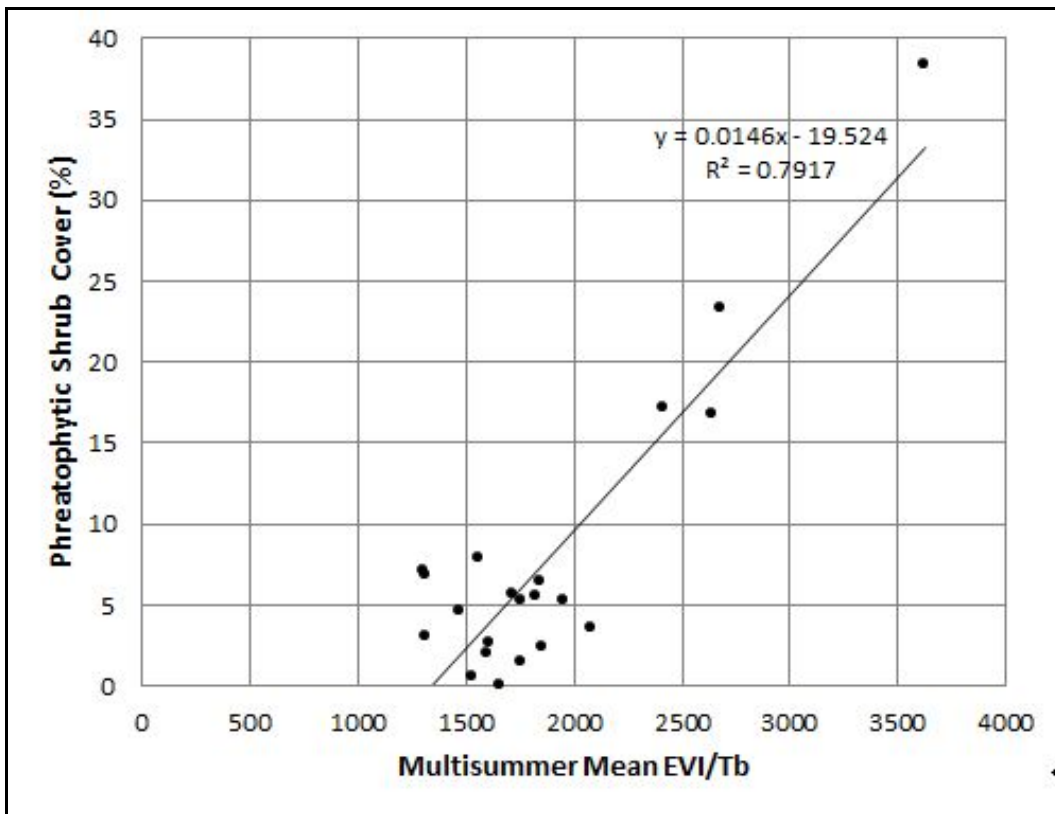


Figure 26. Relationship between averaged mean summer EVI/Tb from 2009 through 2011 and phreatophytic shrub cover.

ET_g for the moderate-to-dense shrubland ET unit (33,730 acres) was calculated for each of the four years as a linear regression between PSCC predicted by EVI/T_b and mean annual ET_g values. A total of five data points defined the regression model to predict PSCC for each summer image. Four data points represented transect locations showing greater than 10 percent canopy cover, while the fifth point paired the mean PSCC from the sparse shrubland ET unit (4.2%) with the minimum EVI/T_b value from the moderate-to-dense shrubland ET unit. Estimated PSCC from each summer image was used to estimate ET_g using linear interpolation defined by two data points: the mean annual ET_g estimates for the DV site (225 mm) and the sparse shrubland ET unit (28 mm) paired with estimated shrub cover at the DV site and the minimum estimated shrub cover for the moderate-to-dense shrubland ET unit.

Grassland ET_g was estimated using a separate linear regression model predicting ET_g directly from ETI/T_b. Low and high data points in this stratum corresponded to the upper end of the moderate-to-dense shrubland class distribution (EVI/T_b associated with 40% PSCC and its estimated ET_g), and the maximum non-agricultural EVI/T_b value from the Dixie Valley phreatophyte zone paired with an assumed maximum annual ET_g value equal to annual ETo minus annual precipitation.

Final ET_g estimates for both the moderate-to-dense shrubland and grassland ET units were calculated as the mean of the 2009–2011 summer mean images. See Garcia et al. (2014) for a complete description of the USGS work.

Comparing USGS and Reclamation ET_g Estimates

Table 11 presents a comparison of the mean values and ranges of ET_g depth estimates from Reclamation and the USGS within the three USGS phreatophyte zone ET units described above. The USGS endeavored to characterize conditions in Dixie Valley prior to human development by masking current and past agricultural lands and a few areas south of the Dixie Valley playa where relatively high vegetation greenness is supported by flowing anthropogenic artesian wells, then filling them in with average ET_g values of their surroundings. The Reclamation data reported in Table 11 were derived from the final Reclamation ET_g map that was masked and filled in a manner identical to that used by the USGS to approximate pre-development conditions. Reclamation maximum and minimum ET_g and PSCC values correspond to 0.1 and 99.9 percentiles of the cumulative histograms to avoid the influence of extreme pixels. Reclamation's image processing scenario also influenced the values in Table 11. ET_g estimates were derived from image data that had been smoothed using a 3x3-pixel averaging filter. While this filtering operation reduces noise and the effects of scene-to-scene misregistration, it also reduces the extreme values, which typically occur in small spatial clumps.

Table 11. Comparison of Reclamation and USGS ETg and Phreatophytic Shrub Canopy Cover (PSCC) Estimates for the Three USGS ET Units

| Estimate | Sparse Shrubland | | Moderate to Dense Shrubland | | Grassland | |
|------------------------------|------------------|----------------|-----------------------------|----------------|-----------|--------------|
| | Mean ETg PSCC | Range ETg PSCC | Mean ETg PSCC | Range ETg PSCC | Mean ETg | Range ETg |
| Reclamation - Predevelopment | 27 mm | 0–92 mm | 44 mm | 0–229 mm | 317 mm | 29–869 mm |
| | 5.7 % | 0–19 % | 9.0 % | 0–47 % | | |
| USGS – Predevelopment | 28 mm | N.A. | 101 mm | 28–499 mm | 503 mm | 140–1,167 mm |
| | 4.2 % | N.A. | 11.0 % | 4–40 % | | |

Reclamation and USGS models predict almost identical mean annual ETg depths for the USGS sparse shrubland ET unit, in spite of differences in estimated PSCC (5.5% from Reclamation, 4.2% from USGS). Differences in mean annual ETg depths are much more pronounced in the moderate-to-dense shrubland ET Unit, in which the USGS estimate is 2.3 times Reclamation’s. USGS estimates of ETg for the grassland ET unit exceed Reclamation’s by a factor of 1.6.

These differences result from the differing structures of the models used to predict ETg from vegetation index values. Reclamation used a single linear relationship between NDVI* and ETg for the entire Dixie Valley phreatophyte zone, based upon the 24 site-years of data presented Groeneveld et al. (2007) (Figure 25). Thus, the incremental impact of a unit change in NDVI* on estimated ETg was constant across the phreatophyte zone. The USGS used a different linear model to estimate ETg for each of the three ET units; the structures of which were defined by adherence to ETg values measured at the SV and DV eddy covariance stations, and an assumed linear relationship between PSCC and ETg for PSCC values between 0 and 40%. The USGS models produced larger changes in ETg for a given change in PSCC for both the sparse shrubland and moderate-to-dense shrubland ET units, which together make up 99% of the Dixie Valley phreatophyte zone. Another difference was that the model used to predict ETg from EVI/Tb in the grassland ET unit was calibrated to assign a value of ETo minus precipitation to the non-agricultural pixel with the highest EVI/Tb value in the Dixie Valley phreatophyte zone (located in the wetlands complex southwest of the Dixie Valley playa). The NDVI* method was calibrated to assign the same maximum ETg value to vigorous agricultural pixels. Using this calibration, the most vigorous non-agricultural vegetation pixel in the Dixie Valley phreatophyte zone received an ETg estimate that was approximately 20% lower than the value assumed by the USGS.

Huntington Hydrologic

Huntington (2015) employed an empirical quadratic model presented in Beamer et al. (2013) to estimate annual ETg for the Dixie Valley phreatophyte zone from EVI imagery (Figure 27). 25 years of imagery from the 1985–2011 date range were processed. The EVI images were generated from Landsat images which had

been processed to surface reflectance using procedures described in Allen et al. (2007) and Tasumi et al. (2008). In an effort to reduce the effect of non-phreatophytic vegetation reflectance on image EVI values, only images acquired in mid-summer (July 17–August 31) were processed. Deriving ET_g estimates as a mean of multiple summer images each year was desired, but images were screened to eliminate those with significant cloud cover or excessive haze. Anywhere from 1 to 3 images were used to estimate ET_g for each year (with the exception of 1990, for which no acceptable images were available). Agricultural lands were masked from the EVI images prior to calculation of ET_g, and replaced with the mean value of all non-agricultural land in the Dixie Valley phreatophyte zone. The summertime mean EVI images provided an ET_g estimate for each year, and the final estimate of 18,900 AF was the median of those 25 ET_g estimates.

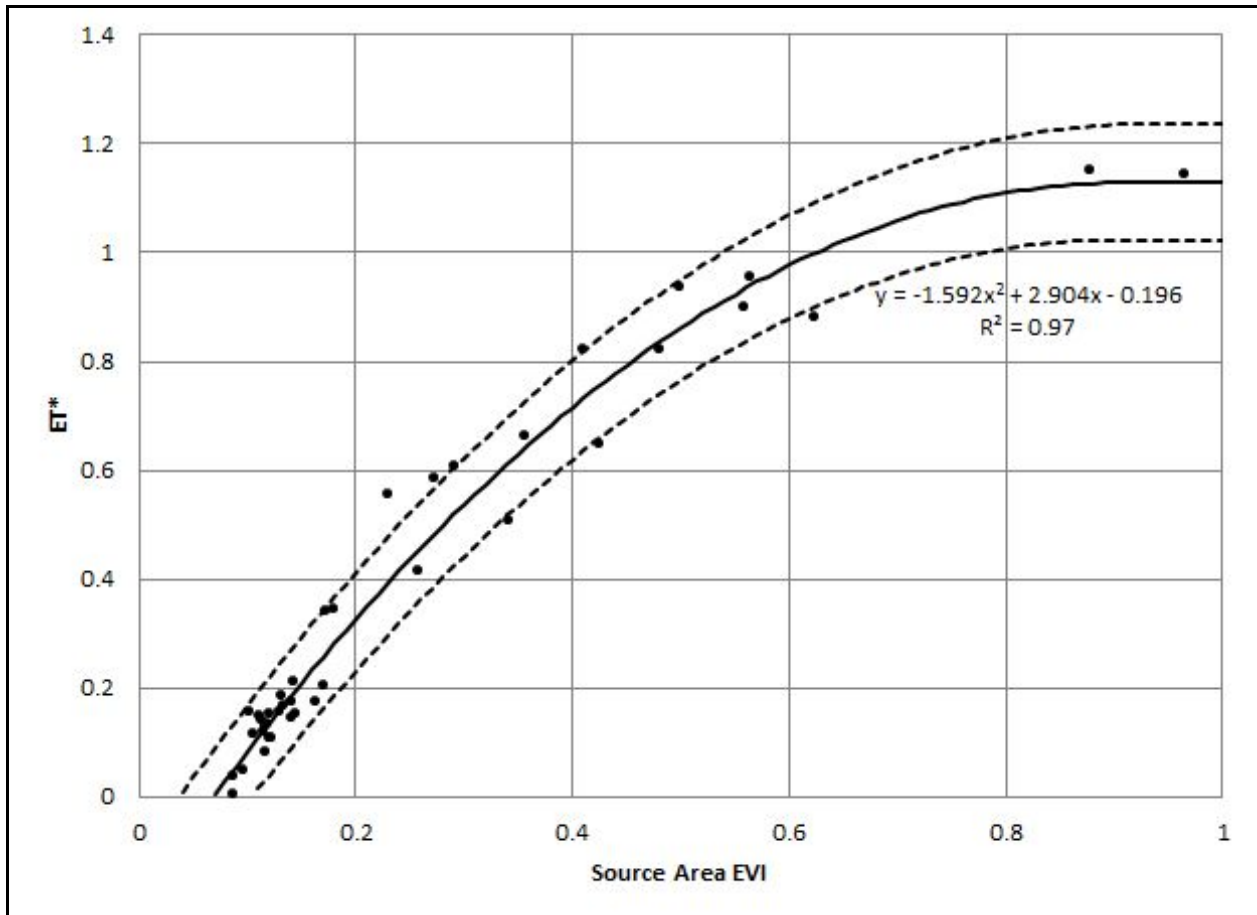


Figure 27. The relationship between NDVI* and ET* developed from data presented in Beamer et al. (2013).

Comparing Huntingtin Hydrologic and Reclamation ETg Estimates

Table 12 compares annual ETg estimates for 2007–2011 generated using EVI and NDVI*, as well as the 5-year average and final Dixie Valley ETg estimates. HH masked all agricultural lands from Dixie Valley prior to generating annual ETg estimates, and estimated ETg for those agricultural areas as the mean of all non-agricultural lands within the phreatophyte zone. For the purpose of comparison in Table 12, Reclamation reprocessed annual NDVI* ETg estimates using the same agricultural land masking and filling procedure as HH. Reclamation’s final ‘low3avg’ ETg estimate excluding agriculture is identical to that in Table 10, and was generated by replacing the ETg of agricultural pixels with the average of their neighbors, following the USGS procedure. Although HH and Reclamation ETg estimates for 2007 and 2008 differ significantly and in opposite directions, Reclamation ETg estimates for 2009–2011 are about 10% lower than the corresponding HH estimates, with Reclamation’s five-year average ETg being only 7% lower than that produced by HH. Reclamation’s final Dixie Valley ETg estimate of 13,962 AF is 26% lower than the final HH estimate of 18,900 AF, but it falls within the 90% prediction intervals of HH’s estimate (12,872 AF to 24,931 AF).

Table 12. Comparison of Reclamation and Huntington Hydrologic ETg Estimates

| Year | Dixie Valley phreatophyte zone ETg (AF), agricultural lands replaced | | |
|----------------------|--|--------------------------|------------------|
| | HH (from EVI) | Reclamation (from NDVI*) | Reclamation / HH |
| 2007 | 15,344 | 19,222 | 1.2527 |
| 2008 | 18,720 | 13,921 | 0.7436 |
| 2009 | 16,372 | 15,117 | 0.9233 |
| 2010 | 22,675 | 20,614 | 0.9091 |
| 2011 | 20,706 | 18,539 | 0.8953 |
| Average of 2007–2011 | 18,763 | 17,483 | 0.9318 |
| Final estimate | 18,900 | 13,962 | 0.7387 |

Dixie Valley phreatophyte zone ETg estimates generated from NDVI* and EVI differ so much more than estimates for individual years because of the different ways Reclamation and HH attempted to reduce the effect of ephemeral, non-phreatophytic vegetation on the vegetation indices. HH recognized the importance of minimizing the effect of non-phreatophytic vegetation on the EVI values used to estimate ET*, and endeavored to reduce its effect by selecting only mid-summer images to characterize phreatophyte ET*, thereby avoiding the spring and early summer dates when non-phreatophytes can dominate the composite EVI response. But after this processing, annual ETg estimates for Dixie Valley varied by a factor of four over the 25-year period of record: between a minimum estimate of 8,378 AF in 1992, and the maximum of 35,601 in 2005. Given that mid-summer soil background variations are largely constant from one

year to the next, such variability between years is most likely tied to variation in the density and/or condition of non-phreatophytic plants within the phreatophyte zone, along with variations in phreatophyte leaf area.

The NDVI* method used by Reclamation to map ET* is predicated on the assumption that the vegetation signal present in the NDVI* data comes from phreatophytic vegetation only. Consequently, care was taken to minimize the contribution of non-phreatophytic vegetation to the NDVI* signal. Study of NDVI* images for each of the years between 2007 and 2011 showed that each exhibited some areas of elevated NDVI* values arising from non-phreatophytic vegetation. Reclamation's averaging of the lowest three ETg estimates (the lowest two in Edwards Creek Valley) was implemented on a pixel-by-pixel basis as a means of reducing the impact of years with significant non-phreatophyte NDVI* response on the final ETg estimates. Processing multirate imagery on a pixel-by-pixel basis rather than a scene-by-scene basis is responsible for most of the 26% difference in HH and Reclamation results.

Reclamation's Implementation of the NDVI* Method

The relationship between NDVI* and phreatophyte ETg described in Groeneveld et al. (2007) was developed using 24 water year ETg estimates measured between 1999 and 2002 at 15 locations in the San Luis Valley, CO, Bosque del Apache, NM, and the Owens Valley, CA. To define the relationship, water year ETg estimates from eddy covariance and Bowen Ratio stations were paired with NDVI* values from the average of the 3x3 pixel block of Landsat pixels containing the stations. A single soil background NDVI value ($NDVI_0$) was defined from the cumulative histogram of each NDVI image. Under this processing scenario, any errors in image calibration were largely irrelevant because their effects were essentially eliminated during the process of rescaling NDVI to NDVI*.

In Dixie Valley, significant variability in soil background NDVI across the phreatophyte zone made this kind of processing scenario impossible. Documented variation in soil background NDVI was larger than the difference in NDVI between the leaf-off and leaf-on conditions for more than 99% of the pixels in the Dixie Valley phreatophyte zone (measured on the 7/28/09 image). The unwanted variation in $NDVI_0$ values caused by changing soil background conditions would have added a significant noise component to the NDVI* signal from the target: transpiring leaves on phreatophytic plants. Discussions with David Groeneveld of HydroBio, Inc. led to the idea using a leaf-off NDVI image to quantify spatially varying soil background NDVI. Inspection of multiple potential leaf-off scenes led to the conclusion that a single leaf-off image could not adequately characterize $NDVI_0$, and that a composite $NDVI_0$ image composed of minimum NDVI values from many potential leaf-off scenes was required. This change was necessary, but it was a significant departure from the

original NDVI* method, and required much more careful preparation of the Landsat data.

Although NDVI₀ values from this project closely match surface-measured soil background NDVI (Figure 12) and produce NDVI* data that correlate well with PSCC data (Figures 21 and 23), there is a question as to whether Reclamation's implementation of NDVI* is somehow different enough from the original implementation that the 1:1 relationship between NDVI* and ET* presented in Groeneveld et al. (2007), no longer applies. Future work can assess the efficacy of NDVI₀ images generated as multi-year minima of leaf-off NDVI images more effectively than was done during this project by comparing NDVI₀ values with soil background NDVI values generated from surface reflectance data acquired over both soil and vegetation canopy during leaf-off conditions. But the larger question of whether the new NDVI* images actually correlate 1:1 to ET* can only be answered through analysis of new data or reprocessing of existing datasets.

Applying the NDVI* Method Using LEDAPS Imagery

The NDVI* method as implemented in this project requires image data that are calibrated to surface reflectance prior to NDVI generation, as uncontrolled atmospheric effects add significant noise to the image data, making reliable ET_g estimation impossible. The reflectance calibration procedure performed for this project was labor intensive, and required stable calibration targets to be present in every satellite image being processed—a condition that is not met everywhere.

After the image calibration work for this project was complete, the USGS EROS (Earth Resources Observation and Science) Center began to make available Landsat TM images processed to apparent surface reflectance using the Landsat Ecosystem Disturbance Adaptive Processing System (LEDAPS) automated procedure (Masek et al., 2006). Later, the USGS also made available several vegetation indices, including NDVI, derived from LEDAPS-processed surface reflectance imagery. Reclamation re-ran the NDVI* procedure using LEDAPS-derived NDVI data, with the only substantial difference being that 3x3 averaging was performed on the NDVI images themselves, rather than the surface reflectance data from which NDVI was calculated. Final ET_g estimates from the two data sets are reported in Tables 13 and 14.

Table 13. Comparison of 2007–2011 ETg Estimates Generated from TM Image Data Calibrated to Surface Reflectance Using the Reclamation (BOR) and LEDAPS Procedures

| Estimate | Parameter | Stingaree | Cowkick | Eastgate | Dixie | Pleasant | Jersey | Edwards Creek | DVHA Total |
|----------------|---------------------------------------|--------------|--------------|--------------|--------------|--------------|--------------|---------------|--------------|
| All | Phreatophyte zone area, no ag (acres) | 52.7 | 272.9 | 3,217 | 115,665 | 6,758 | 1,382 | 36,862 | 164,210 |
| 8/8/07 | BOR refl PZ veg & ag (AF) | 5.5 | 31.6 | 363 | 21,111 | 4,862 | 136 | 6,582 | 33,091 |
| | LEDAPS PZ veg & ag (AF) | 6.6 | 33.8 | 404 | 18,662 | 3,934 | 104 | 6,902 | 30,047 |
| | LEDAPS / BOR | 1.200 | 1.070 | 1.113 | 0.884 | 0.809 | 0.765 | 1.049 | 0.908 |
| | BOR refl PZ veg, no ag (AF) | 5.5 | 31.6 | 363 | 18,870 | 2,093 | 136 | 4,380 | 25,879 |
| | LEDAPS PZ veg, no ag (AF) | 6.6 | 33.8 | 404 | 16,423 | 1,284 | 104 | 4,699 | 22,954 |
| | LEDAPS / BOR | 1.200 | 1.070 | 1.113 | 0.870 | 0.613 | 0.765 | 1.073 | 0.887 |
| 7/25/08 | BOR refl PZ veg & ag (AF) | 10.4 | 76.8 | 892 | 17,285 | 4,741 | 93.0 | 8,327 | 31,424 |
| | LEDAPS PZ veg & ag (AF) | 12.6 | 85.3 | 1,010 | 17,322 | 4,002 | 91.9 | 9,600 | 32,124 |
| | LEDAPS / BOR | 1.212 | 1.111 | 1.132 | 1.002 | 0.844 | 0.988 | 1.153 | 1.022 |
| | BOR refl PZ veg, no ag (AF) | 10.4 | 76.8 | 892 | 13,666 | 1,826 | 93.0 | 6,207 | 22,772 |
| | LEDAPS PZ veg, no ag (AF) | 12.6 | 85.3 | 1,010 | 13,703 | 1,205 | 91.9 | 7,465 | 23,572 |
| | LEDAPS / BOR | 1.212 | 1.111 | 1.132 | 1.003 | 0.660 | 0.988 | 1.203 | 1.035 |
| 7/28/09 | BOR refl PZ veg & ag (AF) | 7.3 | 83.3 | 605 | 18,888 | 4,230 | 97.2 | 9,264 | 33,174 |
| | LEDAPS PZ veg & ag (AF) | 8.9 | 88.7 | 688 | 18,588 | 3,643 | 94.0 | 10,123 | 33,235 |
| | LEDAPS / BOR | 1.219 | 1.065 | 1.137 | 0.984 | 0.861 | 0.967 | 1.093 | 1.002 |
| | BOR refl PZ veg, no ag (AF) | 7.3 | 83.3 | 605 | 14,840 | 1,558 | 97.2 | 7,262 | 24,453 |
| | LEDAPS PZ veg, no ag (AF) | 8.9 | 88.7 | 688 | 14,557 | 1,055 | 94.0 | 8,115 | 24,607 |
| | LEDAPS / BOR | 1.219 | 1.065 | 1.137 | 0.981 | 0.677 | 0.967 | 1.117 | 1.006 |
| 7/31/10 | BOR refl PZ veg & ag (AF) | 8.2 | 72.0 | 758 | 24,278 | 4,597 | 197 | 8,385 | 38,294 |
| | LEDAPS PZ veg & ag (AF) | 10.6 | 81.8 | 896 | 23,660 | 4,034 | 189 | 9,545 | 38,415 |
| | LEDAPS / BOR | 1.293 | 1.136 | 1.182 | 0.975 | 0.878 | 0.959 | 1.138 | 1.003 |
| | BOR refl PZ veg, no ag (AF) | 8.2 | 72.0 | 758 | 20,236 | 1,919 | 197 | 6,404 | 29,593 |
| | LEDAPS PZ veg, no ag (AF) | 10.6 | 81.8 | 896 | 19,632 | 1,410 | 189 | 7,548 | 29,767 |
| | LEDAPS / BOR | 1.293 | 1.136 | 1.182 | 0.970 | 0.735 | 0.959 | 1.179 | 1.006 |
| 8/3/11 | BOR refl PZ veg & ag (AF) | 9.7 | 58.4 | 822 | 22,213 | 5,184 | 290 | 11,619 | 40,197 |
| | LEDAPS PZ veg & ag (AF) | 15.0 | 82.7 | 1,107 | 31,657 | 5,211 | 387 | 15,092 | 53,551 |
| | LEDAPS / BOR | 1.546 | 1.416 | 1.347 | 1.425 | 1.005 | 1.334 | 1.299 | 1.332 |
| | BOR refl PZ veg, no ag (AF) | 9.7 | 58.4 | 822 | 18,200 | 2,587 | 290 | 9,631 | 31,598 |
| | LEDAPS PZ veg, no ag (AF) | 15.0 | 82.7 | 1,107 | 27,620 | 2,613 | 387 | 13,064 | 44,889 |
| | LEDAPS / BOR | 1.546 | 1.416 | 1.347 | 1.518 | 1.010 | 1.334 | 1.356 | 1.421 |

Table 14. Comparison of Hybrid ETg Estimates Generated from TM Image Data Calibrated to Surface Reflectance Using the Reclamation (BOR) and LEDAPS Procedures

| Estimate | Parameter | Stingaree | Cowkick | Eastgate | Dixie | Pleasant | Jersey | Edwards Creek | DVHA Total |
|----------------------|---------------------------------------|--------------|--------------|--------------|--------------|--------------|--------------|---------------|--------------|
| All | Phreatophyte zone area, no ag (acres) | 52.7 | 272.9 | 3,217 | 115,665 | 6,758 | 1,382 | 36,862 | 164,210 |
| Mean of Low 2 | BOR refl PZ veg & ag (AF) | 6.1 | 41.9 | 452 | 16,294 | 4,177 | 71.1 | 6,609 | 27,650 |
| | LEDAPS PZ veg & ag (AF) | 7.6 | 51.0 | 529 | 16,449 | 3,623 | 65.2 | 7457 | 28,182 |
| | LEDAPS / BOR | 1.246 | 1.217 | 1.170 | 1.010 | 0.867 | 0.917 | 1.128 | 1.019 |
| | BOR refl PZ veg, no ag (AF) | 6.1 | 41.9 | 452 | 12,281 | 1,579 | 71.1 | 4,621 | 19,051 |
| | LEDAPS PZ veg, no ag (AF) | 7.6 | 51.0 | 529 | 12,412 | 1,025 | 65.2 | 5,430 | 19,520 |
| | LEDAPS / BOR | 1.246 | 1.217 | 1.170 | 1.011 | 0.649 | 0.917 | 1.175 | 1.025 |
| Mean of Low 3 | BOR refl PZ veg & ag (AF) | 6.8 | 50.0 | 532 | 17,842 | 4,296 | 88.0 | 7,256 | 30,071 |
| | LEDAPS PZ veg & ag (AF) | 8.6 | 59.6 | 635 | 17,869 | 3,717 | 81.3 | 8,201 | 30,572 |
| | LEDAPS / BOR | 1.265 | 1.192 | 1.194 | 1.002 | 0.865 | 0.924 | 1.130 | 1.017 |
| | BOR refl PZ veg, no ag (AF) | 6.8 | 50.0 | 532 | 13,830 | 1,698 | 88.0 | 5,268 | 21,472 |
| | LEDAPS PZ veg, no ag (AF) | 8.6 | 59.6 | 635 | 13,833 | 1,119 | 81.3 | 6,173 | 21,909 |
| | LEDAPS / BOR | 1.265 | 1.192 | 1.194 | 1.000 | 0.659 | 0.924 | 1.172 | 1.020 |
| Second Lowest | BOR refl PZ veg & ag (AF) | 6.9 | 54.7 | 558 | 17,952 | 4,314 | 88.5 | 7,376 | 30,350 |
| | LEDAPS PZ veg & ag (AF) | 8.8 | 69.1 | 663 | 17,928 | 3,730 | 80.0 | 8,465 | 30,943 |
| | LEDAPS / BOR | 1.275 | 1.263 | 1.188 | 0.999 | 0.865 | 0.904 | 1.148 | 1.020 |
| | BOR refl PZ veg, no ag (AF) | 6.9 | 54.7 | 558 | 13,939 | 1,716 | 88.5 | 5,388 | 21,751 |
| | LEDAPS PZ veg, no ag (AF) | 8.8 | 69.1 | 663 | 13,891 | 1,132 | 80.0 | 6,437 | 22,281 |
| | LEDAPS / BOR | 1.275 | 1.263 | 1.188 | 0.997 | 0.660 | 0.904 | 1.195 | 1.024 |

Inspection of Table 13 shows close agreement between ET_g estimates generated using the two different surface reflectance data sets for 2008–2010. Although proportional differences for Stingaree, Cowkick, Eastgate, Pleasant, and Jersey Valleys can be significant, their areas are small, together accounting for about 7% of the area within the DVHA. Between 2008 and 2010, ET_g estimates derived from Reclamation- and LEDAPS-processed TM imagery for Dixie Valley and the DVHA differed by a maximum of 3% and 3.5%, respectively. Differences were more significant for 2007, but Dixie Valley and DVHA estimates were still within 13% and 11.3% of each other, respectively. Only in 2011 were there widely divergent estimates, with LEDAPS imagery producing ET_g estimates that were 52% greater than Reclamation-processed imagery for non-agricultural lands within Dixie Valley. The agreement in final ET_g estimates generated using the two calibration methods is also very strong for the hybrid methods presented in Table 14, where differences between Reclamation and LEDAPS calibration methods never exceed 2.5%.

The availability of freely available NDVI imagery generated from surface reflectance data is a significant development which will allow for further validation of the NDVI* procedure for estimating phreatophyte ET_g, and for its possible application across the West.

Appendix—Calculating Bidirectional Reflectance Factors for the Spectralon SRS-99 Reference Panel

NASA’s Jet Propulsion Laboratory (JPL) measured BRF and DHR values from Spectralon material using a 633 nm non-polarized laser as the illumination source (Bruegge et al., 2001). Figure A-1 shows a 3-D view of BRF values using five different light source locations. It is clear from Figure A-1 that Spectralon reflectance becomes less isotropic at larger illumination angles (measured from surface normal). Table A-1 and Figure A-2 show that BRF values for a normal view angle to the Spectralon panel can differ significantly from DHR values, and the magnitude and direction of these differences vary with illumination angle.

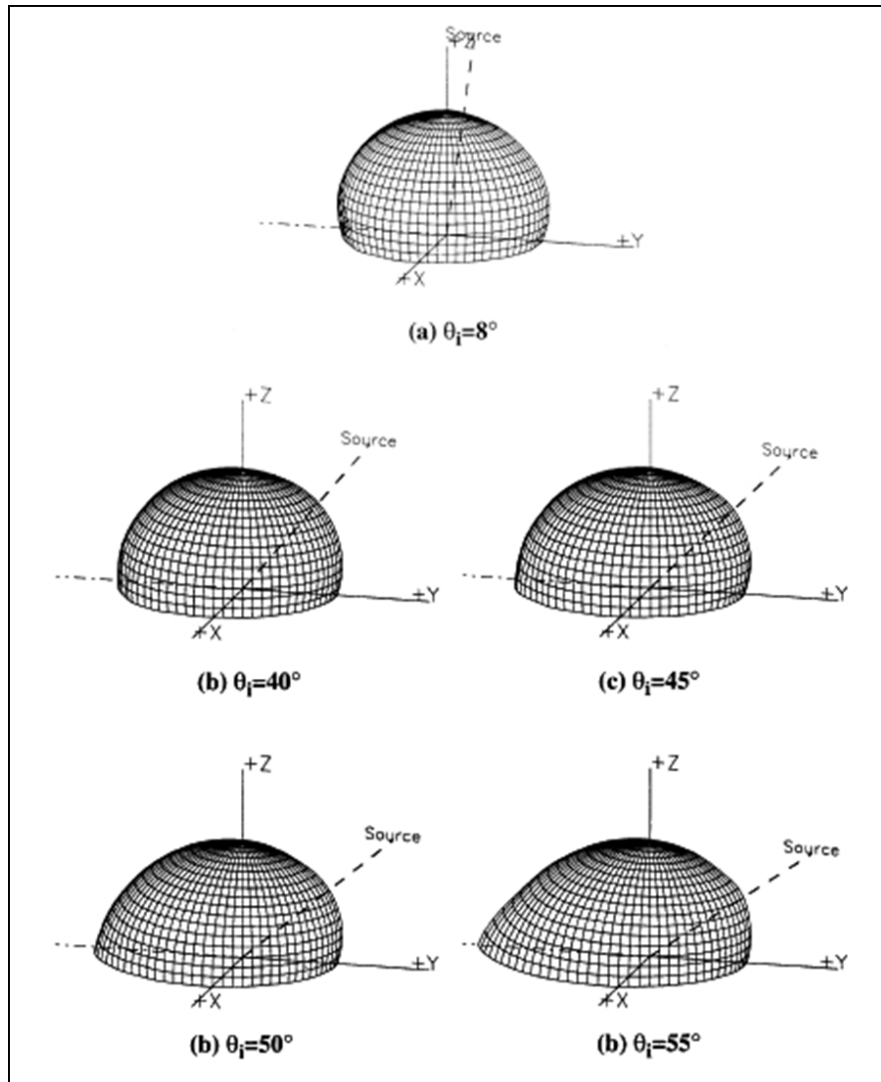


Figure A-1. Measured hemispheric BRF of Spectralon at 632.8 nm (from Bruegge et al., 2001).

Table A-1. Spectralon BRF and DHR for a Nadir-Viewing Sensor at 632.8 nm (from Bruegge et al., 2001)

| Illumination, θ_i ($^\circ$) | BRF, $R(\theta_i; 0^\circ)$ | DHR, $\rho(\theta_i; 2\pi)$ |
|---------------------------------------|-----------------------------|-----------------------------|
| 8 | 1.045 | 0.991 |
| 40 | 1.004 | 0.990 |
| 45 | 0.994 | 0.993 |
| 50 | 0.983 | 0.983 |
| 55 | 0.972 | 0.990 |

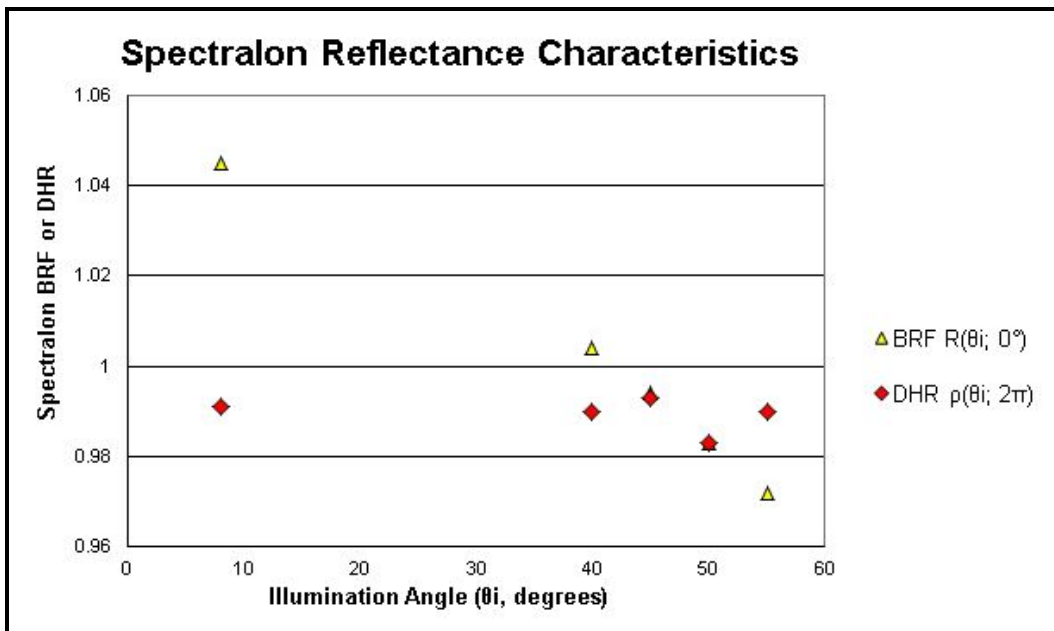


Figure A-2. Spectralon DHR and BRF values measured normal to the panel at five different illumination angles.

Determining Wavelength-Specific Spectralon Reflectance Factors in the Visible and Near Infrared

Figure A-3 plots Spectralon BRDF values (equal to BRF / π) for a number of wavelengths of non-polarized light in the visible and near infrared portions of the spectrum at a wide range of illumination and view angles. These data were measured by National Institute of Standards and Technology (NIST) and reported in Early et al. (2000). These data show that non-polarized light reflected from a Spectralon panel in a direction normal to the panel is sensitive to illumination angle, but shows little wavelength dependence in the 440–940 nm range.

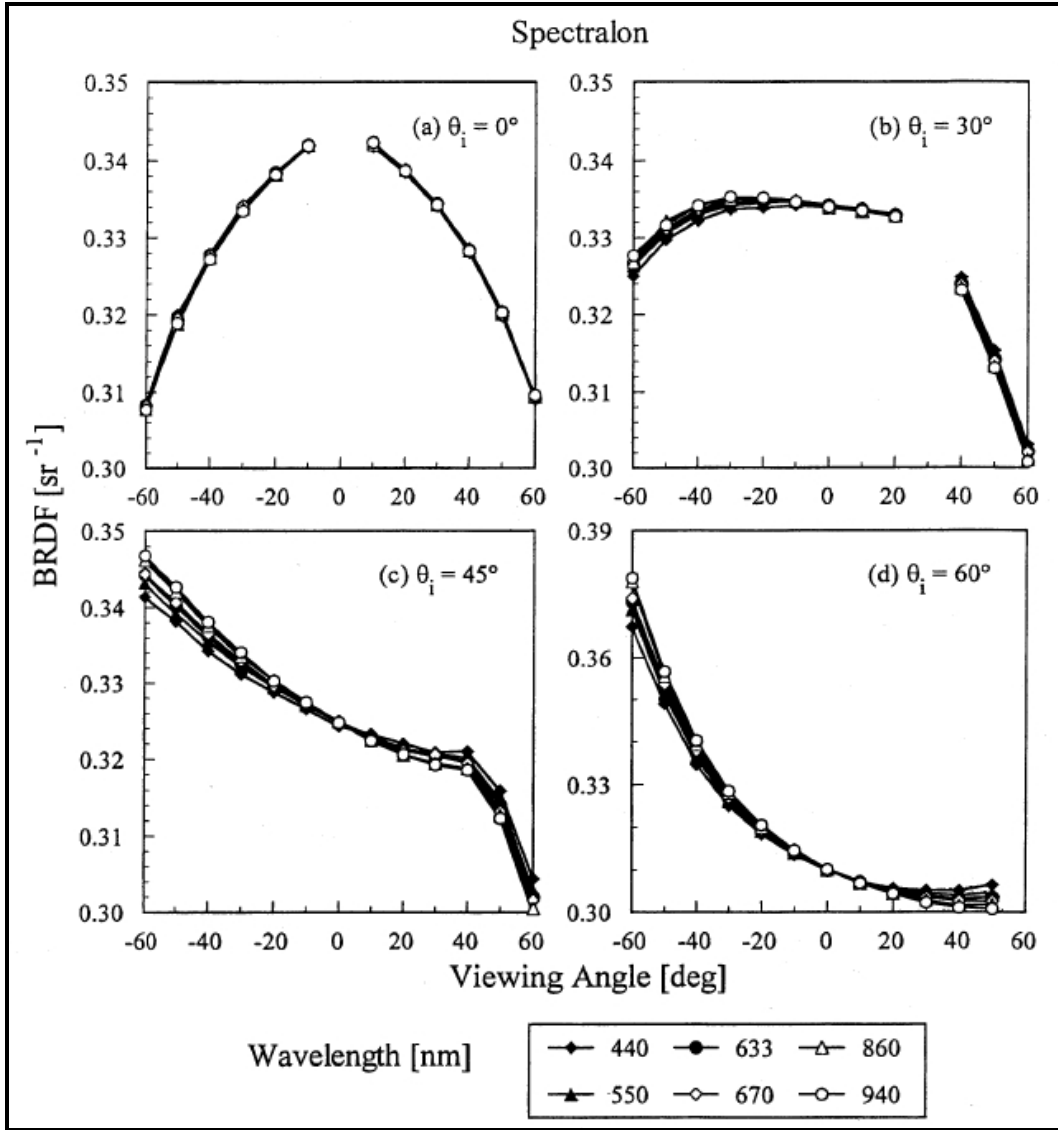


Figure A-3. Spectralon BRDF (bidirectional reflectance distribution function) as a function of viewing angle for four different illumination angles, from NIST measurements.

The incidence angles are indicated in the panels, and the wavelengths are given in the legend (from Early et al., 2000). At view angles normal to the Spectralon panel (view angle = 0°), BRDF values vary little with wavelength. $\text{BRDF} = \text{BRF}/\pi$.

Figure A-3 displays NIST BRDF values for multiple wavelengths of light at multiple illumination and viewing geometries (with the sensor along the plane of the illumination source); while the JPL data presented in Table A-1 and Figures A-1 and A-2 were collected over an entire hemisphere with variable illumination angles, but using only a single wavelength of laser light (633 nm). Spectralon BRFs calculated from NIST and JPL data varied slightly, but integration of BRF values from the 8° illumination angle JPL data set over the entire hemisphere agreed to within 0.14% of the directional/hemispherical reflectance values for Spectralon reported by LabSphere (which were generated using the same

illumination angle, polarization, and laser wavelength). Therefore, the JPL data presented in Bruegge et al. (2001) were used to define an empirical equation that predicts Spectralon BRF at a normal view angle in the 440–940 nm spectral range from illumination angle. The transformation of the incidence angle in Equation A-1 effectively linearized the relationship between incidence angle and Spectralon BRF.

$$\text{BRF}_{\text{est},\theta_i/0^\circ} = 1.0477 - 0.000075561 \theta_i^{1.725} \quad (\text{A-1})$$

where:

$\text{BRF}_{\text{est},\theta_i/0^\circ}$ = estimated Spectralon bidirectional reflectance factor with illumination and view angles θ_i and 0, respectively (measured from surface normal)

θ_i = illumination angle (degrees from surface normal)

While the NIST BRDF values for a nadir look angle presented in Figure A-3 show little variation over the six specific wavelengths in the 440–940 nm range, a method was needed to estimate BRDF values for other wavelengths. LabSphere provides detailed DHR data for its Spectralon panels in the 350 to 2500 nm spectral range, so a method of linking DHR to BRF (or BRDF) values was needed. Yoon et al. (2009) showed that 0°/45° (incidence / view) BRF values for a Spectralon 99% DHR panel vary consistently with 6°/hemispheric DHR values in the 300–1300 nm range, but that relationship begins to change significantly between 1300 nm and 1700 nm (Figure A-4). The reciprocity principle holds that BRF values remain the same if illumination and view positions are switched, so the data presented in Figure A-4 can be considered identical to a 45° illumination angle and a normal view angle.

An assumption was made that because BRF for the 0°/45° condition tracked well with DHR, BRF values for other incidence / view conditions would as well. Given the correlation between DHR and BRF values, and the nearly uniform Spectralon DHR values in the 600-1150 nm region, the 632.8 nm BRF values predicted by Equation A-1 were assumed to represent BRF values for the entire 600-1150 nm range. For wavelengths in the 350–599 and 1151–1300 nm region, BRF values estimated using Equation A-1 were scaled downward slightly by ratioing their DHR values to the average DHR value for the 600-1150 nm range (Equation A-2).

$$\text{BRF}_{\text{corr},\lambda,\theta_i/0^\circ} = \text{DHR}_{\text{spec},\lambda} / \text{DHR}_{\text{spec},\lambda 600-1150} \quad (\text{A-2})$$

where:

$\text{BRF}_{\text{corr},\lambda,\theta_i/0^\circ}$ = multiplicative correction factor for wavelength λ to be applied to BRF values estimated for incidence and view angles θ_i and 0, respectively, using Equation A-3

$\text{DHR}_{\text{spec},\lambda}$ = Spectralon directional/hemispheric reflectance for wavelength λ

$DHR_{spec,\lambda 600-1150}$ = average Spectralon DHR for the 600–1150 nm range
(0.989592)

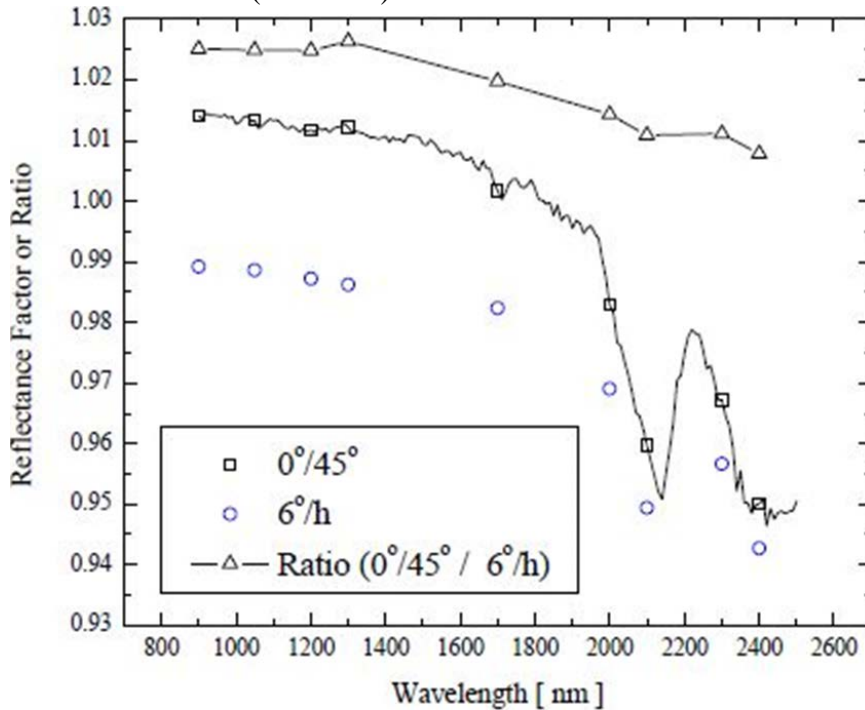


Figure A-4. 0°/45° and 6°/hemispherical (incidence/view) reflectance factors of Spectralon and their ratios (from Yoon et al., 2009). The ratio of BRF/DHR is fairly constant from 900 to 1300 nm, but begins to drop off at wavelengths ≥ 1300 nm.

Final BRF values for the 350–1300 nm region were calculated by multiplying the estimated BRF value from Equation A-1 by the wavelength-dependent correction factor from Equation A-2 (Equation A-3).

$$BRF_{\lambda,\theta_i/0^\circ} = BRF_{est,\theta_i/0^\circ} * BRF_{corr,\lambda,\theta_i/0^\circ} \quad (A-3)$$

where:

$BRF_{\lambda,\theta_i/0^\circ}$ = bidirectional reflectance factor at wavelength λ and illumination and view angles θ_i and 0, respectively (measured from surface normal)

$BRF_{est,\theta_i/0^\circ}$ = estimated Spectralon bidirectional reflectance factor for illumination and view angles θ_i and 0, respectively (from Equation A-1)

$BRF_{corr,\lambda,\theta_i/0^\circ}$ = multiplicative correction factor for wavelength λ to be applied to BRF values estimated for incidence and view angles θ_i and 0, respectively, using Equation A-1 (from Equation A-2)

Determining Spectralon Reflectance Factors in the Shortwave Infrared (1301 nm – 2500 nm)

Figure A-4 shows that the 0°/45° BRF/DHR ratio decreases towards 1.0 in the SWIR (shortwave infrared) wavelengths greater than 1300 nm. This indicates that the application of Equation A-3 beyond 1300 nm is not warranted because the assumption of the constant relationship between 0°/45° BRF and DHR values is no longer valid.

An alternate procedure was developed to estimate BRF values in the SWIR wavelengths beyond 1300 nm for the solar zenith angles present during instrument calibration. The procedure described below was developed quickly from limited data. Simply described, it rescales BRF values estimated for 1300nm using equation A-3 in the same proportion as seen in the data presented in Figure A-4. It was deemed adequate for the purposes of this study, as spectral bands 5 and 7 were the only TM or ETM+ spectral bands that fell within this spectral range, and neither of them were used in the development of vegetation indices used in this project.

Yoon et al. (2009) speculated that the observed decrease in 0°/45° BRF/DHR values with increasing wavelength in Figure A-4 could arise from the chemical absorption peaks in Spectralon centered at 2100 and 2400 nm, and this could result in more lambertian reflectance at these wavelengths. But the authors warned that further off-angle measurements of reflectance in this spectral region would be needed to determine if this idea was correct. Reclamation chose to assume that this hypothesis was true—that as wavelengths increased, the BRF/DHR values for the pre-flight (54.76°) and post-flight (56.78°) solar zenith angles would converge on unity in the same proportion as that seen in the 0°/45° BRF/DHR ratios plotted in Figure A-4.

Equation A-3 was used to estimate the Spectralon BRF for a particular illumination angle at 1300 nm, and this value was divided by the Spectralon DHR to define the value that would be scaled towards 1.0 in the same proportion as the BRF/DHR values for 0°/45° shown in Figure A-4. For all wavelengths in the 1301–2500 nm range, final Spectralon BRF values were obtained by multiplying the scaled BRF/DHR value by the DHR value for that wavelength (Equation A-4).

$$\text{BRF}_{\lambda, \theta_i/0^\circ} = \text{DHR}_\lambda * \left(1 + \left[\frac{((\text{BRF}_{\lambda, 0^\circ/45^\circ}/\text{DHR}_\lambda) - 1)}{((\text{BRF}_{1300\text{nm}, 0^\circ/45^\circ}/\text{DHR}_{1300\text{nm}}) - 1)} * ((\text{BRF}_{1300\text{nm}, \theta_i/0^\circ}/\text{DHR}_{1300\text{nm}}) - 1) \right] \right) \quad (\text{A-4})$$

where:

DHR_λ = directional hemispherical reflectance at wavelength λ
 $\text{BRF}_{\lambda, 0^\circ/45^\circ}$ = BRF at wavelength λ , view/illumination angles 0°/45°
 (from Yoon et al., 2009)

Dixie Valley Groundwater Export Study

$BRF_{1300nm,0^{\circ}/45^{\circ}}$ = BRF at 1300nm, view/illumination angles $0^{\circ}/45^{\circ}$ (from Yoon et al., 2009)

DHR_{1300nm} = DHR at 1300 nm

$BRF_{1300nm,\theta_i/0^{\circ}}$ = BRF at 1300 nm, illumination/view angles $\theta_i/0^{\circ}$ (θ_i = solar zenith angle at time of Spectralon measurement)

References

- American Society of Civil Engineers-Environmental and Water Resources Institute, 2005. *The ASCE Standardized Reference Evapotranspiration Equation*. ASCE-EWRI Standardization of Reference Evapotranspiration Task Committee Report, ASCE.
- Baugh, W.M. and D.P. Groeneveld, 2006. Broadband vegetation index performance evaluated for a low-cover environment. *International Journal of Remote Sensing*, 27 (21):. 4715-4730.
- Bruegge, Carol, Nadine Chrien, and David Haner, 2001. A Spectralon BRF data base for MISR calibration applications, *Remote Sensing of Environment* 72, 354–366.
- Chander, G., Markham, B.L., and Helder, D.L., 2009. Summary of current radiometric calibration coefficients for Landsat MSS, TM, ETM+, and EO-1 ALI sensors. *Remote Sensing of Environment* 113 (5): 893–903.
- Cohen, P. and D.E. Everett, 1963. A brief appraisal of the ground'water hydrology of the Dixie-Fairview Valley area, Nevada: U.S. Geological Survey Ground-Water Resources Reconnaissance Series Report 23, 40 p.
- Early, E.A., P.Y. Barnes, B.C. Johnson, J.J. Butler, C.J. Bruegge, S.F. Biggar, P.R. Spyak, and M.M. Pavlov, 2000. Bidirectional Reflectance Round-Robin in Support of the Earth Observing System Program, *Journal of Atmospheric and Oceanic Technology* 17: 1077-1091.
- Garcia, C.A., J.M. Huntington, S.G. Buto, M.T. Moreo, J.L. Smith, and B.J. Andraski, 2014. Groundwater discharge by evapotranspiration, Dixie Valley, west-central Nevada, March 2009–September 2011: U.S. Geological Survey Professional Paper 1805, 96 p.
- Gillies, R.R., Carlson, T.N., Cui, J., Kustas, W.O., and Humes, K.S., 1997. A verification of the 'triangle' method for obtaining surface soil water content and energy fluxes from remote measurements of the normalized difference vegetation index (NDVI) and surface radiant temperature. *International Journal of Remote Sensing* 18: 3145-3166.
- Groeneveld, D.P., W.M. Baugh, J.B. Silverman, D.D. Barz, and M.B. Prescott, 2006. *Non-imaging Airborne Spectroscopy for Calibration Satellite Imagery*. Hydrobio Advanced Remote Sensing report, 20 pp. <http://www.asdi.com/resource-center/application-notes>
- Groeneveld, David P. and William M. Baugh, 2007. Correcting satellite data to detect vegetation signal for eco-hydrologic analyses. *Journal of Hydrology* 344 (1-2): 135-145.

- Groeneveld, David P., William M. Baugh, John S. Sanderson, and David J. Cooper, 2007. Annual groundwater evapotranspiration mapped from single satellite scenes. *Journal of Hydrology* 344 (1-2): 46-156.
- Harrill, J.R. and L.B. Hines, 1995. *Estimated natural ground-water recharge, discharge, and budget for the Dixie Valley area, west-central Nevada*: U.S. Geological Survey Water-Resources Investigations Report 95-4052, 12 p., <http://pubs.er.usgs.gov/publication/wri954052>.
- Huete, Alfredo, Justice, Chris, and van Leeuwen, Wim, 1999, MODIS Vegetation Index (MOD 13), Version 3. Algorithm Theoretical Basis Document, accessed March 4, 2015, at http://modis.gsfc.nasa.gov/data/atbd/atbd_mod13.pdf
- Huete, A., Didan, K., Miura, T. Rodriguez, E., Gao, X., and Ferreira, L., 2002. Overview of the radiometric and biophysical performance of the MODIS vegetation indices. *Remote Sensing of Environment* 83: 195-213.
- Huntington, J.L. and R. Allen, 2010. *Evapotranspiration and Net Irrigation Water Requirements for Nevada*, Nevada State Engineer's Office Publication, 266 pp.
- Irish, R. R., 2000, *Landsat 7 Science Data User's Handbook*, Report 430-15-01-003-0, National Aeronautics and Space Administration.
- Jackson, Ray D. and Alfredo R. Huete, 1991. Interpreting vegetation indices, *Preventive Veterinary Medicine* 11: 185-200.
- Karnieli, A., R.F. Kokaly, N.E. West, and R.N. Clark, 2001. Remote Sensing of Biological Soil Crusts. In, Ecological Studies, Vol. 150, J. Belknap and O.L. Lange (eds.) *Biological Soil Crusts: Structure, Function, and Management*, copyright Springer-Verlag Berlin Heidelberg.
- Los, S.O., C.J. Tucker, A. Anyamba, M. Cherlet, G.J. Collatz, L. Giglio, F.G. Hall, and J.A. Kendall, 2002. The biosphere: a global perspective. Chapter 5, pp. 68-93 in Skidmore, Andrew (2002), *Environmental Modelling with GIS and Remote Sensing*, Taylor & Francis, New York.
- Markham, B. L. and Barker, J. L., 1986. Landsat MSS and TM post-calibration dynamic ranges, exoatmospheric reflectances and at-satellite temperatures, *EOSAT Landsat Technical Notes* 1: 3-8.
- Masek, J.G., Vermote, E.F., Saleous, N., Wolfe, R., Hall, F.G., Huemmrich, F., Gao, F., Kutler, J., and Lim, T.K., 2006. A Landsat surface reflectance data set for North America, 1990-2000, *IEEE Geoscience and Remote Sensing Letters*, 3: 68-72.
- Matsushita, Bunkei, Wei Yang, Jin Chen, Yuyichi Onda, and Guoyu Qiu, 2007. Sensitivity of the Enhanced Vegetation Index (EVI) and Normalized Difference Vegetation Index (NDVI) to Topographic Effects: A Case Study in High-density Cypress Forest, *Sensors* 7 (11): 2636-2651.

- Qi J., Chehbouni A., Huete A.R., Kerr Y.H., 1994. Modified Soil Adjusted Vegetation Index (MSAVI), *Remote Sensing of Environment* 48: 119-126.
- Rouse, J. W., R. W. Haas, J. A. Schell, D. W. Deering, and J. C. Harlan, 1974. Monitoring the vernal advancement and retrogradation (green wave effect) of natural vegetation. NASA/GSFC, Type 3, Final Report, Greenbelt, MD.
- Yoon, Howard W., David W. Allen, George P. Eppeldauer, and Benjamin K. Tsai, 2009. The Extension of the NIST BRDF Scale from 1100 nm to 2500 nm, in *Proceedings of Earth Observing Systems XIV*, SPIE Volume 7452, ISBN: 9780819477422.